2008

Digital processing and data compilation approach for using remotely sensed imagery to identify geological lineaments in hard-rock terrains : an application for groundwater explorations in Nicaragua

Jill N. Bruning
Michigan Technological University

A DIGITAL PROCESSING AND DATA COMPILATION APPROACH FOR USING REMOTELY SENSED IMAGERY TO IDENTIFY GEOLOGICAL LINEAMENTS IN HARD-ROCK TERRAINS: AN APPLICATION FOR GROUNDWATER EXPLORATION IN NICARAGUA

By
Jill N. Bruning

A Thesis

Submitted in partial fulfillment of the requirements
for the degree of

MASTER OF SCIENCE
GEOLOGICAL ENGINEERING

MICHIGAN TECHNOLOGICAL UNIVERSITY
2008

This thesis, “A DIGITAL PROCESSING AND DATA COMPILATION APPROACH FOR USING REMOTELY SENSED IMAGERY TO IDENTIFY GEOLOGICAL LINEAMENTS IN HARD-ROCK TERRAINS: AN APPLICATION FOR GROUNDWATER EXPLORATION IN NICARAGUA,” is hereby approved in partial fulfillment of the requirements for the Degree of MASTER OF SCIENCE IN GEOLOGICAL ENGINEERING.

Department of Geological and Mining Engineering and Sciences

Thesis Advisor: _____

Dr. John S. Gierke

Department Chair: _____

Dr. Wayne P. Pennington

Date: _____

TABLE OF CONTENTS

LIST OF FIGURES

LIST OF TABLES

ABSTRACT

A DIGITAL PROCESSING AND DATA COMPILATION APPROACH FOR USING REMOTELY SENSED IMAGERY TO IDENTIFY GEOLOGICAL LINEAMENTS IN HARD-ROCK TERRAINS: AN APPLICATION FOR GROUNDWATER EXPLORATION IN NICARAGUA

Sustainable yields from water wells in hard-rock aquifers are achieved when the well bore intersects fracture networks. Fracture networks are often not readily discernable at the surface. Lineament analysis using remotely sensed satellite imagery has been employed to identify surface expressions of fracturing, and a variety of image-analysis techniques have been successfully applied in "ideal" settings. An ideal setting for lineament detection is where the influences of human development, vegetation, and climatic situations are minimal and hydrogeological conditions and geologic structure are known. There is not yet a well-accepted protocol for mapping lineaments nor have different approaches been compared in non-ideal settings. A new approach for image-processing/synthesis was developed to identify successful satellite imagery types for lineament analysis in non-ideal terrain. Four satellite sensors (ASTER, Landsat7 ETM+, QuickBird, RADARSAT-1) and a digital elevation model were evaluated for lineament analysis in Boaco, Nicaragua, where the landscape is subject to varied vegetative cover, a plethora of anthropogenic features, and frequent cloud cover that limit the availability of optical satellite data. A variety of digital image processing techniques were employed and lineament interpretations were performed to obtain 12 complementary image products that were evaluated subjectively to identify lineaments. The 12 lineament interpretations were synthesized to create a raster image of lineament zone coincidence that shows the level of agreement among the 12 interpretations. A composite lineament interpretation was made using the coincidence raster to restrict lineament observations to areas where multiple interpretations (at least 4) agree. Nine of the 11

previously mapped faults were identified from the coincidence raster. An additional 26 lineaments were identified from the coincidence raster, and the locations of 10 were confirmed by field observation. Four manual pumping tests suggest that well productivity is higher for wells proximal to lineament features. Interpretations from RADARSAT-1 products were superior to interpretations from other sensor products, suggesting that quality lineament interpretation in this region requires anthropogenic features to be minimized and topographic expressions to be maximized. The approach developed in this study has the potential to improve siting wells in non-ideal regions.

1.0 Introduction

Lineament analysis in hard-rock terrains has been performed widely as a means for remote groundwater exploration. Using remotely sensed satellite imagery, lineaments are detected by alignment trends of features such as vegetation, drainage patterns, outcrop truncations, soil moisture, topography, etc. These can be identified with remotely sensed attributes including tone, color, texture, pattern, and association. Such lineaments are indicative of secondary porosity in the form of fractures and if intersected by a well at depth have the potential to supply large and reliable quantities of water (Park et al. 2000, Mabee 1999, Magowe and Carr 1999, Edet et al. 1998, Sander et al. 1997, Kresic 1995, Mabee et al. 1994).

A variety of lineament analysis techniques using remotely sensed data exist and have been developed in near ideal settings where influences of anthropology, vegetation, climatic situations are minimal (e.g., Meijerink et al. 2007, Kann and Glenn 2006, Hung et al. 2005, Murphy and Burgess 2005, Glenn and Carr 2004, Abouma-Simba 2003, Paganelli et al. 2003, Mabee 1999, Magowe and Carr 1999, Robinson et al. 1999, Edet et al. 1998, Henderson et al. 1996, Mahmood 1996, Mabee et al. 1994, Boeckh 1992, Krishnamurthy 1992). Furthermore, such lineament studies have been executed in regions with reputable knowledge of hydrology and geology. For these reasons there is no well-accepted or proven protocol for mapping lineaments nor have different approaches been compared in non-ideal regions. The most important questions about defining a lineament analysis process in difficult settings include: (1) what imagery type or combination of imagery types are best to detect lineaments?, (2) what processing and interpretation technique(s) works best to enhance the appearance of fracturing?, and (3) how do lineaments delineated from remotely sensed imagery compare to field observations (i.e., ground truth)? The technical aim of this work brings together a combination of data-processing tools, such as ERDAS Imagine and ArcGIS, in conjunction with a variety of information including several types of

remotely sensed imagery (Quickbird, Landsat 7 ETM+, ASTER, and RADARSAT-1), field observations, pumping tests, geological and topographic maps, and a DEM in order to create an effective and efficient method for lineament analysis in a challenging setting. The method is a low-cost, non-invasive approach for improving groundwater exploration in challenging, remote areas.

This work is part of a larger project within Michigan Technological University's Geological and Mining Engineering and Sciences Department titled, "Remote Sensing for Hazards Mitigation and Resource Protection in Latin America" (http://www.geo.mtu.edu/rs4hazards). The project is funded by the National Science Foundation's Office of International Science and Engineering under the Partnerships for International Research and Education (PIRE) program. The aim of project work is to build and strengthen collaborative research and education between MTU and agencies in Guatemala, Nicaragua, El Salvador, and Ecuador for natural hazard mitigation and resource protection (Rose and Bluth 2005). The work presented here has been assisted by a variety of counterparts in Nicaragua who helped to facilitate the field work and publicize the projects efforts to various stakeholders. Wisconsin/Nicaragua Partners of the Americas, a nongovernmental organization, is one of these counterparts and was responsible with connecting community leaders in Boaco with students and faculty at MTU. Boaco municipal government officials and many community members have helped locate geological information and gain access to properties for conducting field work.

1.1 Previous Work

Historically, image interpretation for lineament identification has been performed with aerial photography and 1st-generation satellite imagery using stereo pairs, light tables, and transparencies (Gupta 2003). Today, numerous advanced sensors exist;

making image processing and interpretation techniques much more powerful and complex, as there are several sensor options for various applications.

1.1.1 Imagery Types Suitable for Lineament Detection

Optical sensors of moderate spatial resolutions have been used extensively for lineament analysis (Meijerink et al. 2007, Sander 2007, Arellano-Baezo et al. 2006, Kann and Glenn 2006, Hung et al. 2005, Ricchetti and Palombella 2005, Inzana et al. 2003, Drury and Andrews 2002, Lee and Moon 2002, Ricchetti 2002, Loizzo et al. 1994). In particular, ASTER and Landsat are specifically designed to detect geological information, including structure, due to their spectral resolutions in both the visible and infrared portions of the electromagnetic spectrum (Drury and Andrews 2002). Furthermore, several studies have been carried out to boost geological knowledge and revise existing geological maps in remote regions of the world using optical remotely sensed data. For example, Kann and Glenn (2006) mapped a remote area of northern Pakistan using ASTER imagery and discovered two active strike-slip faults that were previously unmapped. Few studies have employed optical sensors in combination for lineament detection (Hung et al. 2005, Murphy and Burgess 2005, Akman and Tüfeçi 2004). Hung et al. (2005) compared lineament interpretations from Landsat 7 ETM+ and ASTER imagery and observed fewer erroneous results from ASTER derived lineaments compared with Landsat 7 ETM+ derived lineaments. They attribute the difference to the higher spatial resolution of ASTER data.

High spatial resolution satellite remotely sensed imagery has not been widely employed in lineament studies for groundwater exploration, primarily due to cost and limited spectral resolution (Sander 2007). However, water resource studies have used high spatial resolution sensors to monitor land use and land cover. Sawaya et al. (2003) employed QuickBird and IKONOS for monitoring water resources including observations of lake clarity, mapping of urban impervious areas, and examination of

aquatic vegetation populations. These sensors allowed for the assessment to include smaller water bodies, which would not have been possible with a sensor of a larger spatial resolution (Sawaya et al. 2003). Although shadows from tall objects affected classification results, high spatial resolution imagery has great potential for water studies at local scales (Sawaya et al. 2003). This was demonstrated by Loveless et al. (2005) by using IKONOS to map geological "cracks" at local scales associated with the tectonic setting in coastal Chile. These cracks range in aperture from a few centimeters to 2.5m and were easily observable due to the hyper-arid climate of the region and IKONOS's 1-m pixel resolution (Loveless et al. 2005).

A variety of image processing techniques have been utilized to enhance linear features in optical imagery (Kann and Glenn 2006, Ricchetti and Palombella 2005, Krishnamurthy et al. 1992). The study by Kann and Glenn (2006) mentioned earlier employed decorrelation stretches (stretch enhancements) and principle components analysis (PCA) to aid in geological mapping. Offsets of rock types due to the two newly discovered faults were apparent using these image processing techniques as they exploit the unique spectral signatures of each lithological formation. Krishnamurthy et al. (1992) explored a variety of digital image processing techniques on a Landsat TM image of Karnataka, India for groundwater investigations. Their processing resulted in 13 image products, which were assessed to exhibit several geologic and geomorphic features. The assessment was performed in a qualitative manner and the ability of products to exhibit features was ranked as either good, moderate, or poor (Krishnamurthy et al. 1992). They recommend five Landsat TM products including (1) normalized band 4, (2) composite of normalized bands 3, 5, and 7, (3) composite of first three principle components, (4) composite of vertical filtered band 7, diagonal filtered band 5, and horizontal filtered band 7, and (5) band subtraction of band 4 – band 3 (Krishnamurthy et al. 1992).

Radar sensors, such as RADARSAT-1 and JERS-1 SAR, are an attractive alternative to or in complement with optical sensors for lineament detection. Unlike optical sensors, which rely upon the sun's illumination, radar sensors are active sensors, as they provide their own source of ground illumination. Additionally, the long wave lengths of radar signals are able to image through clouds and other atmospheric obstructions. This means that radar sensors are able to collect imagery regardless of time of day and weather conditions. Radar sensors respond to surface topography, roughness, and dielectric properties, unlike optical sensors which respond to optical and thermal attributes (Radarsat Geology Handbook 1996, Mahmood 1996). Thus, radar images contain less anthropogenic and vegetation information and exhibit more topographic information (Mahmood 1996).

Radar has been proven a good option for geologic mapping where soil cover inhibits viewing geological features (Paillou and Rosenqvist 2003, Abouma-Simba et al. 2003, Robinson et al. 1991). Schaber et al. (1997) showed radar penetrations of 30 cm in dry, eolian sand using X-band, 52 cm using C-band, and up to 2.07 m using L-band. Radar penetration increases with greater incidence angle and homogeneity and with less moisture and grain size (Robinson et al. 1991). Robinson et al. (1999) exposed a network of drainage patterns and faults below 10 to 30 cm sand dune and megaripple deposits in northwestern Sudan using RADARSAT-1 imagery. These hydrological features were not revealed with similar-resolution Landsat TM imagery even after advanced image processing, demonstrating RADARSAT-1's usefulness over optical sensors for groundwater exploration in desert regions (Robinson et al. 1999). However, Robinson et al. (1999) did emphasize that including optical imagery in remote studies is essential in determination of a feature being subsurface or surface.

Radar has also proven to be a good option for mapping in regions of vegetation cover (Abouma-Simba et al. 2003, Paradella et al. 2000, Paradella et al. 1998). Natural

variations in vegetation cover are closely linked to geology in remote settings, such as in the Brazilian Amazon, and are detectable using RADARSAT-1/Landsat TM integrated products (Paradella et al. 1998) due to the differences in incidence angles of the two types of imagery. Research conducted by Paradella et al. (1998) produced a geological map of the study area from a RADARSAT-1/Landsat TM stack which mapped five geological units and two primary lineament systems for the first time. Furthermore, a method called tree-top geology is also employed for mapping in areas of dense vegetation using radar imagery (Radarsat Geology Handbook 1996). Radar responds largely to topography, which is mirrored by tree canopy height, allowing for structural information to be derived in such settings (Radarsat Geology Handbook 1996).

Image processing of radar imagery is often performed to highlight geological features. Principle component analysis was employed by Paganelli et al. (2003) on a stack of four RADARSAT-1 scenes (standard beam mode S1 and S7 acquired in descending and ascending orbital directions) to provide structural information for geological mapping for kimberlite exploration in the Buffalo Head Hills area of northern Alberta, Canada. Lineament interpretations were calibrated using several detailed, reputable structural studies, one of which being the Alberta Geological Survey. Results of Paganelli et al. (2003) showed principle components 2 and 3 preserved topographic information, such as pattern and texture, necessary to interpret bedrock structures. RADARSAT has also been used to delineate geomorphic features via change detection between two scenes acquired at different times of the year (Glenn and Carr 2003, Radarsat Geology Handbook1996) due to differences in surface moisture. High reflectivity values in radar imagery can be caused by increased moisture content in both soils and vegetation and have shown to enhance linear topographic features (Glenn and Carr 2003).

DEMs also have been shown to be useful for detecting lineaments because they can eliminate bias in remotely sensed imagery caused by inherent east-west sun illumination as a DEM hill-shade can be illuminated from any direction (Henderson et al. 1996, Yun and Moon 2001). Such studies that detect lineaments from DEMs alone rely on the assumption that the majority of lineaments in a given study area are geomorphic rather than tonal (Yun and Moon 2001). This assumption, however, is valid for most regions as valley and cliff orientations are typically controlled by faulting direction (Yun and Moon 2001).

1.1.2 Lineaments and Groundwater Occurrence in Hard-rock Terrains

Relationships between lineament characteristics, remotely sensed data, and well yield have been explored in several studies (Mabee et al. 1994, Kresic 1995, Sander et al. 1997, Edet et al. 1998, Magowe and Carr 1999, Mabee 1999, Park et al. 2000). According to this literature, a relationship exists between high lineament intersection densities and greater well productivity. Magowe and Carr (1999) visually interpreted imagery for lineaments, which control surface drainage patterns in their study area. Well yields were determined from 226 wells and were coded as having either high yield (>1 m^3/hr) or low yield (<1 m^3/hr). This data was used to create a raster of well yields with the use of kriging interpolation. Lineament intersections were then overlain onto the well yield raster, showing that areas of high well yield coincide with lineament intersections. They found that median well yield correlated with the proximity to lineament intersection.

Because locations of high lineament density correlate to high well productivity, lineament analysis via remotely sensed image interpretation is used extensively to pinpoint locations for follow-up detailed geophysical investigations (Boeckh 1992, Mabee et al. 1994, Raju and Reddy 1998, Breilin et al. 2003, Hung et al. 2004). Mabee et al. (1994) recognized that image interpretation often results in a huge collection of lineaments. They proposed a method for reducing the number of

interpreted lineaments in order to focus detailed field investigations. The method they developed uses three steps: (1) visual image interpretation via multiple observers, multiple images, and multiple trials by one observer, (2) reproducibility tests, and (3) domain overlap analysis (Mabee et al. 1994). The first step ensures that lineaments drawn at a given geographic location can be duplicated during additional trials or by other observers. Reproducibility tests take this concept further by applying a range of acceptable values to the lineaments, such as +/- 5° azimuth. Domain overlap analysis separates lineaments into fracture domains determined by local geological knowledge. They were able to reduce the number of lineaments in their study location from more than 6,500 to less than 250. Using statistical analysis, the remaining lineaments were shown to coincide more accurately with higher yields of nearby wells compared to lineaments that did not meet the domain overlap analysis criteria.

Domain overlap analysis and other orientation dependent methods are typically applied to evaluate lineament interpretations (Loveless et al. 2005, Murphy and Burgress 2005, Akman and Tüfeçi 2004, Edet et al. 1998, Mabee et al. 1994). These methods are based heavily upon a detailed field campaign focusing on structure to isolate acceptable ranges of lineament orientations. Data collected on such a campaign requires numerous rock outcrops displaying fractures and joints to be available and accessible in a given study area.

Although methods such as Mabee et al. (1994) incorporate reproducibility tests in an attempt to eliminate erroneous data, lineament mapping based on visual interpretation is a subjective process as it varies with an individual's experience and ability. "*The human observer is a variable detector of features and does not produce the same annotation on each occasion*." writes Burns and Brown (1978). In an attempt to increase reproducibility, objective automated/digital methods have been developed (Cross and Wadge 1988, Wang and Howarth 1990, Sawaragi et al. 1992, Saether et al. 1994, Kageyama et al. 2000, Vassilas et al. 2002). However, these methods often

identify cultural features (e.g., roads and field boundaries) as potentially geological lineaments. In addition, the effect of sun angles, which produce shadow and other effects, add noise and compound this problem. As a result, visual interpretation is still the most extensively applied approach (Gupta 2003).

A detailed review of literature since 1985 regarding the use of remote sensing and GIS methods to investigate various groundwater problems was executed by Jha et al. (2007). Several areas were identified where future groundwater-based studies should focus to develop remote sensing and GIS technologies. This includes the need for further examination of remotely sensed data reliability by assessing the correlation between remotely sensed observations with surface-based measurements and groundwater occurrence. They recognize that as future remote sensing instruments and data become available, studies need to continue to refine analysis and interpretation techniques in agreement with field measurements. A great deal of this review focuses on applications in developing countries, where standard methodology is often lacking. Constraints, including few or no groundwater monitoring programs and a dearth of available remotely sensed and GIS data, compound development difficulties. One solution the authors suggest is to proliferate awareness of remote sensing and GIS technologies in both the government and private sectors within developing countries.

1.2 Study Area

The study is executed in and around the small Nicaraguan town of Boaco, a rural community of 20,000 (municipality population of 54,000) located in the country's interior highlands, roughly 100-km northeast of Managua, Figure 1.

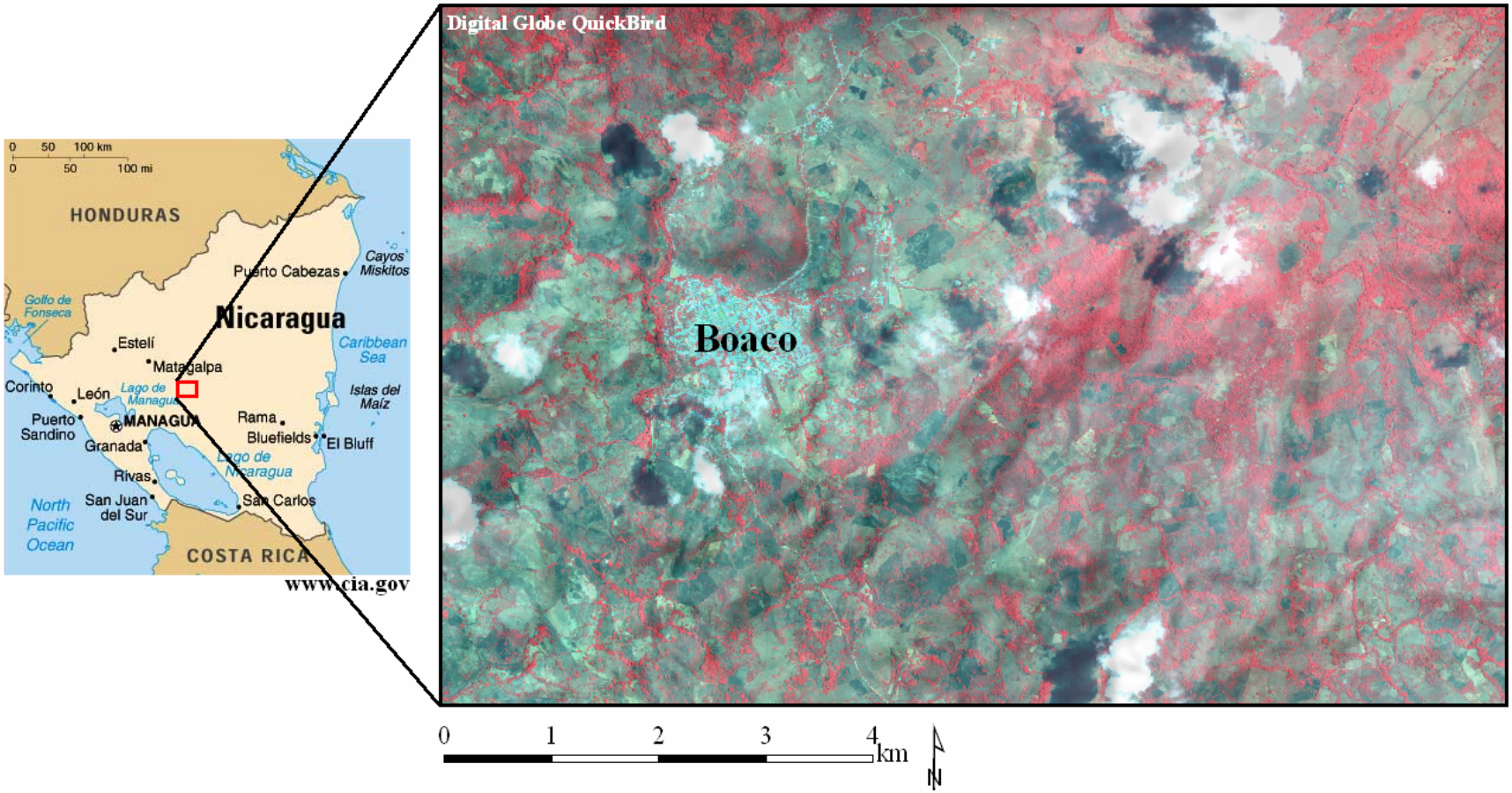

Figure 1: Location of study area. Imagery derived from Digital Globe QuickBird (2006. The municipality of Boaco is located approximately 100 km northeast of Managua in Nicaragua's interior highlands. Elevations in the study area vary from 250 m to 750 m.

This study area was chosen for the following reasons:

- Two previous field campaigns in December 2005 and January 2007 to this site have been carried out as part of MTU Aqua Terra Tech Enterprise project work. As a result, relationships have been built between this research group and the local government officials and civilians. It has been our experience that positive working relationships in Central America take years to develop. Central American agencies are often asked to supply information and assistance for foreign research without ever seeing any benefit. Additionally, previous field campaigns have yielded knowledge of the terrain, geology, and potential obstructions/challenges in the field, which is valuable when planning for return campaigns.

- A large set of remotely sensed imagery and ancillary data has been collected previous to this study by Aqua Terra Tech Enterprise. This includes the purchase of a QuickBird scene, acquisition of a RADARSAT-1 and Landsat7 ETM+ scenes, topographic map, geological map, and several GIS thematic shapefiles (i.e. roads, rivers).

- The combination of highly fractured bedrock aquifers and water scarcity is not unique to Boaco. Therefore, this study location can serve as a proxy for similar fractured hard-rock terrains not only in Central America but elsewhere in the world.

It is important to note that Boaco has several characteristics that make this site non-ideal for lineament analysis. Few outcrops are available for structural measurements making it near impossible to employ traditional lineament analysis techniques. The presence of a topical climate, severe anthropogenic influences on land use and land cover, and a lack of hydrological and geological information compounds the problem. However, our personal connections with the Boaco community and their need for improvement in well siting techniques override these downfalls.

1.2.1 Geological Setting

The municipality of Boaco, Nicaragua, approximately 100km NE of Managua, is located upon the Chortis Block. Positioned in the northwest part of the Caribbean Plate, the Chortis Block is the only continental constituent of the Caribbean Plate (Bundschuh and Alvarado 2007, Weyl 1980). It is bounded to the southwest by the Middle American trench and 1100-km long volcanic arc associated with the Cocos Plate subduction below the Caribbean Plate (Rogers 2003). To the north, the Chortis Block is bounded by the Maya Block of the North American Plate located in south-central Guatemala. Here, juxtaposition of the Caribbean and North American Plates form the Motagua-Polochic Fault zones (Bundschuh and Alvarado, 2007). The south and east boundaries of the Chortis Block are not well defined and lay either somewhere in the lowlands of eastern Honduras and Nicaragua or on the carbonate platform of the Nicaraguan Rise below the Caribbean Sea (Rodgers 2003).

Weyl (1980) defines four first-order controls over regional structure and geomorphology in this region of Central America and include:

- The E/W trending, left-lateral, strike-slip motion of the Motagua-Polochic Fault zone caused by the boundary between the Caribbean and North American Plates.

- Far-reaching, normal faults that parallel the Pacific margin (trending approximately NW/SE), which are most dramatically expressed by the Nicaragua Depression, and are due to uplift caused by subduction of the Cocos Plate below the Caribbean Plate.

- Fault and graben systems trending N/S, however these structures reside primarily north and east of the study area, the largest of which being the Honduras Depression. These structures form a tensional zone thought to be caused by slightly differing rotation of portions of the Caribbean Plate.

- Transverse faults trending NNE/ SSW to NE/SW caused by deep-seated segmented boundaries of Cocos Plate within the Pacific Marginal Zone

The Chortis Block basement is composed primarily of Precambrian-Paleozoic metamorphic and igneous rocks (Bundschuh and Alvarado 2007, Rogers 2003). Locally in Boaco, Nicaragua, the basement materials are overlain by Quaternary alluvium, lavas, and pyroclastics and Tertiary ash, basalts, andesites, dacitic ignimbrites, and plutonic intrusives of the Coyol and Matagalpa Groups (Rogers 2003, Weyl 1980). A geological map of the Boaco region is provided in Figure 2 and the stratigraphy of these units is shown in Figure 3.

Boaco is located in what is known as the Tertiary volcanic ranges and plateaus, which are extensively present in Nicaragua and Honduras and in portions of El Salvador and Guatemala (Weyl 1980). The terrain is characterized by wide-spread plateaus and fault-block mountains. Rivers and other drainages incise deeply into the topography often following fracture patterns, creating a rugged landscape. Elevations can reach over 1000 m, however Boaco sits at approximately 400-m elevation.

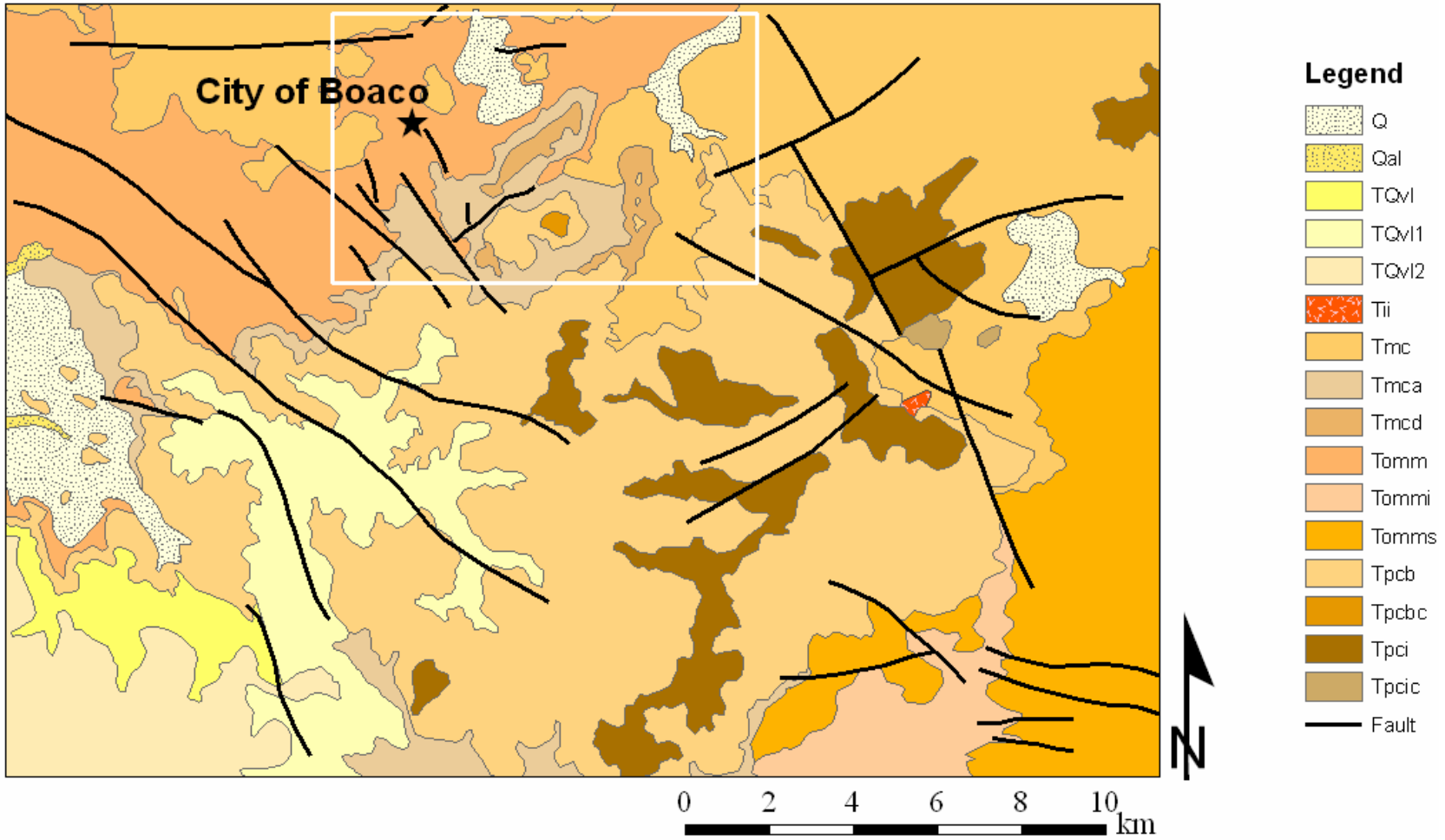

Figure 2: Geological map of the Boaco region. Geological Map adapted from Office of Cadasters and Natural Resources Inventory (1971). The white box shows the geographical location of the study area. The city of Boaco is located at 12°29'N 85°40'W.

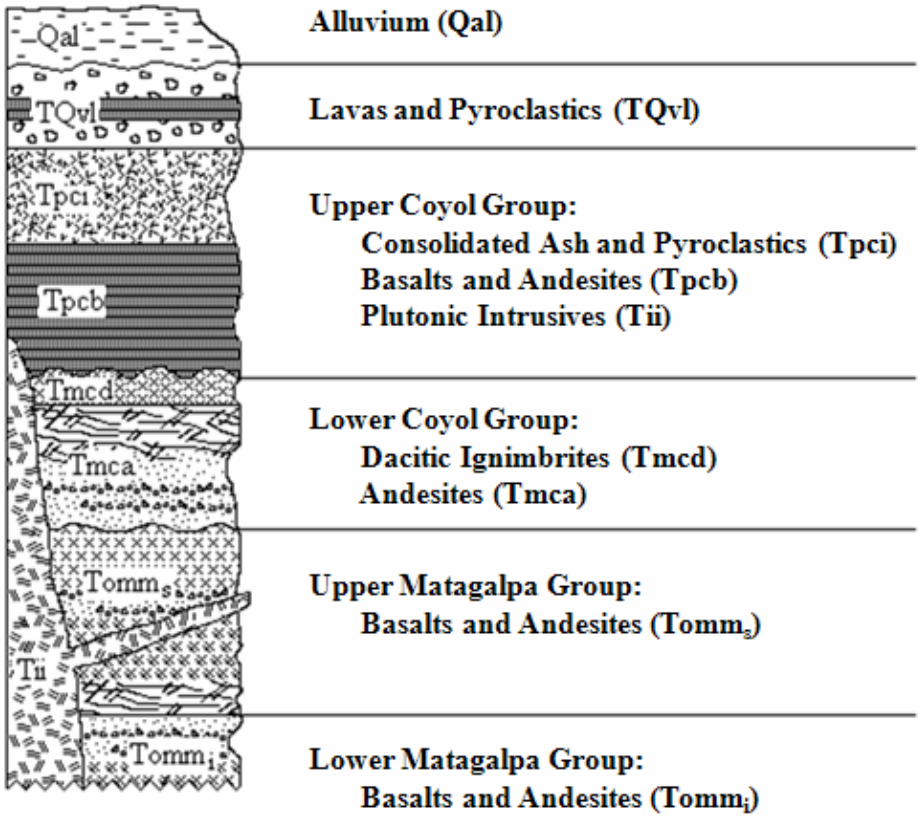

Figure 3: Generalized stratigraphic column for Boaco, Nicaragua. Adapted from Office of Cadasters and Natural Resources Inventory (1971).

1.2.2 Groundwater Occurrence and Society

The Central Highlands of west-central Nicaragua consists of alluvial and volcanic aquifers. Alluvial aquifers occur in intermountain valleys and are exceptionally heterogeneous. The composition of these alluvial aquifers range from clay to gravel sized sedimentary material and can be either unconsolidated or semi-consolidated (Bundschuh and Alvarado, 2007). These sediments are interrupted by layers of tuff, volcanic ash, and ignimbrites forming complex aquifer/aquitard structures (Bundschuh and Alvarado, 2007). Water flow in the alluvial deposits is dictated by intergranular flow and the majority of well yields are low to moderate (Bundschuh

and Alvarado, 2007). Volcanic aquifers dominate the highland and volcanic arc regions of Nicaragua. These aquifers are composed of fractured andesite, basalt, and ignimbrites stratified with lower permeability tuff and ash deposits. Water flow in these hard-rock aquifers are controlled by the density and distribution of secondary porosity primarily in the form of fractures (Magowe and Carr, 1999). Wells producing within highly fractured rock have potential for moderate to high water yields (>10L/s). Nearly all wells, both drilled and hand-dug, are sited by water diviners (Gross 2008, Gutierrez 2008). Of the 150 wells drilled in 2007 by a local driller in Boaco, 70% produce less than 5 gal/min and are considered non-productive (Gutierrez 2008).

Nicaragua's population is highly dependent upon groundwater resources with 95% of people relying on groundwater (Bundschuh and Alvarado, 2007). Nicaragua's groundwater dependency is significantly higher than the rest of the world, where only about 30% to 50% of the global population relies on groundwater (Bundschuh and Alvarado, 2007). Groundwater resources of Nicaragua are naturally high quality and are reliable throughout the year (Bundschuh and Alvarado, 2007). Conversely, surface waters in Nicaragua are generally polluted and rivers and streams experience low flows during the dry season (November through April) (Bundschuh and Alvarado, 2007).

Local municipal governments in Nicaragua control water management; however they lack adequate funds and technical expertise needed to support most management activities and any existing water policies primarily focus on surface water (Bundschuh and Alvarado, 2007). Widespread poverty among communities compounds the problem, as most communities have insufficient sewage treatment, if any, and watershed protection is absent. In rural communities, water wells are mostly shallow (hand-dug) and extract from the water table region, which is commonly polluted.

2.0 Objectives

Many of the techniques used for traditional lineament analysis discussed in the reviewed literature above cannot be employed in Pacific Latin America due the challenging conditions inherent to this region. These conditions include intensive weathering of near surface bedrock, tropical climate, vegetation in which the type and pattern are constrained by land use/land cover, and the lack of geological and hydrological knowledge. The motive of this study is to determine if and how these conditions can be overcome to develop a more-effective approach to map lineaments in this region. This work combines select elements from methods previously developed along with other new techniques to create a standardized lineament mapping procedure for Pacific Latin America.

The objectives of this study are to:

- Develop a comprehensive approach for using lineament analysis techniques for groundwater development in fractured bedrock aquifers in tropical climates where limited knowledge of geology and hydrology exist.

- Compare the abilities of a broad assortment of imagery types, combination of imagery types, and image processing methods to determine which produces the best lineament interpretation.

- Explore appropriate methods to evaluate lineament interpretations via ground validation and well pump tests.

3.0 Methods

As with any lineament study, it is important to establish the author's definition of the term *lineament*. In the context of this study, a lineament is considered a surface expression of fracturing in the form of topographic alignments (i.e., valleys and cliffs), alignments of streams, rivers, and other drainages, linear trends in vegetation and soil-moisture anomalies, and truncation of rock outcrops. A variety of remotely sensed data were utilized to detect lineaments for identifying zones of subsurface fractures in Boaco, Nicaragua. The procedure has three primary steps: (1) data preparation, (2) feature exploitation and detection, and (3) evaluation of results.

3.1 Data Preparation

3.1.1 Fracture Phenomenology Assessment

A list of fracture characteristics and descriptions, as well as insights for lineament detection, was created to gain understanding of surface expressions of fracturing, shown in Table 1. Of these phenomena, orientation and length dependent upon the study area and were measured from a regional geological map, 1:50,000 scale. Faults were digitized from the geological map (Office of Cadasters and Natural Resources Inventory, 1971) using ArcGIS (ESRI, 2006) and fault orientation and length data was derived using the Linear Directional Mean tool. The fault orientations were plotted using MATLAB (The MathWorks, Inc. 2007) and are shown in Figure 4.

Table 1: Fracture phenomenology. Fracture phenomenons, or attributes, include orientation, length, roughness, seasonal variation, soil moisture content, vegetation type and health, drainage and topographic control, and thermal response.

Fracture Phenomenon	**Description**	**Possible Imagery for Detection** (bands)	**Possible Processing Method(s) and *Notes***
Orientation	Major directions: 75°, 150° *(Measurements based on geological maps)*	All	*Note:* detection may be dependent upon illumination direction.
Length	0.52 km – 15.8+ km *(Measurements based on geological maps)*	All	*Note*: detection may be dependent upon spatial resolution and observation scale.
Roughness	Zones of intense fracturing will be mirrored by complex topography, creating random backscatter values and therefore appear as a "rough" surface.	All, especially RADARSAT-1	Original RADARSAT-1 images (no despeckling)
Seasonal Variation	See "Soil Moisture Content" and "Vegetation Health" phenomenons.	RADARSAT-1	Change detection of dry season vs. wet season, PCA.
Soil Moisture Content	Radar reflects brightly off water, therefore water-bearing fractures would appear brighter than surrounding areas.	RADARSAT-1	Change detection of dry season vs. wet season, PCA.
Vegetation Type	Vegetation species requiring year-round water will occupy water-bearing lineaments.	ASTER (1-3) Landsat7 ETM+ (1-4) QuickBird (1-4)	Normalized Difference Vegetation Index (NDVI), "natural color" bands of optical imagery
Vegetation Health	Vegetation growing along water-bearing fractures have much more moisture available than nearby vegetation and therefore be more reflective in the IR bands.	ASTER (3-8) Landsat7 ETM + (4) QuickBird (4)	NDVI.
Drainage Control	Because fractures are zones of weakness, streams and rivers often follow fractures and can make sharp angle turns where intersected by faults.	All	Overlay digitized drainage shapefiles onto imagery.
Topographic Control	*Valley*: fractures are often enlarged by weathering and erosion, becoming small valleys. *Cliff*: faults with large offsets produce cliffs or very steep slopes.	DEM	Displaying DEM as a hillshade (with vertical exaggeration) below somewhat transparent remotely sensed imagery.
Thermal Response	In nighttime imagery, groundwater filled fractures will be warmer than the surrounding ground. In mid-day time imagery, groundwater filled fractures will be cooler than the surrounding ground.	ASTER (9+)	Change detection of night vs. day time imagery, PCA. *Note:* A cloud-free ASTER scene is not available; it is not possible to test this method in this study.

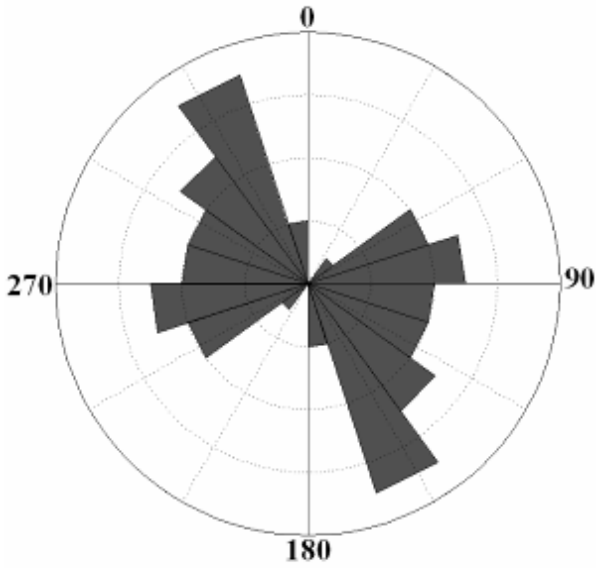

Figure 4: Rose diagram of fault orientations. Faults were digitized in ArcGIS from a 1:50,000 scale geological map (Office of Cadasters and Natural Resources Inventory 1971) and orientation directions were calculated using the Linear Directional Mean tool and shows the two primary faulting directions with azimuths of 75° and 150°.

3.1.2 Imagery Selection

A suite of image types from different sensors are employed in this study and their attributes are compared in Table 2. The diversity of characteristics present with these sensors provides an array of information needed to evaluate which remotely sensed imagery type is most successful for lineament detection in this study area. Also, this enables a unique fusion of imagery types preceded by a re-extraction of lineaments from these composites. The combined use of two or more image types may prove to be a more powerful tool to detect lineaments than a single image alone.

Table 2: Sensor attributes. Sensors employed in this study and their spectral and spatial resolutions of bands, quantization, and the publisher of the imagery are shown.

Sensor	Band	Spectral Resolution (mm)	Spatial Resolution (m)	Quantization (Bits)	Publisher
Quickbird	1	0.45 - 0.52	0.6	16	Digital Globe
	2	0.52 - 0.60			
	3	0.63 - 0.69			
	4	0.76 - 0.89			
Landsat 7 ETM+	1	0.450 - 0.515	30	8	Global Land Cover Facility, University of Maryland
	2	0.525 - 0.605			
	3	0.630 - 0.690			
	4	0.750 - 0.900			
	5	1.55 - 1.75			
	6	10.40 - 12.50	60		
	7	2.08 - 2.35	30		
	8 (panchromatic)	0.52 - 0.90	15		
ASTER	1	0.52 - 0.60	15	8	Land Processes Distributed Active Archive Center, NASA
	2	0.63 - 0.69			
	3	0.76 - 0.86			
	3 (backward)	0.76 - 0.86			
	4	1.600 - 1.700	30		
	5	2.145 - 2.185			
	6	2.185 - 2.225			
	7	2.235 - 2.285			
	8	2.295 - 2.365			
	9	2.360 - 2.430			
	10	8.125 - 8.475	90	12	
	11	8.475 - 8.825			
	12	8.925 - 9.275			
	13	10.25 - 10.95			
	14	10.95 - 11.65			
RADARSAT-1	C-band	56-mm radar pulses at 5.3Ghz	12.5	8	Alaska Satellite Facility Distributed Active Archive Center Program, NASA

Three optical sensors, including QuickBird, Landsat 7 Enhanced Thematic Mapper Plus (ETM+), and ASTER, were chosen to be complimentary in both spectral and spatial resolutions. QuickBird imagery, available to the public through Digital Globe, was chosen primarily for the extremely high spatial resolution of 0.6 m. Landsat 7 ETM+ was chosen due to popularity among earth observing scientists and for the collection of infrared bands (bands 4, 5, 7). The Landsat 7 ETM+ data set was obtained through Global Land Cover Facility (www.landcover.org). ASTER (Advanced Spaceborne Thermal Emission and Reflection Radiometer) imagery was chosen for the collection of bands sensing in the short-wave infrared (bands 4-9), as well as the high spatial resolution of the very near infrared bands (bands 1-3 have 15-m spatial resolution). Unfortunately, a nighttime scene without cloud cover over the study area is not available, meaning that assessment of the thermal bands for lineament detection is not possible. The ASTER sensor is aboard the NASA Terra satellite and the imagery was available through the NASA EOS Data Gateway.

It is important to note that scene acquisitions dates for the optical data sets were overwhelming controlled by cloud cover severity. For example, of the 27 ASTER daytime scenes available (as of 11/29/2007) for Boaco, only one scene is *mostly* cloud-free. The 15 available ASTER nighttime scenes (as of 11/29/2007) all display cloud coverage over the study area. As a result, this study includes only one scene for each of the optical sensors.

Three RADARSAT-1 scenes were obtained from the Alaska Satellite Facility (ASF) archive. These scenes include two ascending orbits acquired on 9/9/2006 (wet season) and 2/24/2007 (dry season) and one descending orbit acquired on 11/8/1997 (season). All three RADARSAT-1 scenes used in this study were acquired using Standard Beam Mode 3.

A summary of image parameters including acquisition dates and times, image ordering specifications, solar azimuths and elevations, off-nadir look angles, and orbital directions are provided in Table 3.

Table 3: Summary of image parameters. Parameters, including image ordering specifications, acquisition date and time, solar azimuth and elevation, orbital direction of the satellite, and off-nadir look angle, which are specific to each scene are shown.

Sensor	Image Ordering Specifications	Acquisition Date (mm/dd/yyyy)	Acquisition Time (Local Time, hh:mm:ss)	Solar Azimuth (degrees)	Solar Elevation Angle (degrees)	Off-Nadir Look Angle (degrees)
QuickBird	Standard 2A	06/01/2006	11:39:15	54.2	72.5	10.3
ASTER	Level 1 B	11/24/2005	11:16:36	151.1	52.4	-5.7
Landsat7 ETM+	Geolocated and Projected	11/13/2001	10:45:11	142.1	50.9	0.0

Sensor	Image Ordering Specifications	Acquisition Date (mm/dd/yyyy)	Off-Nadir Look Angle (degrees)	Orbital Direction
RADARSAT-1	Standard Beam Mode 3	02/24/2007	29.8	Ascending
	Standard Beam Mode 3	09/09/2006	29.8	Ascending
	Standard Beam Mode 3	11/08/1997	31.7	Descending

Statistics for each scene are reported in Appendix 1 and contain general statistics, correlation and variance-covariance matrices, and image processing statistics (principal components analysis, discussed later). The general statistics show the distribution of brightness values for each band contained in a scene (e.g., minimum and maximum brightness values). Variance-covariance matrices show the relationship between two bands, providing a measure of their interaction, and are calculate for each combination of bands within a scene (Jensen, 2005). Variance-covariance coefficients are calculated using the equation below (Jensen, 2002) and are influenced by units of measure (brightness value, BV, also known as digital number, DN):

$$\mathrm{cov}_{jk} = \frac{\sum_{i=1}^{n} (BV_{ij} - \mu_j)(BV_{ik} - \mu_k)}{n-1}$$

where BV_{ij} = brightness value for the i^{th} pixel in band j (BV)

BV_{ik} = brightness value for the i^{th} pixel in band k (BV)

μ_j = mean of band j (BV)

μ_k = mean of band k (BV)

n = number of pixels

cov_{jk} = covariance coefficient for bands j and k (BV)

The correlation matrices also provide a measure of the degree of interaction between two bands and are also calculated for each combination of bands within a scene. Correlation coefficients are unit-less and range between -1 and +1 (Jensen, 2005). A negative value indicates and inverse relationship, a positive value indicates a positive relationship, and a value of zero indicates no relationship between the two bands (Jensen, 2005). Correlation coefficients are calculated using the covariance coefficients as shown below (Jensen, 2005):

$$r_{jk} = \frac{\mathrm{cov}_{jk}}{s_j s_k}$$

where s_j = standard deviation of band j (BV)

s_k = standard deviation of band k (BV)

r_{jk} = correlation coefficient for bands j and k (unit-less ratio)

A DEM was generated from a paper topographic map (INETER, 1987) by manually digitizing the 20-m contour lines. Using ArcMap "Topo to Raster" tool, a 20-m DEM surface was generated. This tool uses an iterative finite difference interpolation technique which is able to model sharp changes in topography (i.e., cliffs) while minimizing sinks (ESRI ArcMap, 2006). From the DEM, a hillshade surface with a vertical exaggeration of 2x was produced using ArcGIS Surface Analysis Tool. Although digitizing topographic lines is a tedious process, there was no other available high-resolution DEM option for the study area.

3.2 Feature exploitation and detection

3.2.1 Image Processing

RADARSAT-1 images were orthorectified and geolocated with ASF MapReady© Tool (2007) with shadowed and layover areas filled. A simple x, y shift was performed to align images and refine geolocations. Prior to image processing, each image was subset to the extent of the study area, roughly 66 km^2. By creating a subset of an image before executing processing techniques, the unique statistical signature of pixels contained only within the study area can be fully utilized. Processing steps for each original image are provided in Figures 5, 6, 7, and 8. These figures are flow charts that describe the processing path followed to generate various final image products. Final image products are listed in Table 4. All image processing techniques were performed using ERDAS Imagine 9.1 (Lecia Geosystems Geospatial Imaging, LLC. 2006) unless otherwise indicated and are all georeferenced using WGS 1984 and UTM zone 16N. General and PCA statistics are provided in Appendix 1.

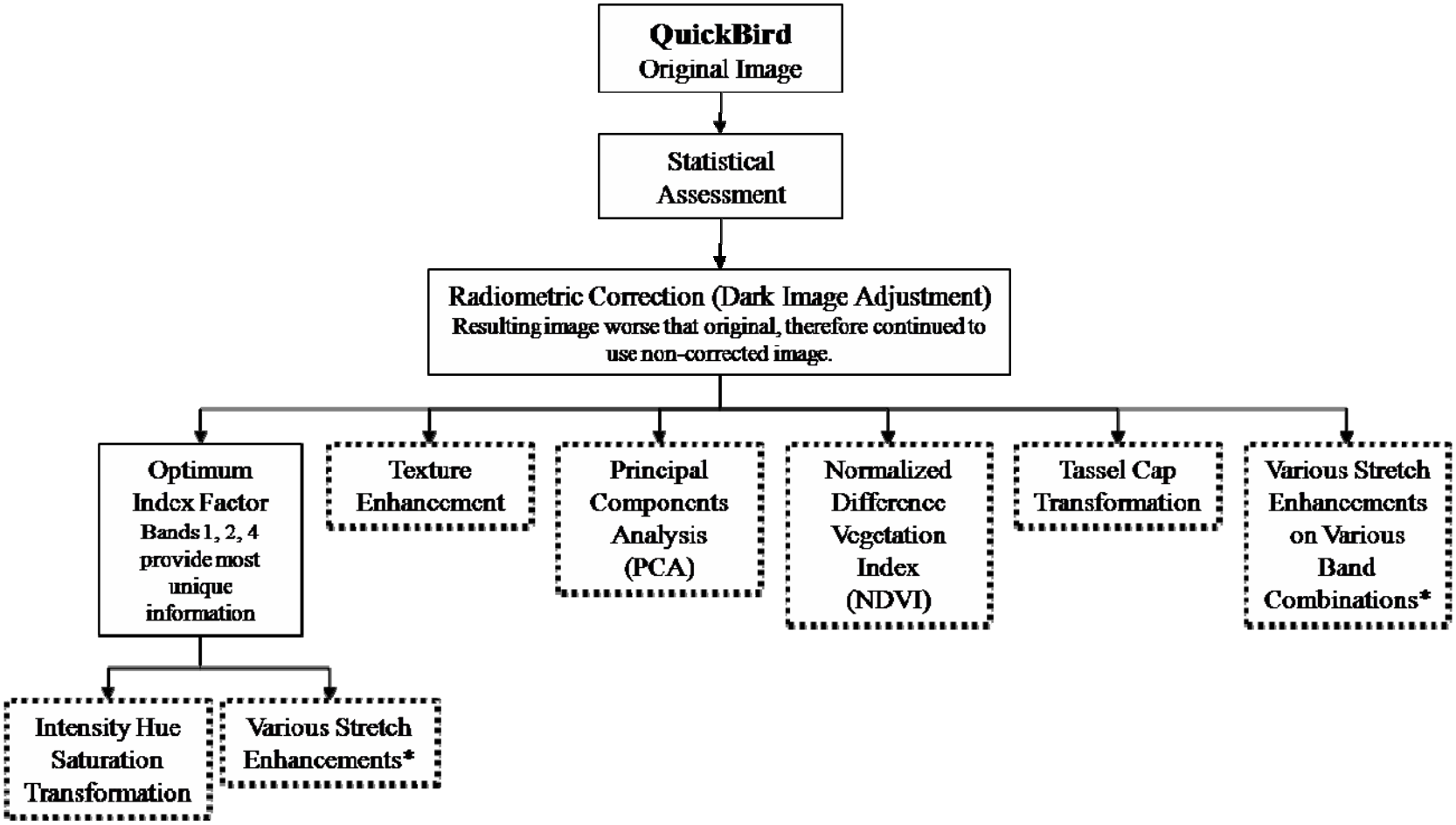

Figure 5: Processing flow for QuickBird image. Dotted boxes indicate production of an image product and are listed in Table 4. An asterisk indicates that more than one image product was created, the most successful of which is included in Table 4.

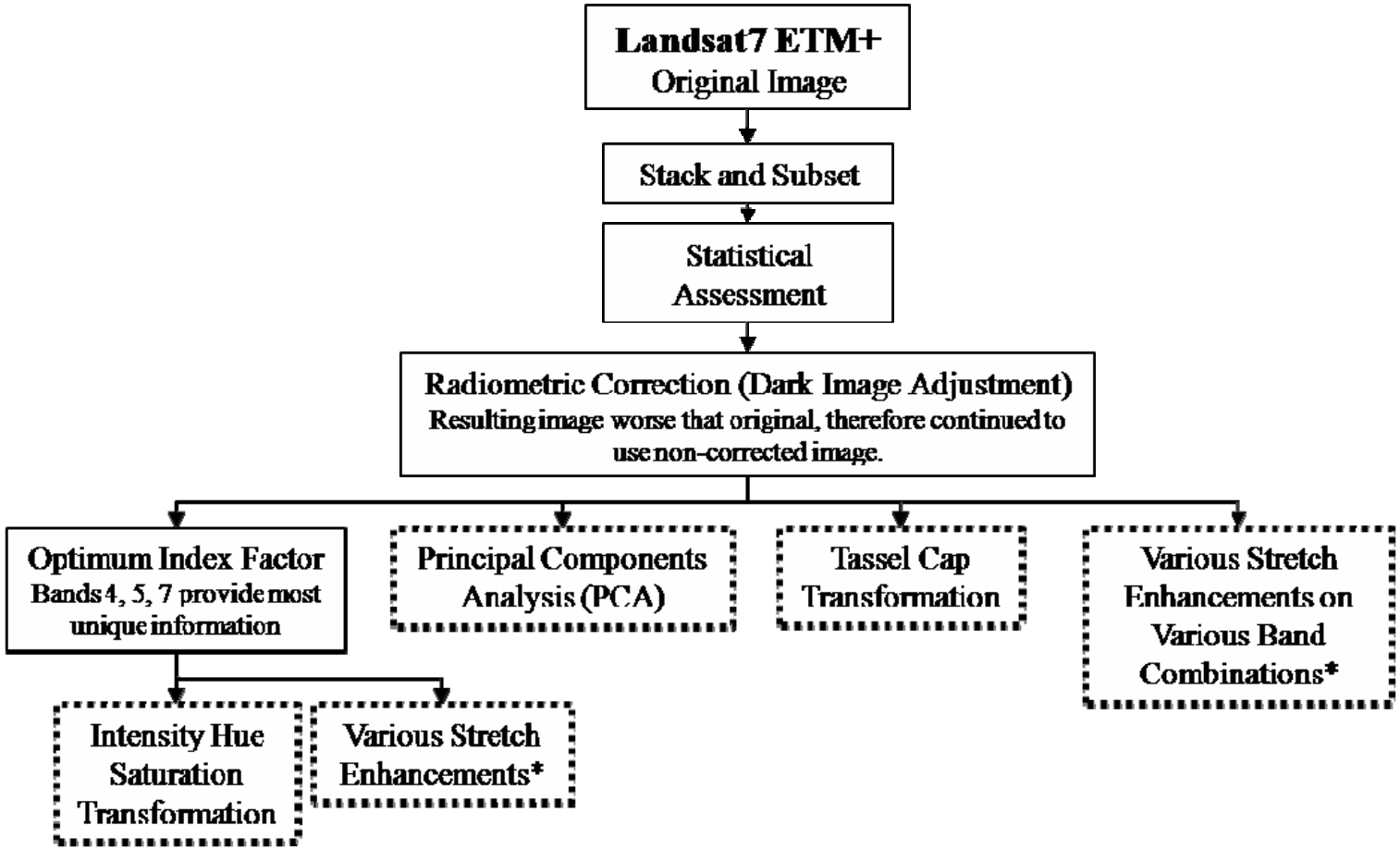

Figure 6: Processing flow for Landsat7 ETM+ image. Dotted boxes indicate production of an image product and an asterisk indicates that more than one image product was created. Image products created by processing Landsat7 ETM+ scene were unsuccessful at exhibiting faulting. Therefore, Landsat7 ETM+ scene was removed from the study and no image products are listed in Table 4.

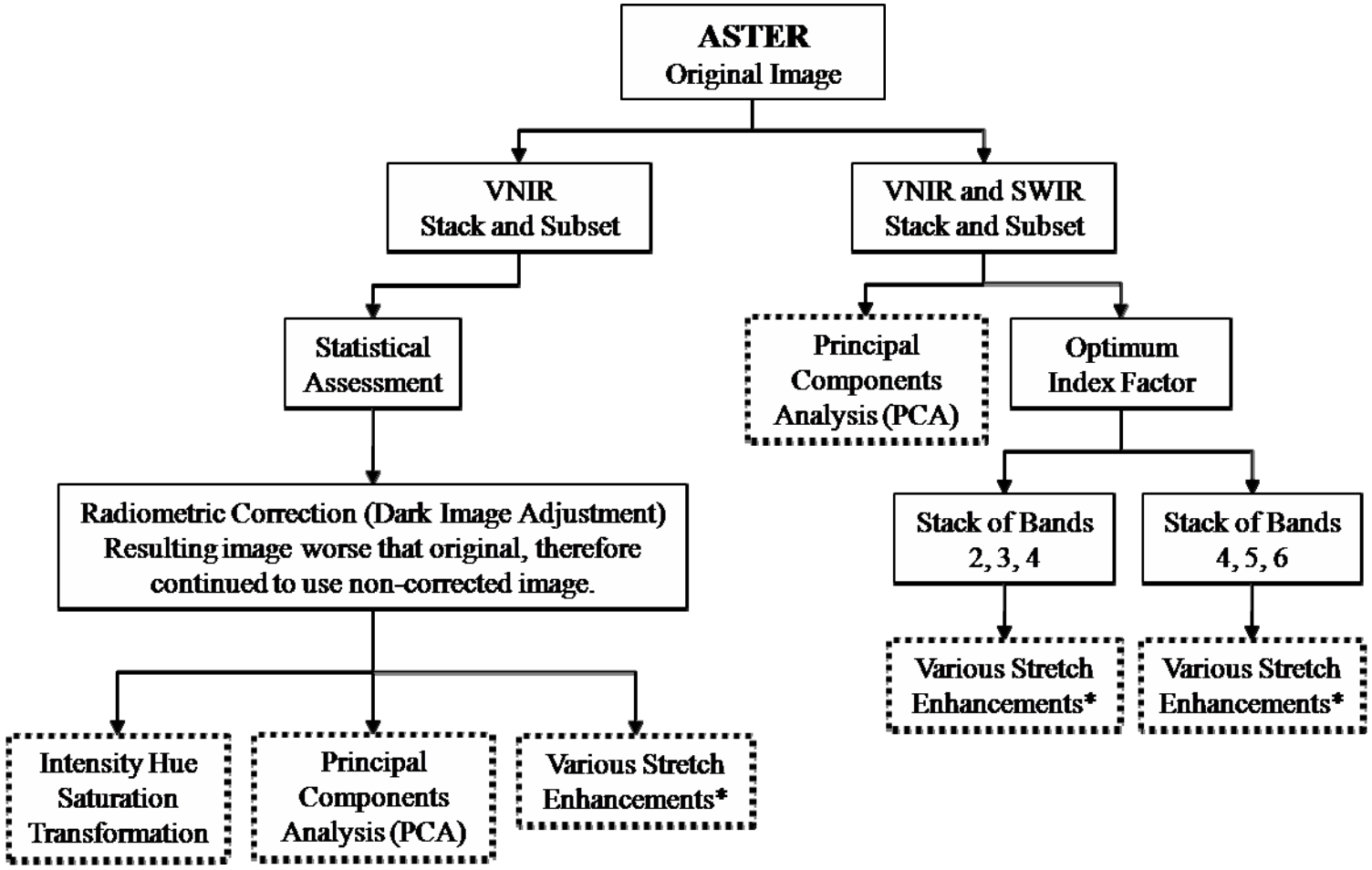

Figure 7: Processing flow for ASTER image. Dotted boxes indicate production of an image product and are listed in Table 4. An asterisk indicates that more than one image product was created, the most successful of which is included in Table 4.

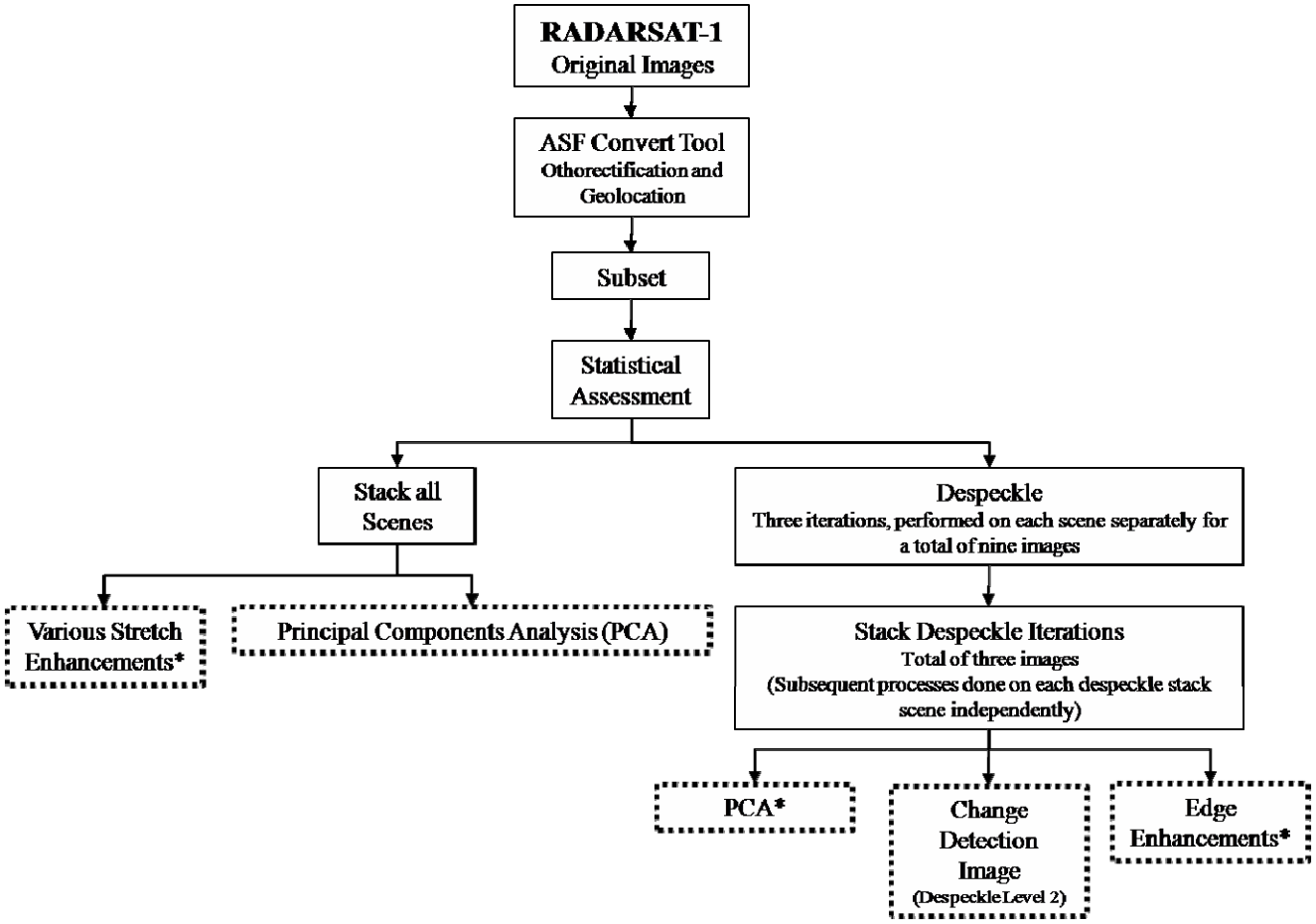

Figure 8: Processing flow for RADARSAT-1 images. Dotted boxes indicate production of an image product and are listed in Table 4. An asterisk indicates that more than one image product was created, the most successful of which is included in Table 4.

Table 4: Assessment of product images for exhibiting faults. The ability of each image product to exhibit faulting in the two dominate directions is ranked as either P = Poor, M = Moderate, or G= Good.

Sensor	Processing Level	150° Trending Faults	70° Trending Faults
ASTER	VNIR Stretch Enhancement – Std. Dev. (1.5)	M	M
	band 1	M	M
	band 2	M	P
	band 3	P	M
	VNIR PCA	P	M
	P C 1	P	M
	P C 2	P	M
	P C 3	P	P
	VNIR IHS	P	P
	I	P	P
	H	P	P
	S	P	P
	VNIR and SWIR Stack		
	band 4	P	M
	band 5	P	P
	band 6	P	P
	band 7	P	P
	band 8	P	P
	band 9	P	P
	VNIR/SWIR PCA		
	Composite of PC 1, 2, and 3	P	P
	P C 1	P	M
	P C 2	P	P
	P C 3	P	P
	P C 4	P	P
	P C 5	P	P
	P C 6	P	P
	P C 7	P	P
	P C 8	P	P
	P C 9	P	P
	OIF (2, 3, 4) Stretch Enhancement - Std. Dev (1.8).	P	P
	band 2	P	P
	band 3	P	P
	band 4	M	M
	OIF (4, 5, 6) Stretch Enhancement - Std. Dev. (1.8)	M	P
	band 4	M	M
	band 5	P	P
	band 6	M	P

Table 4: Assessment of product images for exhibiting faults - continued

Sensor	Processing Level	150° Trending Faults	70° Trending Faults
QuickBird	Original Image Stretch Enhancement - Std. Dev. (1.6)	M	P
	band 1	P	P
	band 2	P	P
	band 3	M	P
	band 4	M	P
	PCA		
	Composite of PC 1, 2, and 3	M	P
	P C 1	M	P
	P C 2	M	P
	P C 3	M	P
	P C 4	P	P
	Texture Enhancement	P	P
	Tassel Cap		
	T C 1	P	P
	T C 2	P	P
	T C 3	P	P
	T C 4	P	P
	OIF (2, 3, 4) Stretch Enhancement – Std. Dev. (1.8)	M	P
	band 2	P	P
	band 3	M	P
	band 4	M	P
	IHS (2, 3, 4)	P	P
	I	P	P
	H	P	P
	S	P	P
	NDVI	M	M
RADARSAT-1	Stack of Scenes Stretch Enhancement – Std. Dev. (2)	G	M
	Original Image (Sept.)	M	M
	Original Image (Nov.)	P	M
	Original Image (Feb.)	P	P
	Despeckle - 1st Iteration	G	M
	Despeckle - 2nd Iteration	G	M
	Despeckle - 3rd Iteration	G	M
	PCA	G	M
	PC 1	G	M
	PC 2	M	P
	PC 3	P	P
	PC 1, 1st Despeckle	G	M
	PC 1, 2nd Despeckle	G	M
	PC 1, 3rd Despeckle	M	M
	Change Detection (Image Sub)	G	G
	Edge Enhancements		
	NW Filter	P	M
	NE Filter	M	P
	SW Filter	M	P
	SE Filter	M	P
	Non-directional	M	P
DEM	Topographic lines	M	M
	Hill shade, z=2	M	M

The ASF MapReady© Tool (2007) was used to orthorectify and geolocate the RADARSAT-1 scenes prior to subsetting and it requires a digital elevation model (DEM) equal to or larger in extent than the scenes. A mosaic of four 90-m Shuttle Topography Radar Mission (STRM) (USGS 2000) DEMs was necessary to meet this spatial requirement and was created using ERDAS Imagine. Data gaps in the STRM DEM were filled using ERDAS Imagine Immediate Surface Interpolation Tool, which uses a 2nd order polynomial function with 1024 sample points, to produce complete DEM coverage. These "holes" in the original DEM are areas of pixels containing no data usually existing as clusters of fewer than 10 pixels and are inherent to STRM DEM data sets of remote regions around the world.

The despeckling procedure used for the RADARSAT-1 data set is outlined in ERDAS Imagine Radar Tutorial (Lecia Geosystems Geospatial Imaging, LLC) and is a smoothing operation to decrease backscatter noise (speckle). This process involves three iterations of despeckling where the averaging window increases in size for sequential iterations and the coefficient of variation is calculated at each step to create the output image. The coefficient of variation is a measure of the distribution of data points around a mean and decreases in value with sequential iterations. This procedure was performed on each scene individually. Products from each despeckling iteration were then stacked. For example, three RADARSAT-1 scenes produced three 1st iteration products, which were stacked to create a single composite image of the 1st iteration. However, each of the three 1st iteration products was used individually to create the three 2nd iteration products, and so on.

Image differencing was used to compare the wet and dry season RADARSAT-1 images, thus creating a change detection product. This technique employs a simple band math operation where one image is subtracted from the other. In this case, the change detection product was created by subtracting the wet season image (acquired 9/9/06) from the dry season image (acquired 2/24/07).

Intermediate results of Landsat 7 ETM+ image processing were proving less successful in exhibiting faulting over all three other image types. At this point, the Landsat 7 ETM+ sensor was removed from the study and therefore no lineament interpretations were performed using these image products.

3.2.2 Initial Evaluation of Image Products

A substantial number of product images were created by employing various processing techniques and it is therefore impractical to attempt lineament interpretations on all of these images. In order to eliminate images that lack promise for lineament delineation, each image was evaluated for its ability to show faulting in the two primary directions (azimuths 75° and 150°). The ability of an image to exhibit the two fault directions was ranked as either poor, moderate, or good in a similar fashion to the work presented by Krishnamurthy et al (1992), examples of which are provided in Appendix 2. This was achieved by considering each image, as well as each individual band associated with that image, and overlaying known faults digitized from geological map (Office of Cadasters and Natural Resources Inventory, 1971). The results of the assessment are given in Table 4. Products highlighted with grey in Table 4 include data sets accepted for lineament interpretation and are provided in Appendix 3.

3.2.3 Fusion of Image Products

Table 4 was also used to select images for fusion. Fused images include:

- Composite 1: stack of RADARSAT-1 (1) principle component (PC) #1, 1st despeckle iteration, (2) PC #1, 2nd despeckle iteration, and (3) PC #1, 3rd despeckle iteration

- Composite 2: stack of (1) RADARSAT-1 PC #1, 2st despeckle iteration (2) RADARSAT-1 change detection, and (3) ASTER band 1. Prior to stacking

these images, both RADARSAT spatial resolution had to be degraded from 12.5 m to 15 m in order to match ASTER spatial resolution.

None of the QuickBird products were selected for fusion with another sensor product for two reasons. First, the fusion process would require severe degradation of the QuickBird scene's spatial resolution to match the spatial resolution of the other images. For example if a QuickBird product was to be fused with a RADARSAT-1 product, the QuickBird's spatial resolution would need to be degraded from 0.6 m to 12.5 m. Secondly, bands 2, 3, and 4 of QuickBird have almost the same spectral resolution of ASTER bands 1, 2, and 3, see Table 2. This means that the using a QuickBird product for image fusion would not provide a significant amount of new information, if any, than an ASTER product would provide for the same image fusion.

3.2.4 Lineament Interpretation

Each image highlighted in grey in Table 4 was interpreted individually for lineaments. This was done in a visual manner using ArcGIS to display imagery and actively digitize lineaments. An advantage of using GIS software, such as ArcGIS, for lineament interpretations is that ArcGIS enables the user to change viewing scales so that features of any extent (regional or local) can be easily visualized. Besides the QuickBird image (discussed in the following paragraph), all images were interpreted only once for lineaments.

The QuickBird image, displaying band combination 1, 3, 4, was interpreted multiple times to test for reproducibility, similar to the methods described by Magowe et al (1994). Three different interpreters produced lineament interpretations separately for the entire scene. Additionally, one of these interpreters analyzed the scene two more times at an interval of two or more weeks between interpretations. The result is five visual lineament interpretations for the

QuickBird scene to assess reproducibility between multiple observers and a single observer, multiple trials.

3.3 Evaluation

3.3.1 Field Campaign

A field campaign to Boaco, Nicaragua occurred in March 2008, corresponding to the latter part of the dry season. The objective of field work was to evaluate lineament interpretation results by: (1) performing visual inspection of lineaments, and (2) executing pump tests.

3.3.1.1 Visual Inspection of Lineaments

Initially, lineament validation occurred by seeking out remotely sensed lineaments in the field and observing local field characteristics, such as drainage control, topographic situation, and vegetation type and health. This method introduced bias as only lineaments interpreted prior to the field campaign were inspected and did not account for lineament-like features existing in the field missed during lineament interpretation. Therefore, lineament validation was altered to identify lineament like features in the field without location guidance from lineament interpretation maps. Lineament validation was limited by accessibility and time, therefore only regions accessible via road were inspected for lineament occurrence. Thus, only a subset of lineaments interpreted prior to the field campaign were inspected in situ. Field-observed lineament locations were marked using a global positioning system (Garmin GPSmap76) and characteristics were recorded. Digital photographs (Sony Cyber-shot 5.1 mega pixels) of observed lineaments were taken, provided in Appendix 3. The positions of ground observed lineaments were displayed in GIS as a 200 m long line oriented at the surveyed strike of the feature. The 200 m length was chosen solely for display purposes.

3.3.1.2 Pump Tests

Carroll (2006) cataloged wells in the municipality of Boaco and surrounding communities, noting well type and location, creating the first well inventory for the city. Using this catalog and by traveling around Boaco and neighboring communities and talking to local residents (more wells have been drilled since the Carroll (2006) study), wells suitable for pump tests within the study area were located. Suitable wells include those that are drilled, have access to the borehole and cooperation with owner and/or local community members. A survey, provided in Appendix 4, was completed for every drilled well to assess pump test feasibility, results of which are summarized in Table 5.

In total, nine wells were chosen for testing, all of which are drilled and the well boreholes are covered with a removable cap as shown in Figure 9. Little is known about these wells as drilling logs are almost always non-existent. A majority of the wells suitable for testing were located near major roads within communities and the spatial distribution of wells is shown in Figure 10.

The methodology for the pump tests used in this study is based on methods developed by Gross (2008). Gross (2008) showed that it was possible to measure well productivity via simple, low-extraction, manual pumping tests on rope pumps in Santa Rita (near Juigalpa), Nicaragua. These tests were reproducible within 80% and 88% using equilibrium approximation and Papadapolous-Cooper solutions respectively, and over estimate specific capacity by 41% as compared to a conventional pump test (Gross 2008).

Table 5: Summary of drilled wells. Information derived from well surveys is summarized in this table. Volumes of water extracted are rough estimates by users of the well, reported as number of households using the well, and assumes six residents per household. Entries highlighted in grey include those wells pump tested.

Well Owner or Community Name	Well Status	Owner Type	Intended Use	Type of Pump	Estimated Volume Extracted (gallons/day)	Pump Test Feasibility
Juana Guzman, NW Boaco	Sealed/Cemented	Private	Household	Rope	50-60	Moderate
Seminary Well, N Boaco	Sealed/Cemented	Private	Household	Rope	?	Poor
Eddie Jose Lopez Davila, SW San Nicolas	Removable Cap	Public	Household	Rope	1000	Moderate
Maria de la Cruz Miranda, SW San Nicolas	Removable Cap	Public	Household	Rope	1500	Good
Maura Padilla, E San Nicolas	Removable Cap	Public	Household	Rope	900	Moderate
E San Nicolas	Removable Cap	Public	Household	Rope	?	Good
Juan Jose Amador Urbina, N San Nicolas	Removable Cap	Public	Household	Rope	2000	Good
N Santa Blanca	Sealed	Private	Irrigation	None	not in use	Good
Santa Blanca	Sealed	Private	Irrigation	None	not in use	Good
S Boaco	Removable Cap	Private	Household	Rope	100	Good
Marisol Martes, Municiple Slaughter House, S Boaco	Removable Cap	Industry	Industrial	Electric	2000	Good
S Paso de Laja	Removable Cap	Public	Household	Rope	?	Good
Fermin Mendosa, Paso de Laja	Removable Cap	Public	Household	Rope	1200	Good
S San Nicolas (A)	Removable Cap	Public	Household	Rope	Combined use of 4500	Good
S San Nicolas (B)	Removable Cap	Public	Household	Rope		Good
Muy Muy/Camoapa/ Boaco highway intersection	Completely Cemented	Public	Household	Rope	?	Poor
Hardware Store, Boaco	Contained in Pump House	Private	Household	Electric	50-60	Moderate
Market Well, Boaco	Contained in Pump House	Public	Household	?	?	Poor

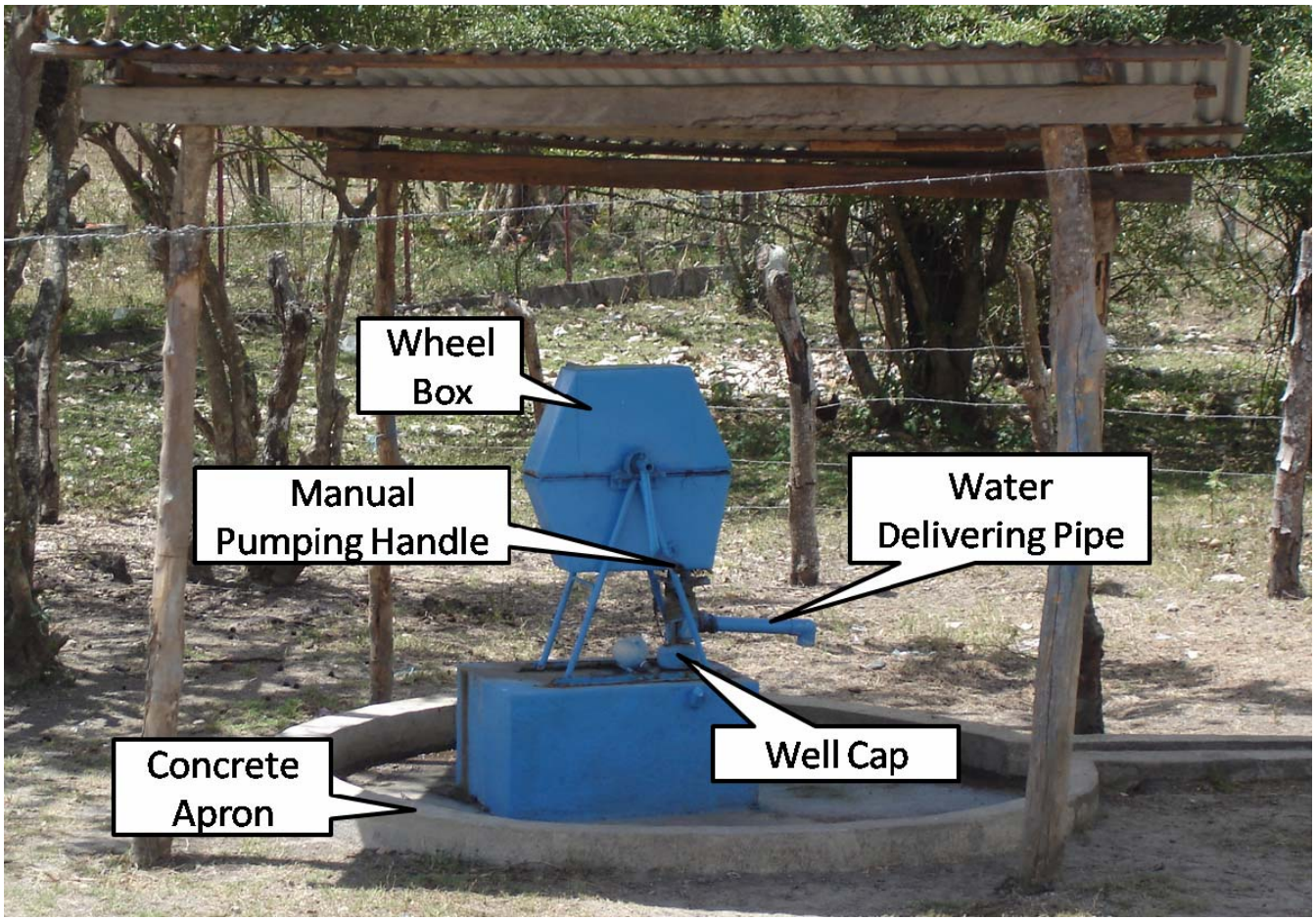

Figure 9: Rope rump for a drilled, perforated well. Access to borehole simply requires lifting the entire rope pump apparatus and sliding up and off the well cap. Photo by author.

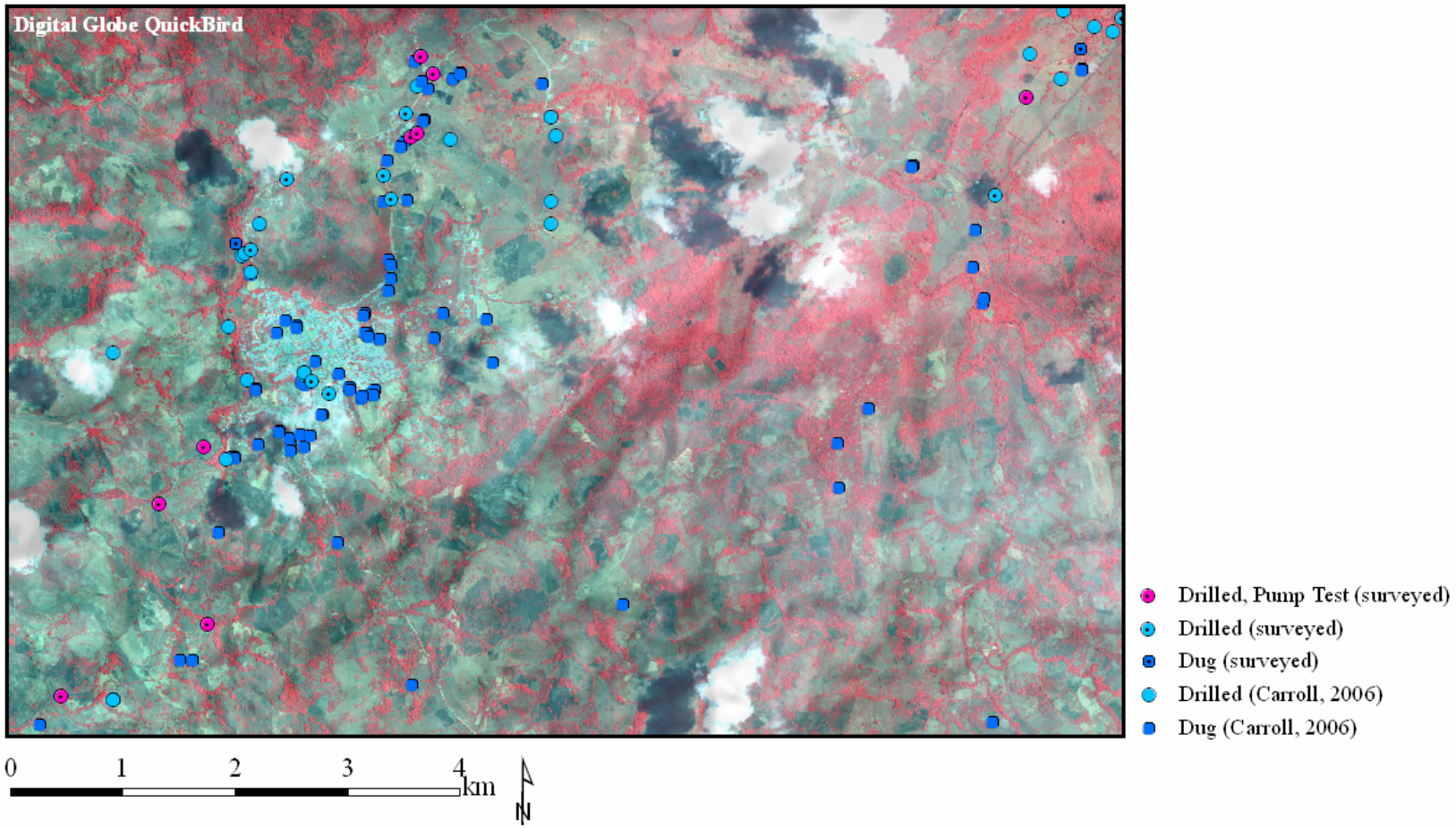

Figure 10: Distribution of wells in study area. Image derived from Digital Globe QuickBird scene (2006). The highest concentrations of wells are located within the city of Boaco and are used primarily for household supply. Wells that were surveyed during the March 2008 field campaign are indicated with a black dot in the center of their icon and those pump tested are shown as purple. Wells cataloged by Carroll (2006) are shown without a black dot.

In general, steps for testing a rope pump well include:

1) Prior preparation with well users
    i) Gain cooperation from owner and/or local community
    ii) Schedule pump test so that:
        (a) The well is not used prior to test for several hours to ensure that water height in the well is at static level
        (b) Community members can plan to fill buckets ahead of time and bring empty buckets to fill with water extracted during pump test

2) Preparation of pump for testing
    i) Remove bolts holding rope pump apparatus to concrete base
    ii) Loosen borehole cap (gentle tapping)
    iii) Lift up entire apparatus and set it on four inch thick concrete blocks
    iv) Measure casing diameter
    v) Deploy sounder to measure static water level

3) Pump test, shown in Figure 11
    i) Begin pumping, record start time
    ii) Continue pumping at a constant rate, measuring water level with sounder and recording volume and fill time for each container
    iii) End pumping when equilibrium is reached, record stop time
    iv) Measure water level recovery with sounder, concluding test when water level is as close as possible to static water level

4) Return pump to original position
    i) set entire pump apparatus back on cement base, re-securing with bolts

Figure 11: Manual pump test in progress. Notice the pump apparatus is set up on blocks, sounder measurements being continuously taken and recorded during pumping, and community involvement. Typically, manual pump tests require five people; two to turn pump, one to deploy sounder, one to organize buckets for filling, and one to record data. Photo by author.

Well characteristics and pump test conditions varied for each of the nine wells and deviations from the above procedure are shown in Table 6. Each well was only tested once, which is justified by the results presented by Gross (2008). Specific conductivity and temperature measurements were made from water samples taken during pumping with a flow through cell. These results are provided in Appendix 5 and are not discussed in this paper.

Table 6: Pump test summary and well conditions. Measurements of water level pre pumping, post pumping, and drawdown are shown. Calculated specific capacity values for each well and the solution method used are given. Deviations from standard pump test procedure are discussed as additional considerations. Wells highlighted in grey lie in hard-rock aquifers, while non-highlighted wells lie in alluvial aquifers of unknown thickness.

Community Name	**Static Water Level Established Prior to Testing?**	**Static Water Level (ft)**	**Total Drawdown at end of Pumping (ft)**	**Residual Drawdown at end of data collection (ft)**	**Specific Capacity (gal/min/ft)**	**Solution Method**	**Additional Considerations and Notes** (All test preformed manually unless otherwise noted)	**Easting Coord. (m)**	**Northing Coord. (m)**	**Ground Elevation of Well (m)**
E San Nicolas	Yes	22.41	8.30*	0.50	**0.4**	Papadopoulos - Cooper	delivery of water to surface stopped near end of pumping (possibly dried up?)	646,856	1,381,579	404
N San Nicolas	Yes	39.80	0.90	0.80	**6**	Equilibrium Approx.	extremely productive well, recovery data difficult to record	646,753	1,381,740	407
Santa Blanca	Yes	21.82	2.60	0.10	**0.8**	Equilibrium Approx.	submersible electrical pump used for testing, level logger data also available	652,145	1,381,375	369
S Boaco	Yes	17.73	42.32*	0.57	**0.08**	Papadopoulos - Cooper	water level drawdown during test was limited by depth rope reached (60 ft)	643,542	1,376,043	310
Municipal Slaughter House, S Boaco	Yes, see note	4.61	7.84	2.19	**1**	Equilibrium Approx.	well pumped electrically for 3.25 hours at 10 gpm by the municipal slaughter house, all data collected during recovery only, static water level established 6 hours after pump turned off	644,846	1,376,678	345
S Paso de Laja	No	27.00 ?	6.05*	2.40	**0.5**	Papadopoulos - Cooper	well had been used prior to test (volume extracted unknown), started pump test without complete recovery because of time limitations, estimated static water level at 27ft	644,421	1,377,746	311
Paso de Laja	No	33.00 ?	9.25*	1.70	**0.1**	Papadopoulos - Cooper	well had been used prior to test (volume extracted unknown), measured recovery from prior use for one hour, started pump test without complete recovery, estimated static water level at 33ft	644,813	1,378,256	300
S San Nicolas (A)	Yes	21.40	6.85	0.10	**0.7**	Equilibrium Approx.	rope began slipping due to too fast of pumping rate	646,666	1,381,020	400
S San Nicolas (B)	Yes	22.41	0.77	1.14	**6**	Equilibrium Approx.	extremely productive well, recovery data difficult to record	646,714	1,381,048	400

* These wells did not reach equilibrium during pumping.

Also shown in Table 6 are solution methods used to calculate values of specific capacity for each well tested. Wells that reached equilibrium during pumping were solved using equilibrium approximation method:

$$F = \frac{Q}{s_w}$$

where F = specific capacity (gpm/ft)
Q = pumping rate (gal/min)
Δs = total drawdown (ft)

For wells that failed to reach equilibrium during pumping, parameters were solved graphically using the Papadapolous-Cooper solution in AQTESOLVE (HydroSOLVE, Inc. 2007). This solution was chosen because it considers both drawdown and recovery data as well as effects of casing storage. All aquifers are assumed to be confined and aquifer thickness was assumed to be 200 ft (estimate depth of wells) less the static water level. The effects down-hole equipment has on casing storage were ignored, as this value is negligible in this study. The fit curve was manipulated manually by adjusting values of storativity, transmissivity, and borehole radius. These values are candidates for manipulation because no previous measurements of storativity and transmissivity have been recorded in the study area nor are drilling records containing borehole radii available for tested wells. Final transmissivity values were then used to calculate specific storage using the Cooper-Jacob approximation:

$$F = \frac{T}{264 \log \frac{0.03Tt}{r_w^2 S}}$$

where F = specific capacity (gpm/ft)

T = transmissivity (gpd/ft)

t = time since pumping began (min)

r_w = well casing radius (in)

S = storativity

3.3.2 GIS Analysis

The goals of GIS analysis were to synthesize the large amount of data resulting from lineament interpretations and pump tests, provide an objective method in filtering multiple lineament interpretations for a study area that lacks reliable geological and hydrological knowledge, and determine which image product type results in the best lineament interpretation. Geographical Information Systems (GIS) was chosen as the means to bring together data sets and perform the necessary spatial analysis of the lineament interpretations and pump test data to rank imagery types for their lineament delineation abilities. Additionally, GIS facilitates graphical displays of end results, primarily in the form of maps, which permits results to be easily shared with municipality officials in the study area.

A total of sixteen lineament interpretations were created from multiple images (eleven images) and from the multiple interpretation trials and observers (performed only on the QuickBird image, three observers, one repeat observer with three trials). A filter was designed to decrease the number of observed lineaments in each individual interpretation to include only coincident lineaments. According to Magowe and Carr (1997), a coincident lineament is a lineament which has been interpreted in either two or more image types, interpretation trials, or observers (i.e., coincidence number = 2). The steps involved in the filter process include (1) compute acceptable

lineament interpretation buffer width representing the “fracture zone”, (2) check of all lineament interpretations, (3) GIS analysis to filter interpretations, and (4) image performance assessment.

The lineament interpretation buffer width represents the fracture zone and therefore the area in which a lineament interpretation is acceptable. The width was determined using the QuickBird imagery because of the very fine spatial resolution of the sensor, thus producing the most accurate width measurements. Digitized faults were overlain on the QuickBird image. Attributes exhibited by the QuickBird image nearby these faults, such as tonal variations in the soil and vegetation, were observed. Distances across (perpendicular to) the faults where measured. In all, twenty-four measurements were made in areas where the exhibition of fracture-like features in the QuickBird image is distinct. The average width is 172 m, with a standard deviation of 56 m (56 m on the ground is equal to approximately 93 QuickBird pixels, 4.5 RADARSAT-1 Standard Beam Mode pixels, and 3.7 ASTER VNIR pixels). It should be noted that the width measurements made are most likely larger than the fracture zones they represent due to extensive weathering in the study area.

A final check of all the interpretations was completed to ensure interpretation quality and completeness, as well as to ensure the lineament shapefiles were error free before entering into the filtering process.

A buffer polygon shapefile with a width of 172 m was computed for every lineament in each interpretation. These shapefiles, which are vector files, were changed to raster format and reclassified into binary rasters. All binary rasters (16 in all) were then added together. The resulting raster, called the coincidence raster, shows the number of times a lineament was detected and is considered the coincidence level. Because the coincidence raster was created from the original 16 lineament interpretations, it is visually overwhelmed by the level of detail present in the QuickBird image interpretations. A second coincidence raster was created by adding all the binary raster except those created from QuickBird interpretations, thus reducing the number

of input raster from 16 to 11. This resulted in a coincidence raster that is much more visually acceptable; refer to Appendix 6 for figures associated with this process. Unlike Magowe and Carr (1997), a coincidence level = 4 was used in this study as the threshold to detect lineaments that are coincident. This level was chosen because several of the lineament interpretations used as input for creating the coincidence raster were made from similar image products. For example, three individual interpretations produced from RADARSAT-1 products are very similar, including interpretations from the stack of all original RADARSAT-1 scenes and the despeckled products (levels 2 and 3). Agreement with the coincidence raster at a coincidence level = 2 is therefore definite in these cases. To remove bias inherent to the coincidence raster, coincidence raster values ≤ 3 were removed and a binary coincidence raster was created to include only areas having a coincidence level ≥ 4. Sliver polygons of areas < 60,000m^2 were removed from the coincidence raster shapefile because these areas would allow lineaments of minor extent to pass through the filter. This binary coincidence raster was then converted back into a polygon shapefile and every original lineament interpretation was clipped by this polygon. Details concerning the steps taken in the GIS analysis beyond this discussion are contained in Appendix 6.

Finally, specific capacity values resulting from the pump tests were displayed in combination with the coincidence raster for qualitative comparison, Figure 12.

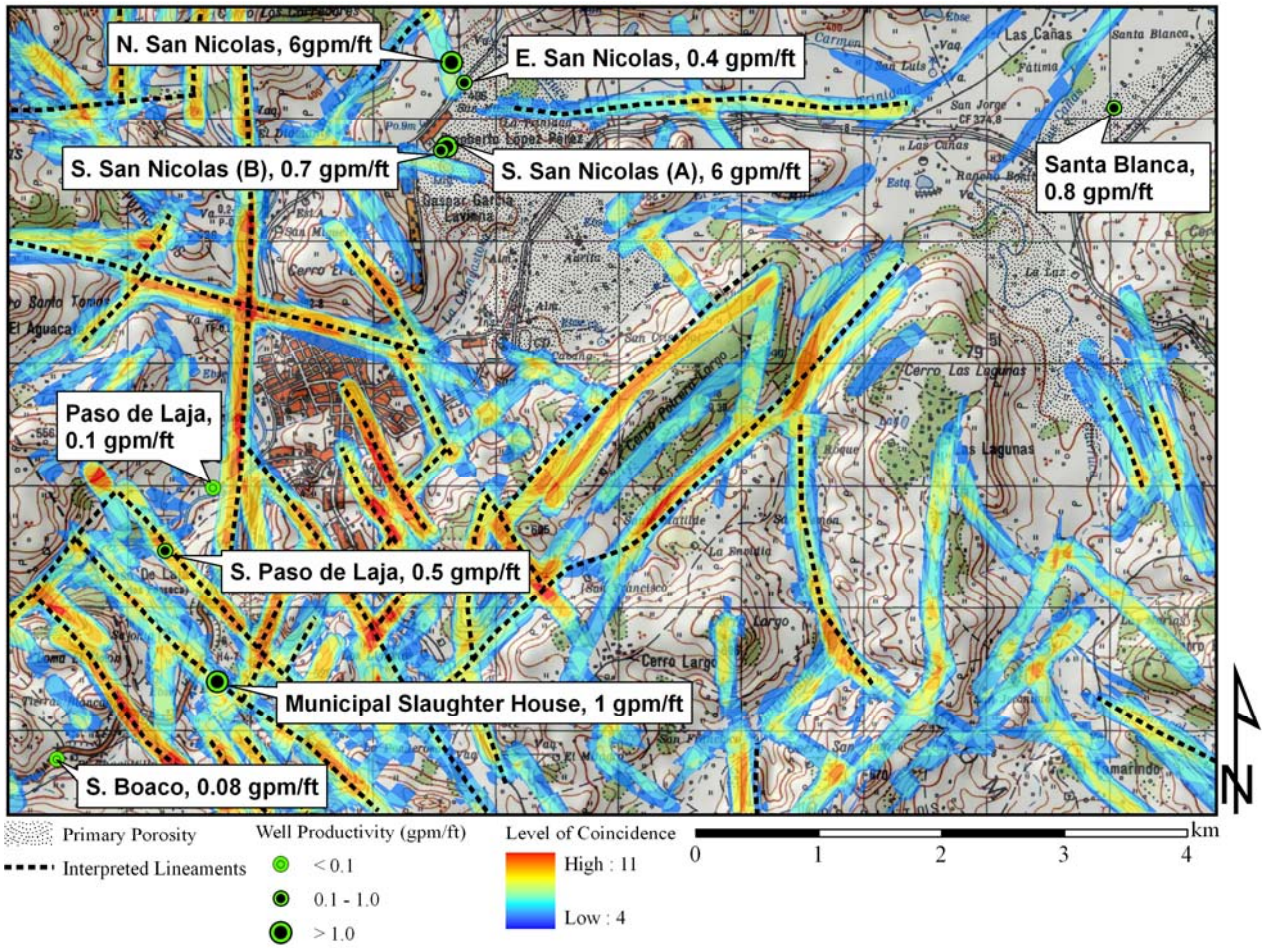

Figure 12: Well productivity and relationship with coincidence raster. Topographic Map adapted from INETER (1987), hillshade derived from INETER (1987). Well productivities are displayed gradationally in order of magnitude; refer to Table 6 for exact values. Of the nine wells tested, four were located in hard-rock aquifers. Of these four, there is a positive correlation between well productivity and proximity to an interpreted fault.

4.0 Results and Discussion

The ability of the various image products to produce acceptable lineament interpretations were assessed in two complementary ways: (1) determine how much of the original lineament interpretation is explained in the coincidence raster filter – an overlap comparison of the original interpretation and filter, and (2) examine the degree to which an original interpretation survived the filtering process – a before and after comparison of the lineament interpretation alone. These two assessment methods use area calculations of the original lineament buffer ("before"), filtered lineament buffer ("after"), and the coincidence raster ("filter") polygon shapefiles. Results of the two assessment methods are given in Tables 7 and 8, respectively. Figure 13: A – P provide illustrations comparing each original lineament interpretation to the coincidence raster and allow for visual assessment of these results. It can be seen from Tables 7 and 8 that RADARSAT-1 products ranked the highest overall for producing acceptable lineament interpretations.

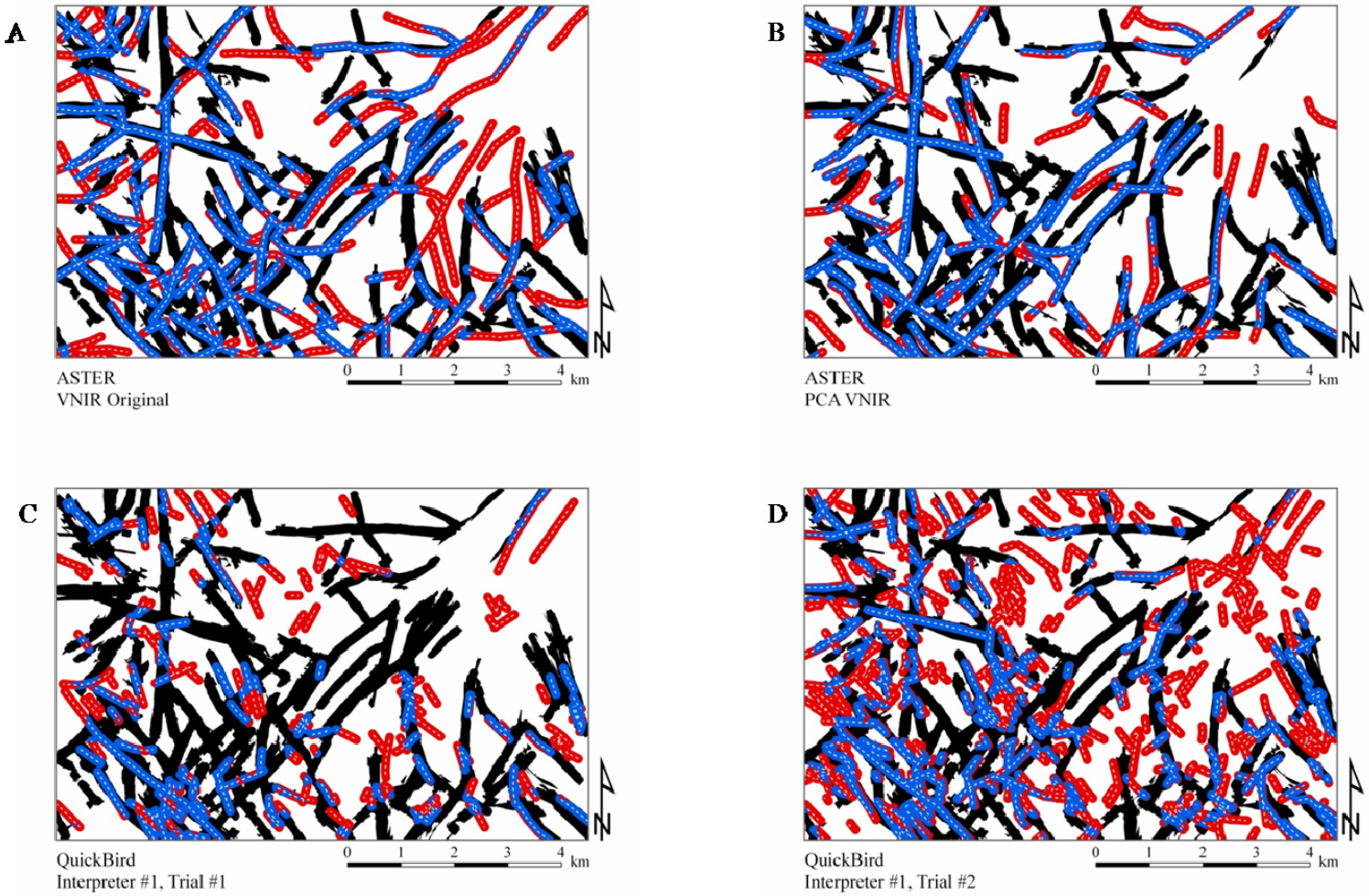

Figure 13 A-P: Level of agreement between original interpretations and the coincidence raster. Original lineament interpretations are display as white dashed lines surrounded by a 172m wide buffer in red. Black areas represent the coincidence raster. Locations where the coincidence raster and original lineament buffer overlap are shown in blue.

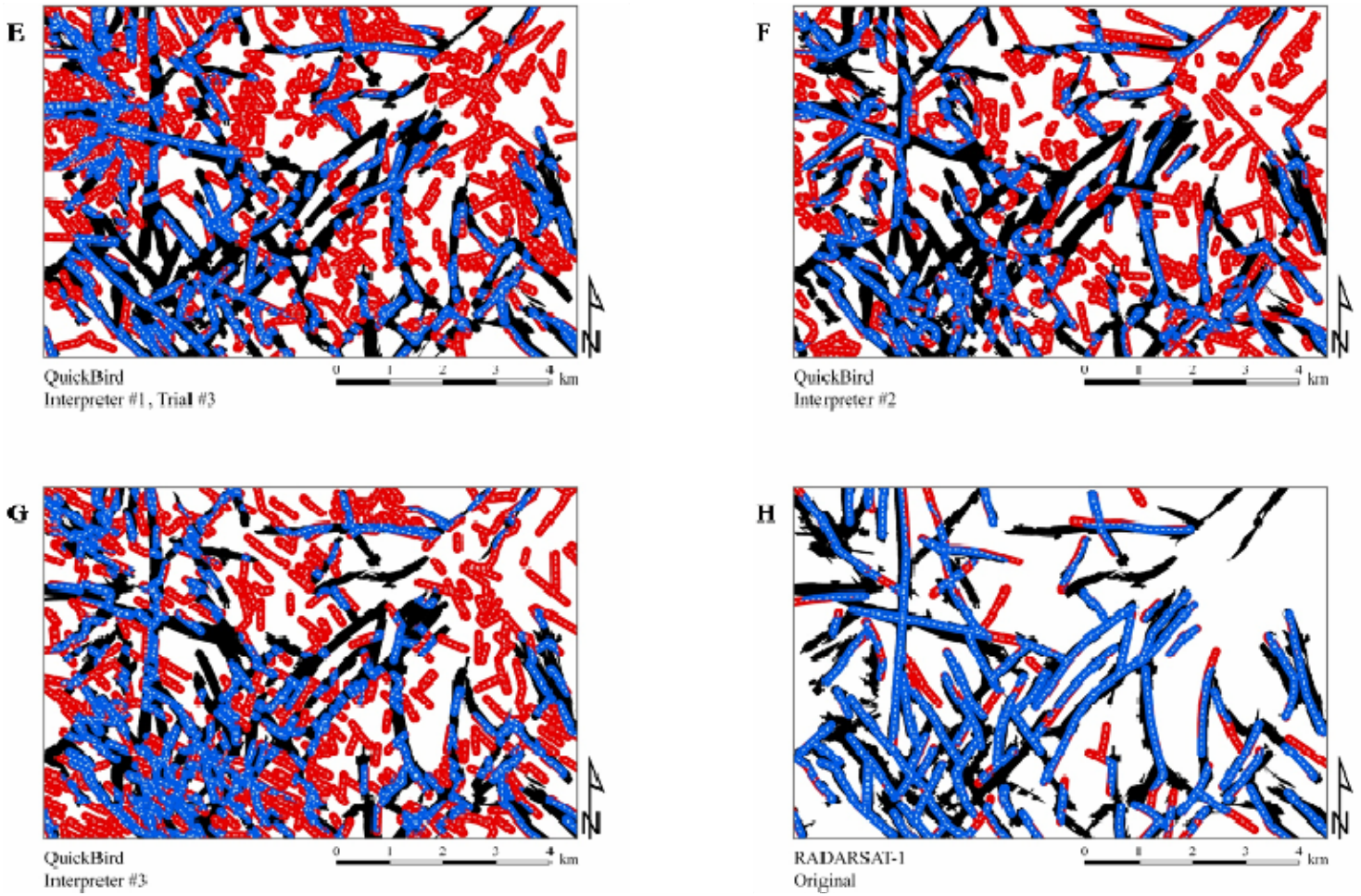

Figure 13 A-P: Level of agreement between original interpretations and the coincidence raster – continued.

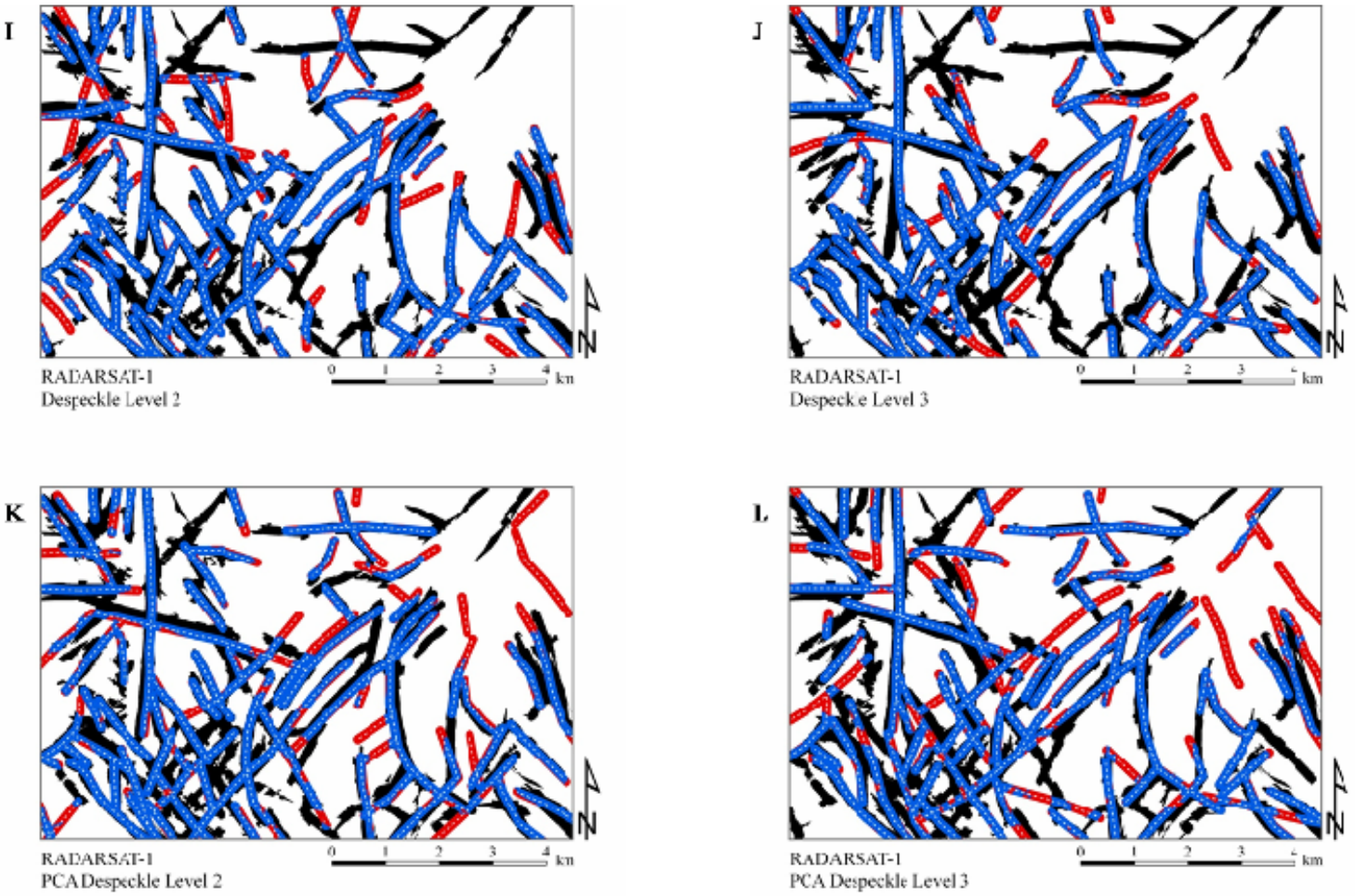

Figure 13 A-P: Level of agreement between original interpretations and the coincidence raster – continued.

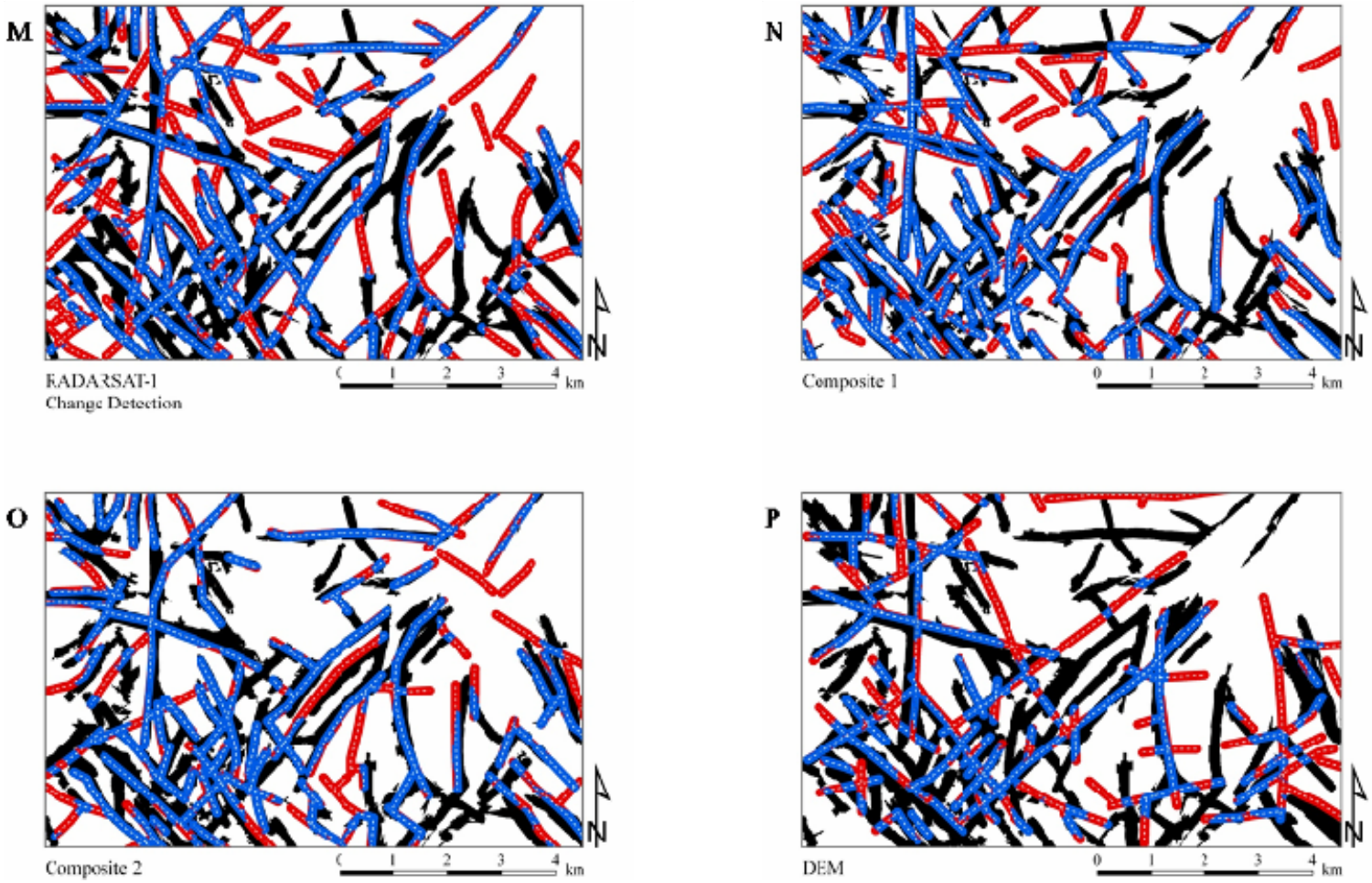

Figure 13 A-P: Level of agreement between original interpretations and the coincidence raster – continued.

Table 7: Image product rank, based on total area of filtered lineament buffer compared to area of coincidence raster buffer. The total area of filtered lineament buffer includes those buffer areas of the original lineament interpretation that are the same as (overlap) areas of the coincidence raster buffer. Therefore the % of lineament area retained calculates the percent of the coincidence raster buffer area is overlapped by a given lineament interpretation.

Sensor/Source	Product	Total area of **filtered** lineament buffer (m^2)	% of lineament area retained	Image rank
RADARSAT-1	Despeckle Level 2	15,666,092	62.8%	**1**
RADARSAT-1	PCA Despeckle 2	15,435,604	61.9%	**2**
QuickBird	Interpreter #3	15,246,142	61.2%	**3**
RADARSAT-1	PCA Despeckle 3	15,153,675	60.8%	**4**
RADARSAT-1	Original	15,032,505	60.3%	**5**
RADARSAT-1	Composite 1	14,944,564	60.0%	**6**
RADARSAT-1	Despeckle Level 3	14,299,222	57.4%	**7**
QuickBird	Interpreter #1, Trial #3	14,273,043	57.3%	**8**
RADARSAT-1 and ASTER	Composite 2	13,709,411	55.0%	**9**
ASTER	Original VNIR	13,669,722	54.8%	**10**
RADARSAT-1	Change Detection	13,431,805	53.9%	**11**
QuickBird	Interpreter #2	12,349,619	49.5%	**12**
QuickBird	Interpreter #1, Trial #2	11,776,477	47.2%	**13**
ASTER	VNIR PCA	11,751,611	47.1%	**14**
Topographic Map	DEM	9,002,583	36.1%	**15**
QuickBird	Interpreter #1, Trial #1	6,828,349	27.4%	**16**
area of coincidence raster buffer		*24,928,193*	*100.0%*	

Table 8: Image product rank, based on total area of original lineament buffer compared to total area of filtered lineament buffer. The total area of original lineament buffer is the area of the original buffered lineaments before filtering. The total area of filtered lineament buffer includes those buffer areas of the original lineament interpretation that are the same as (overlap) areas of the coincidence raster buffer. Therefore the % of lineament area retained calculates the percent of the original buffer area that survived the filtering process for a given lineament interpretation.

Sensor/Source	Product	Total area of **original** lineament buffer (m^2)	Total area of **filtered** lineament buffer (m^2)	% of lineament area retained	Image rank
RADARSAT-1	Radar Despeckle 3	17,055,282	14,299,222	83.8%	**1**
RADARSAT-1	Original	18,329,695	15,032,505	82.0%	**2**
RADARSAT-1	Radar Despeckle 2	19,276,762	15,666,092	81.3%	**3**
RADARSAT-1	Radar Despeckle 2 PCA	19,621,685	15,435,604	78.7%	**4**
RADARSAT-1	Radar Despeckle 3 PCA	20,203,106	15,153,675	75.0%	**5**
RADARSAT-1 and ASTER	Composite 2	19,312,012	13,709,411	71.0%	**6**
RADARSAT-1	Composite 1	21,312,422	14,944,564	70.1%	**7**
ASTER	VNIR PCA	17,290,531	11,751,611	68.0%	**8**
RADARSAT-1	Radar Change Detection	22,354,497	13,431,805	60.1%	**9**
ASTER	Original VNIR	23,291,573	13,669,722	58.7%	**10**
Topographic Map	DEM	15,886,263	9,002,583	56.7%	**11**
QuickBird	Interpreter #1, Trial #1	13,318,755	6,828,349	51.3%	**12**
QuickBird	Interpreter #1, Trial #2	26,273,860	11,776,477	44.8%	**13**
QuickBird	Interpreter #3	34,466,403	15,246,142	44.2%	**14**
QuickBird	Interpreter #2	28,315,462	12,349,619	43.6%	**15**
QuickBird	Interpreter #1, Trial #3	34,366,485	14,273,043	41.5%	**16**

Assessment method (1) shown in Table 7 ranked RADARSAT-1 Despeckle Level 2 product as the best with 62.8% of the original lineament interpretation overlapping with the coincidence raster and is displayed Figure 13: I. This assessment method is biased towards image products that tend to over-interpret as numerous lineament segments will inherently overlap the coincidence raster more often. Such segments do not necessarily have the same orientation as overlapping segments of the coincidence raster and therefore are not identifying the same lineament. This means that if the total area of original lineament buffers is large, the percent retained also tends to be large and is especially evident in all QuickBird interpretations displayed in Figure 13: C – G. These findings further justify the decision not to include interpretations from the QuickBird image for creation of the coincidence raster. Assessment method (2) shown in Table 8, Figure 13: J ranked RADARSAT-2 Despeckle Level 3 product as the best with 83.8% of the original lineament interpretation surviving the filtering process. Unlike assessment method (1), assessment method (2) is biased towards image products that tend to under interpret as this method is only considering original interpretations before and after the filter and does not account for lack of observing lineaments contained in the coincidence raster. These biases are overcome by considering results from both assessment methods simultaneously.

Image rank results show poor performance by the optical sensor products, suggesting that optical sensor types are not appropriate for lineament delineation in this type of study area. One explanation for this can be seen in Table 4, which assesses the ability of each image product to exhibit faulting in the two primary directions. QuickBird products exhibit NW/SE faulting better than NE/SW faulting where as ASTER products exhibit NE/SW faulting better than NW/SE faulting, however neither QuickBird nor ASTER are classified as “good”, if at all, at exhibiting either faulting direction. This implies that solar illumination conditions for each optical scene control what features can be seen. Features striking perpendicular to solar illumination direction are much more observable due to enhancement of topography contrasts, which may be associated with faulting.

Conversely, the sun suppresses features striking parallel to solar illumination direction because the down-strike illumination minimizes topographic contrasts. The QuickBird scene was acquired with a solar azimuth of 54.2°suppressing NE/SW faulting, whereas the ASTER scene was acquired with a solar azimuth of 151.1° suppressing NW/SE faulting (refer to Table 3) as observed in Table 4.

Another explanation for the poor performance of the optical sensor products is that optical images in tropical climates are visually dominated by vegetation patterns. Vegetation is very reflective in the portion of the electromagnetic spectrum employed by ASTER band 3 and QuickBird band 4. These bands show significantly more variation in brightness values over the other bands in each sensor and thus load heavily into principal component 1. This is shown in the image statistics provided in Appendix 1. Vegetation patterns in Boaco are manipulated by both anthropogenic conditions and location of drainages. Anthropogenic conditions cause linear alignments of vegetation to follow field boundaries and roads and are not reflective of subsurface structure. It is typically difficult to distinguish between these two types of vegetation occurrences in remotely sensed imagery, especially imagery of moderate spatial resolution. This further reduces the value of optical products to detect geological faults as many of the lineament interpretations based on vegetation are not true lineaments.

The image ranks show that ASTER products out performed almost all of the QuickBird interpretations for assessment methods (1) and (2), respectively. With the spectral resolutions of ASTER VNIR bands and QuickBird bands 2 – 4 being nearly identical, the major difference between these two data sets is spatial resolution (Table 2). The results indicate that the 15m spatial resolution present in ASTER VNIR bands must provide the right level of detail; whereas QuickBird 0.6-m spatial resolution is too detailed and causesover-interpretation of the imagery. This implies that lineament interpretations cannot be performed on small scales because these interpretations are primarily of limited extent and miss regional features important to groundwater flow Figure 13 C- G. On the other hand, ASTER SWIR bands and

Landsat 7 EMT+ have spatial resolutions of 30 m, which provided too little detail to observe even the regional faults. Additionally, poor performance of the Landsat 7 ETM+ scene is likely due to bands 5 and 7 not containing information exhibited by fault features. Landsat 7 ETM+ bands 5 and 7 are the only bands containing unique information as the spectral resolution of bands 1 – 4 and 2 – 4 are almost identical to QuickBird bands 1 – 4 and ASTER bands 2 – 4, respectively (Table 2).

In this study area, there is not much that can be done to get around the downfalls of using optical imagery. Advanced image processing, including the successful processing techniques identified by Krishnamurthy et al. (1992) study (described earlier), does not show significant improvement in the products' ability to exhibit faulting. Regular cloud cover innate to a tropical climate results in few satisfactory images. This hinders choice of scene acquisition date making it practically impossible to obtain desirable solar parameters or to perform change detection. Moreover, spectral resolutions employed by the optical sensors are remarkably similar and provide little unique information.

On the other hand, these results show that RADARSAT-1 products overcome many of the downfalls inherent to optical imagery, making these products better suited for lineament interpretation in this setting. The longer wavelength utilized by this sensor make RADARSAT-1 uninhibited by atmospheric conditions and allows the sensor to collect imagery at any time in either an ascending or descending orbital path. Fusing ascending and descending scenes produces a composite image that has two illumination directions overcoming feature suppression in any direction. This can be seen in the product assessment provided in Table 4. The 12.5-m spatial resolution of RADARSAT-1 Standard Beam Mode images fall into the same level of detail as ASTER VNIR products, again providing the right level of detail for lineament interpretations. In addition, RADARSAT-1 products are dominated by topographic features and are influenced less by vegetation and anthropogenic targets. For this reason, lineament interpretations made from RADARSAT-1 products are more likely than optical image products to reflect subsurface structure.

RADARSAT-1 despeckle Levels 2 and 3 products performed the best because this processing technique removes noise (backscatter). The original RADARSAT-1 product was saturated with random backscatter pixels inherent to this sensor causing suppression of lineament features. When random backscatter is reduced, many of the lineament features become observable. It is important to note the differences between despeckle Levels 2 and 3. Level 3 exhibited *less* lineament features than Level 2, demonstrating that it is possible to over-despeckle a product and remove important features. Further despeckling beyond Level 3 would surely produce even fewer lineaments.

Production of a coincidence raster resulting from the GIS analysis method indicates that this method works well to synthesize several lineament interpretations by creating a single, clear coincidence raster and is shown in Figure 14. In the case of Boaco where very few structural features have been mapped, it is inappropriate to filter lineament interpretations based on the limited knowledge of faulting orientations. Moreover, due to extensive surface weathering, it is much more fitting to represent a lineament as a *zone* rather than a thin line. Creating the coincidence raster is a good alternative to traditional orientation-based lineament filters since the coincidence raster is based upon the *zonal* agreement of several interpretations and proves to correlate well with the few faults mapped in the study area, Figure 14.

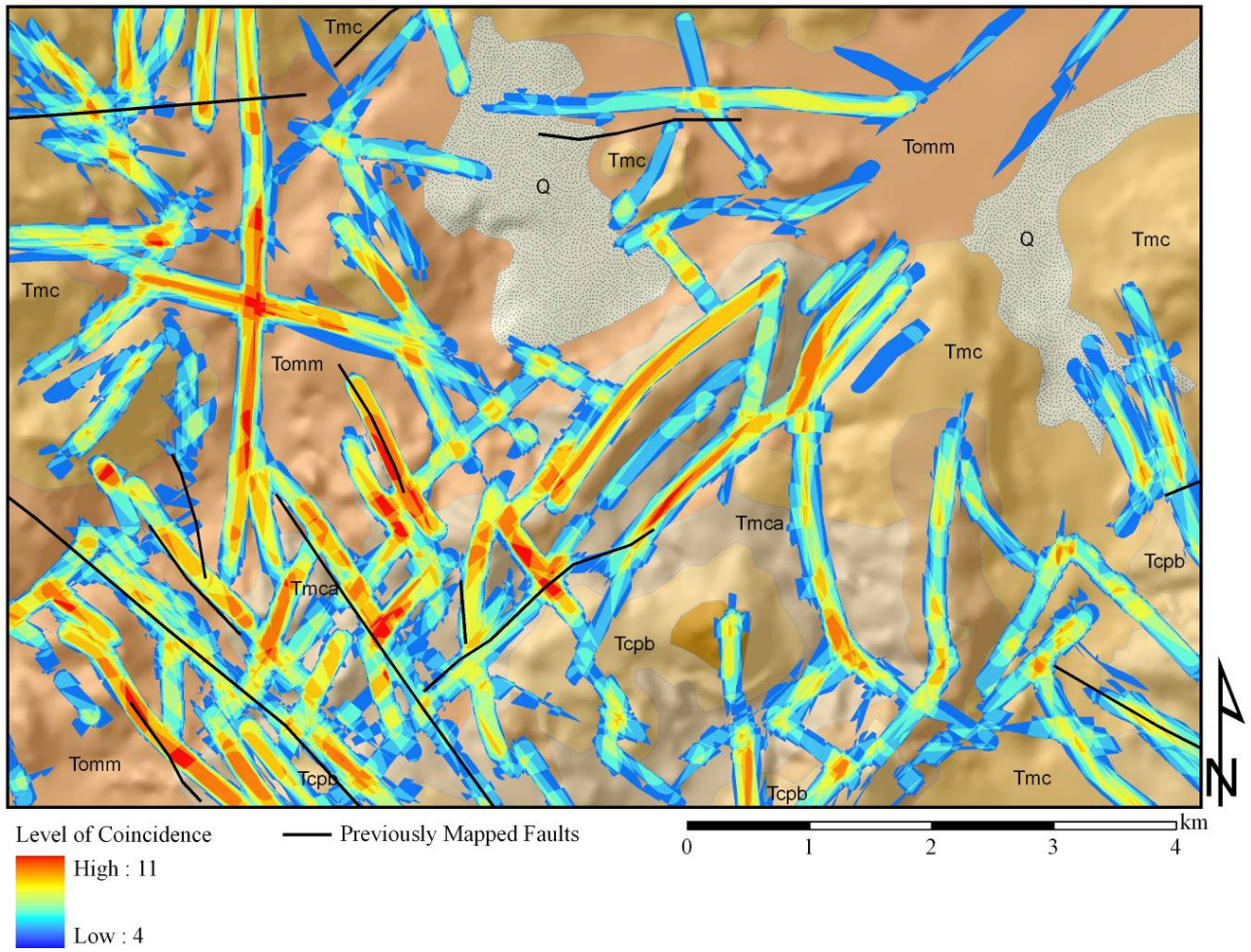

Figure 14: Coincidence raster. Geological Map adapted from Office of Cadasters and Natural Resources Inventory (1971). Topographic hillshade derived from INETER (1987). Level of lineament coincidence, or agreement, is shown gradationally with warmer shades indicating a higher level of agreement.

With a strict coincidence number of 4 used to make the coincidence raster (refer to Methods 3.5 and Appendix 6), fewer original interpreted lineaments made it through the filter than if the coincidence level had been set at 2 as recommended in the study by Mabee et al. (1994). The result is a much cleaner coincidence raster, see Appendix 4 for a comparison of the coincidence raster resulting from these two coincidence numbers. This indicates that having a strict coincidence level is suitable in this study due to the large number of input image products which tend to obscure the coincidence raster. It may be necessary to reduce or increase the coincidence level for other studies if less products and/or image types are used to create the coincidence raster.

Superior performance of RADARSAT-1 products is suspicious because 7 of the 11 image products used to create the coincidence raster are RADARSAT-1 products. To ensure these results are not an artifact of the coincidence raster composition, two more coincidence rasters were generated and qualitatively compared to the original coincidence raster. Additional coincidence rasters created include a RADARSAT-1 coincidence raster made with RADARSAT-1 products only (7 input products) and an ASTER coincidence raster made with ASTER products only (2 input products), and are provided in Figures 15 A and B. It can be seen in Figure 15 A and B that these two coincidence rasters have slightly differing geographic footprints. However when these coincidence rasters are compared with the original coincidence raster, provided in Figure 16, it is clear that neither RADARSAT-1 nor ASTER products alone explain the original coincidence raster entirely. There are several lineaments as shown in Figure 16 that only ASTER coincidence raster detect (e.g., lineaments labeled A and B) and several that only RADARSAT-1coincidence raster detect (e.g., lineaments labeled, C, D, and E). Furthermore, there are a handful of lineaments in the original coincidence raster that are not explained by either of the additional coincidence rasters, implying that coincidence in these cases must occur between products of different sensor types. Results from this comparison indicate that superior performance of RADARSAT-1 products is not an artifact of coincidence raster composition.

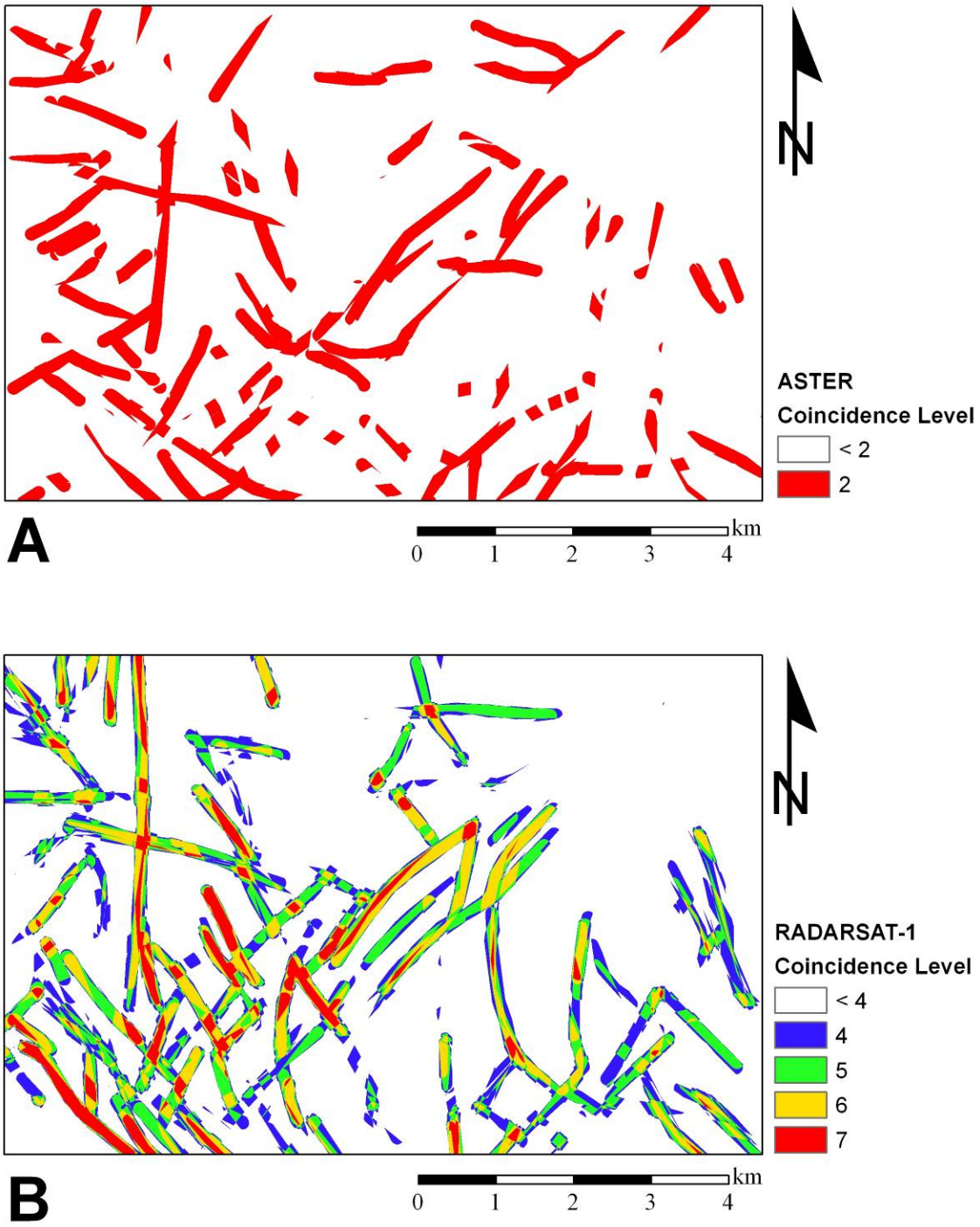

Figure 15 A and B: Additional coincidence rasters. Coincidence raster A is made with two ASTER product inputs and coincidence raster B is made with 7 RADARSAT-1 product inputs. The threshold of coincidence level 4 is used for the RADARSAT-1 coincidence raster, which is the same threshold for the original coincidence raster.

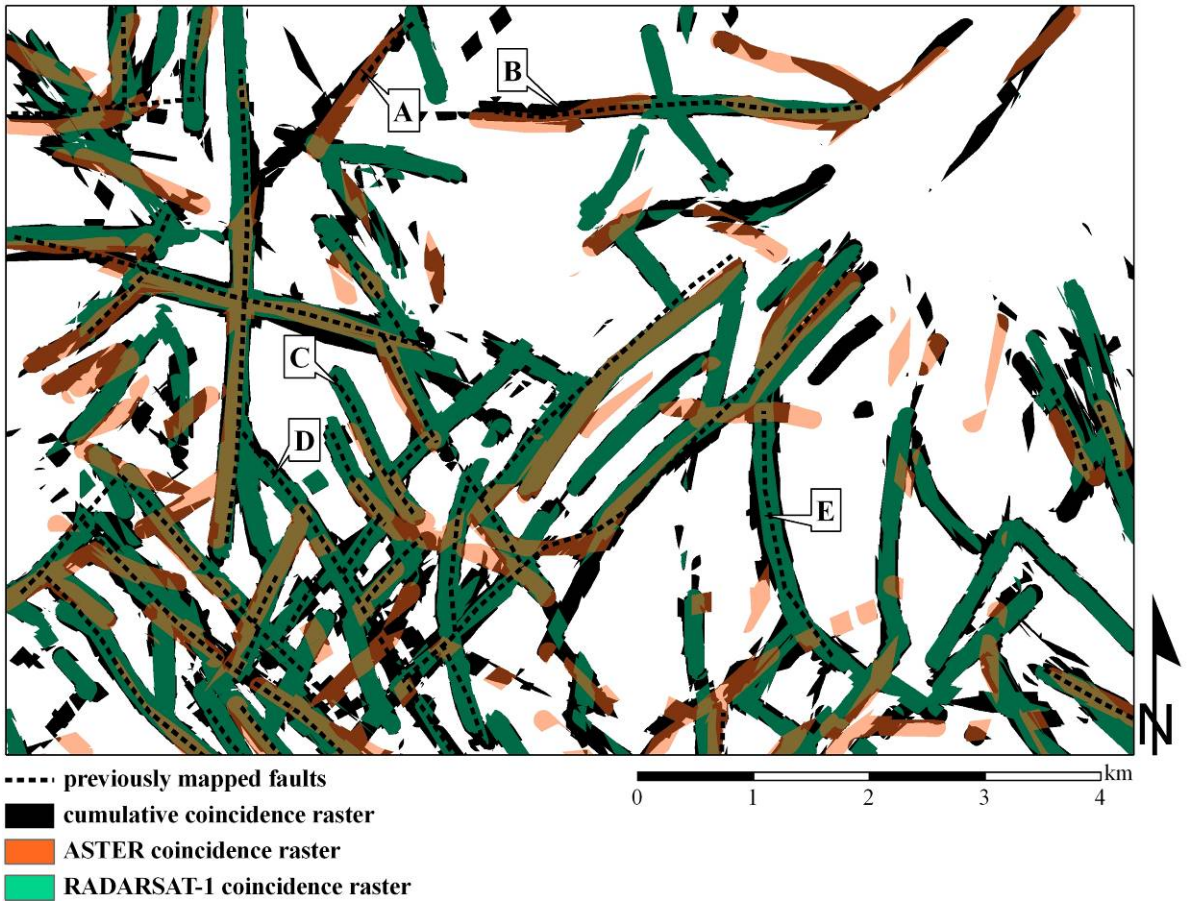

Figure 16: Comparison of the original coincidence raster to ASTER and RADARSAT-1 coincidence rasters. Neither RADARSAT-1 nor ASTER products alone explain the original coincidence raster entirely as there are several lineaments that only ASTER coincidence raster detect (e.g., lineaments labeled A and B) and several that only RADARSAT-1coincidence raster detect (e.g., lineaments labeled, C, D, and E). This indicates that superior performance of RADARSAT-1 products over the other imagery products is not an artifact of coincidence raster composition.

Utilizing both the coincidence raster and DEM allow for a final drawing of interpreted lineaments to be made with confidence, presented in Figures 17 and 18. All but two of previously mapped faults were discerned by interpretation of the coincidence raster and DEM. It can be seen in Figures 17 and 18 that there are slight dislocations between the mapped faults and interpreted lineaments. This may be due to inconsistencies in scale or mistakes within the geological map. The two mapped faults not observed using the coincidence raster and DEM do not appear as topographic expressions and still require ground confirmation. Lineaments interpreted where there are no mapped faults display the same attributes in the coincidence raster and DEM as locations where previously mapped faults are located.

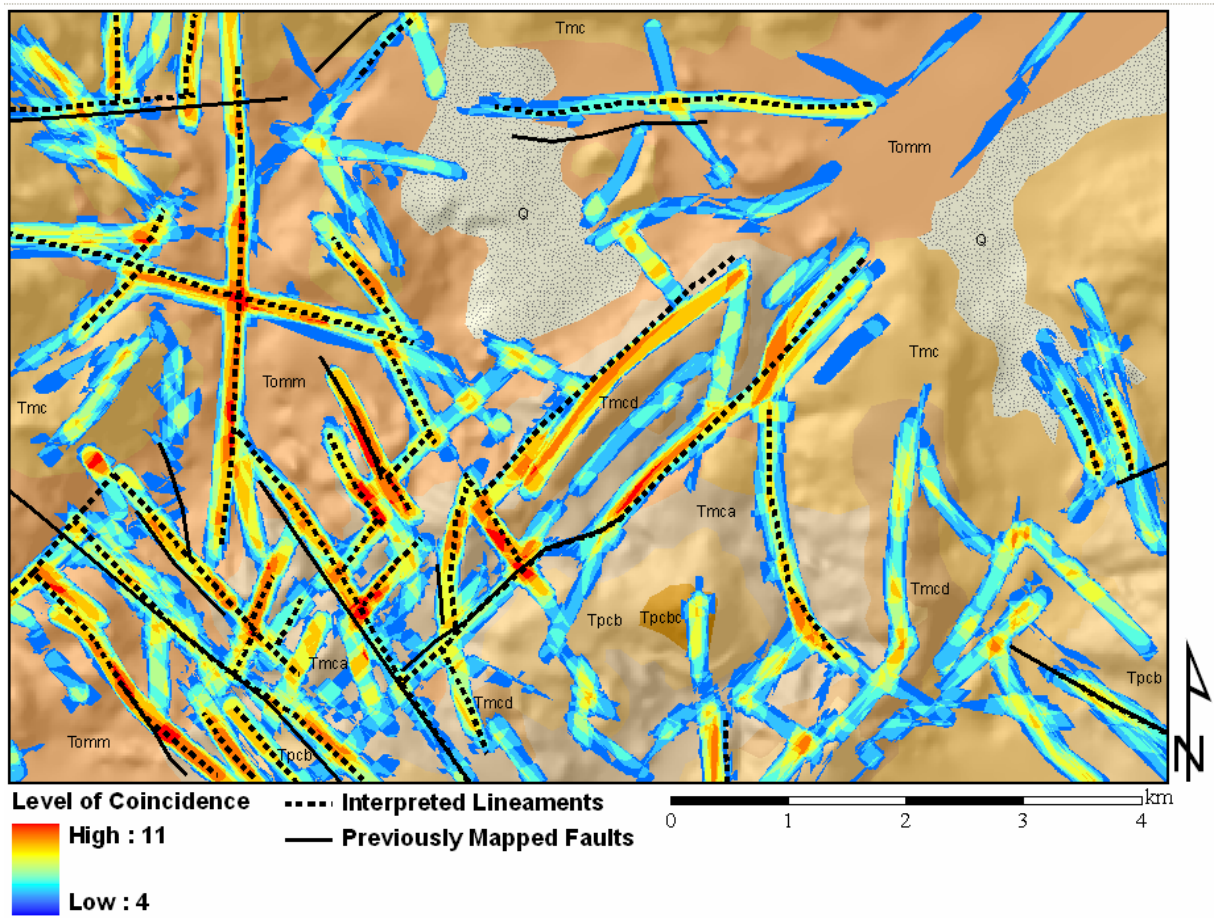

Figure 17: Interpreted lineaments determined from the coincidence raster and DEM. Geological Map adapted from Office of Cadasters and Natural Resources Inventory (1971). Topographic hillshade derived from INETER (1987). All but two of mapped faults were observed using the coincidence raster and DEM. It can be seen from this image that faulting has important control over topography. Level of lineament coincidence, or agreement, is shown gradationally with warmer shades indicating a higher level of agreement.

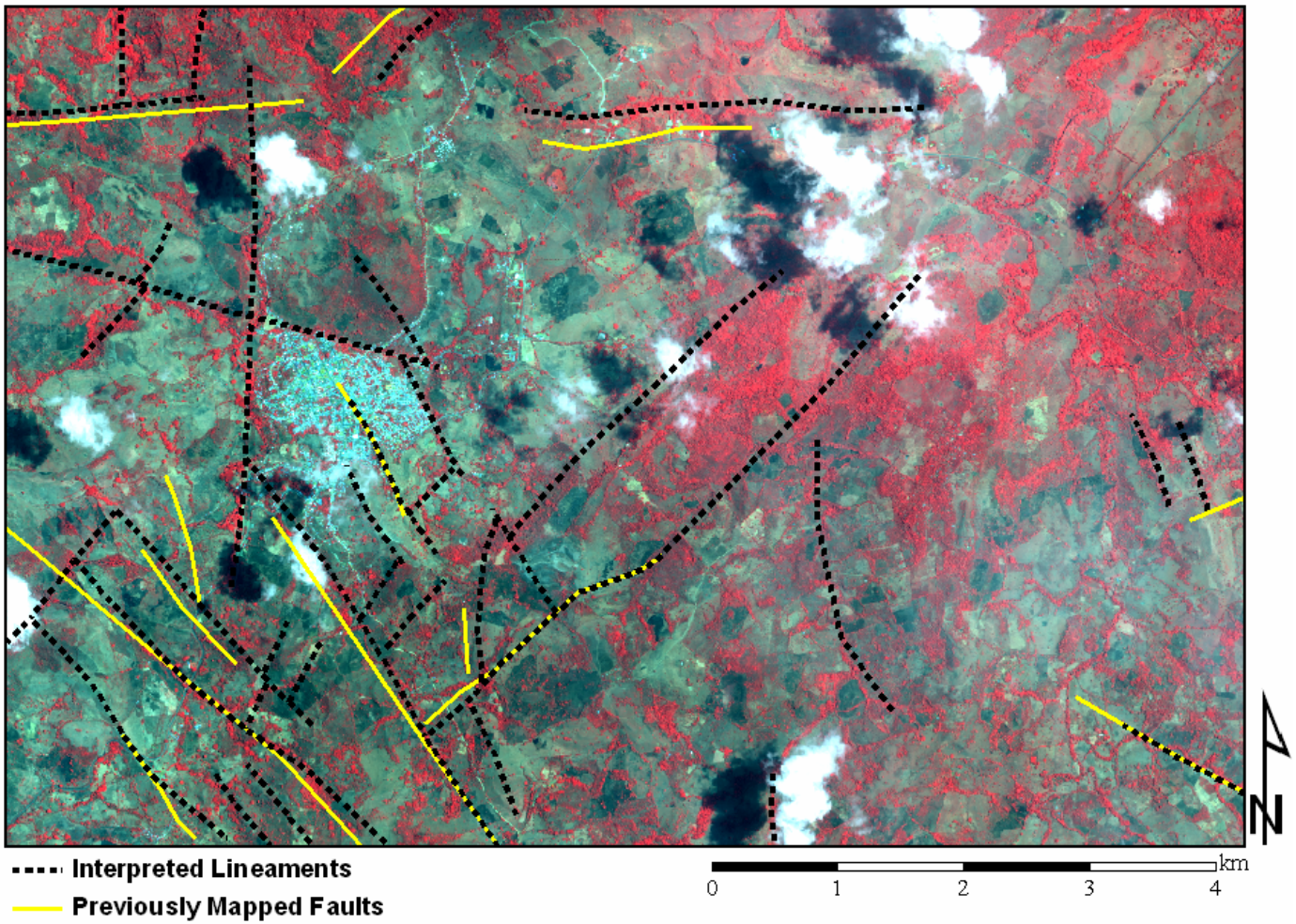

Figure 18: Interpreted faults overlain on the QuickBird image. Imagery derived from Digital Globe QuickBird (2006). The QuickBird image is displaying bands 4, 3, 1.

Ground based observations of lineament features are compared to remotely sensed interpreted lineaments and previously mapped faults in Figure 19. The figure show that of the 42 features observed in the field, 21 were interpreted using the coincidence raster and DEM. Disagreement between the two is most likely due to errors contained in both data sets. The study area lacks adequate outcrops dispersed across the area because of severe weathering; therefore ground truth relied purely on observation of geomorphic lineament features. These features include alignments of valley, drainages, and cliffs and their locations have definite error. For example, the position of a drainage observed from a ground vantage point does not *exactly* reflect the location and orientation of a possible underlying structural feature. This causes displacements and disorientations between remotely sensed and ground observed features. Furthermore, it is possible that some of the ground observed features are not true lineaments. Many of the linear drainages observed from the ground were minor and may not be caused by subsurface fracturing whereas the remotely sensed based observations are much more regional. For these reasons, 21 of 42 (or 50% of) lineaments being confirmed by ground truth is conservative and it is probable that the remotely sensed interpreted features correlate better with subsurface structure than these ground validations results indicate.

While producing high quality lineament interpretations requires anthropogenic features to be minimized, it is important to note that such features can provide some geological information and should not be ignored completely. In this region as well as in other developing countries, orientations of roads, field boundaries, property ownerships, municipality lines, etc tend to reflect orientations of regional fault patterns and structure trends. Land cover is not constrained by the grid system present in the developed world. This is demonstrated in Figure 20 which shows clear similarities between fault and field boundary orientations (digitized from the QuickBird image). Performing this simple operation in a location where geological structure is either unknown or poorly understood establishes an approximation of and boost confidence in structural knowledge.

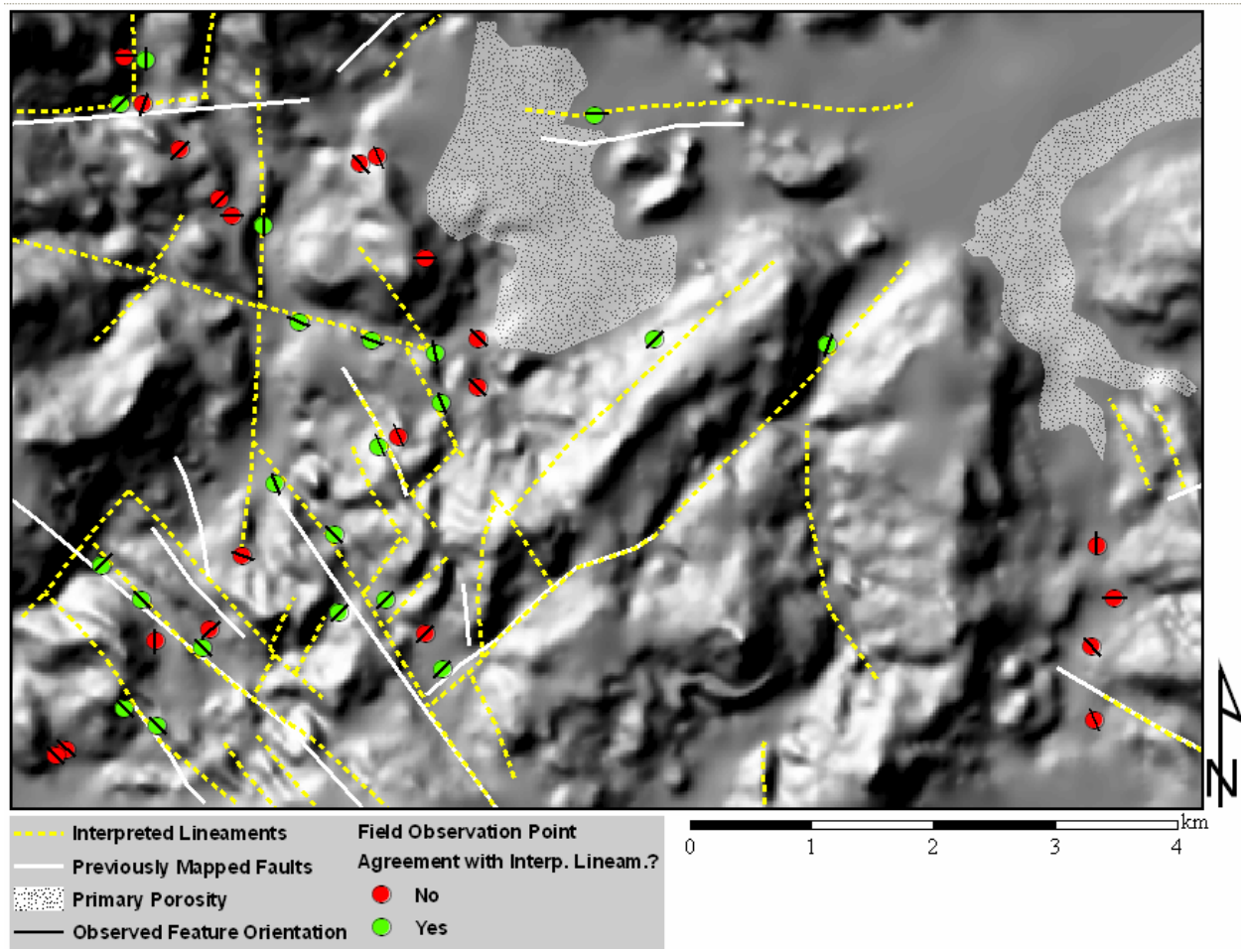

Figure 19: Interpreted lineaments and ground observed features. Topographic hillshade derived from INETER (1987). Interpreted lineaments (yellow dashed lines) and previously mapped faults (solid white lines) are compared with ground based observations. Locations where ground observations agree with interpreted lineaments are shown as green points and those that disagree are red. Of the 42 features observed in the field, 21 were interpreted using the coincidence raster and DEM.

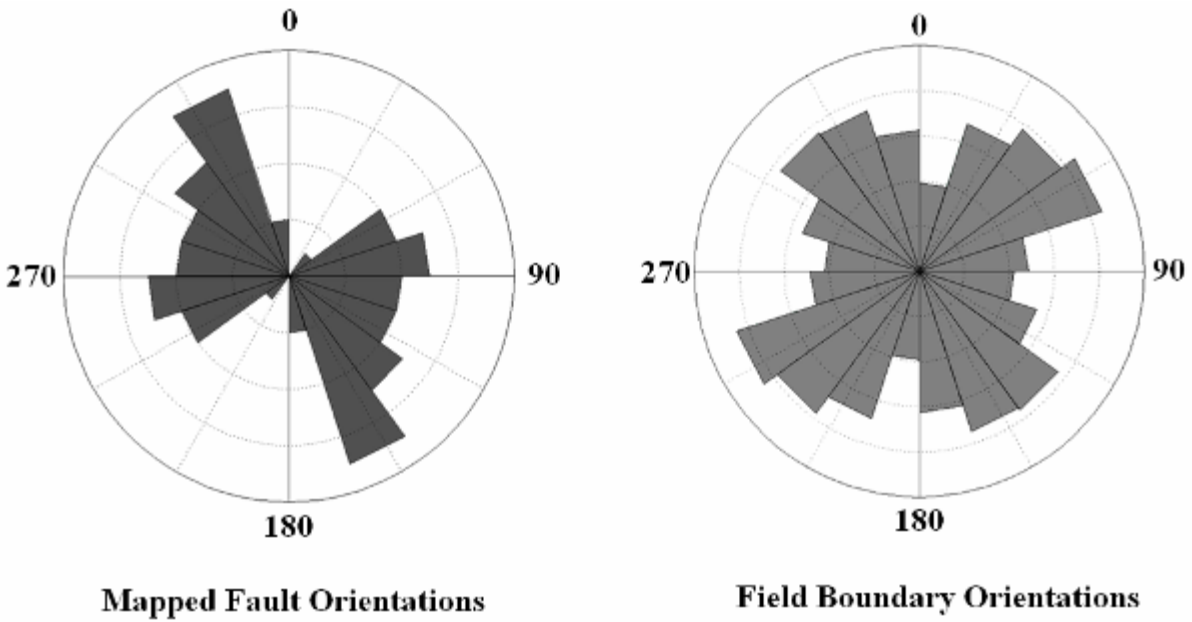

Figure 20: Comparison of mapped faults and field boundary orientations. The two dominate faulting directions are expressed to a degree by field boundaries orientations in Boaco, Nicaragua. This implies that land use is controlled by geological structure to some extent.

Although performance of QuickBird products to delineate lineaments was poor, the imagery's high-spatial resolution proved useful in other components of the study. As mentioned above, the field boundary orientations were examined using the QuickBird imagery. Fault-zone aperture measurements were made from the QuickBird imagery which is a key aspect of the GIS analysis methodology. Finally, other features are easily seen in the QuickBird imagery and allow for analysis of land cover and land use prior to deployment of a field campaign. The quality and detail of the measurements and observations discussed here would not have been possible using the other optical sensor types.

Results from the pumping tests are provided in Table 6 and shown in Figure 12. Of the nine wells tested, four were located in hard-rock aquifers while the other five were in alluvial aquifers. A positive correlation between well production and proximity to a lineament feature exists for the wells located in hard-rock aquifers. Two of these four wells, Paso de Laja and Ranch, had very low specific capacity values and are not shown to lie within a coincident area. The other two wells, Paso de Laja S and Municipal Slaughter House, have higher specific capacity values and lay within a coincident area. In fact, the municipal slaughter house well has the highest specific capacity of any of the hard-rock aquifer wells (1 gpm/ft) and is located on the most extensive fault in the study area. Although the number of wells tested is not enough to make a statistical assessment, results indicate that there may be a relationship between well productivity and lineament locations. A similar visual assessment of the five wells located in alluvial aquifers cannot be made. Thickness of these alluvial aquifers and depth of the wells are unknown; it is impossible to know if the wells are drawing from the alluvial aquifer alone or are reaching below to hard-rock aquifers. Specific capacity values of these wells vary significantly over small distances. For example, the two wells located in south San Nicolas, are 55-m apart and differ by over 5 gpm/ft in specific capacity. If both of these wells are drawing from an alluvial aquifer, these results indicate that alluvial aquifers are extremely heterogeneous in this area and well success must be determined from other methods than presented here.

5.0 Conclusions

Lineament mapping offers a low-cost, non-invasive approach for improving groundwater exploration in hard-rock terrains by identifying zones of secondary porosity in the form of fractures. However, in challenging, remote areas of the world, geological and hydrological information is often lacking and anthropogenic and climatic influences dominate land use and land cover making traditional methods of lineament mapping ineffective. The method developed here establishes an appropriate approach and identifies successful satellite imagery types for lineament analysis, resolving many deficiencies when employing traditional lineament analysis techniques in challenging settings. This work combines select elements from methods previously developed along with new techniques for a new approach to lineament mapping. The primary steps of this method are (1) data preparation including an assessment of fracture phenomenology and selection of imagery, (2) feature exploitation and detection via image processing, image fusion, and lineament interpretation of successful image products, and (3) evaluation of results by pumping tests, ground-based visual inspection of lineaments, and GIS analysis.

Four complimentary satellite remote sensors were utilized for lineament analysis in this study and include ASTER, Landsat7 ETM+, QuickBird, and RADARSAT-1. Lineament interpretations based on RADARSAT-1 products are superior to interpretations from other sensor products as evaluated by the GIS analysis. The most successful products are composites of three RADARSAT-1 scenes acquired 2/24/2007 (ascending orbit), 9/9/2006 (ascending orbit), and 11/8/1997 (descending orbit) after being processed to remove speckle. These results show that producing high quality lineament interpretations in this region requires anthropogenic features to be minimized and topographic expressions to be maximized. However, utilizing RADARSAT-1 imagery alone for lineament interpretations may result in missed lineaments as shown when comparing results to the coincidence raster and ground based inspection for lineaments. For this reason, it is suggested that image products

derived from both radar and optical sensors along with a DEM are employed to generate a coincidence raster from which a final lineament map can be drawn.

Creating the coincidence raster is a good alternative to traditional orientation-based lineament filters in this setting. The coincidence raster is based upon the zonal agreement of several interpretations, rather than relying on detailed structural information. The coincidence raster proved to correlate well with the few faults mapped in the study area. Additionally, results from pump tests, though few in number, suggest that as well productivity can be linked to proximity to lineament features as interpreted from the coincidence raster. These results indicate that the coincidence raster is a useful tool to reveal where to focus geophysical field campaigns for groundwater exploration in this type of terrain and setting.

6.0 Future Work and Recommendations

Based on this work, several auxiliary studies are suggested to further examine these results in the context of this study area's climate and geology. Such studies include:

- Examination of thermal imagery, namely a nighttime ASTER scene, for lineament detection. A comparison of these results should be made with the successful image types identified in this study. This requires a different study location other than Boaco where cloud-free nighttime ASTER imagery is available.

- Assessment of the new RADARSAT-2 generation of imagery (launched December 2007) as compared with RADARSAT-1 imagery for lineament detection. Are the RADARSAT-2 products superior over the RADARSAT-1 products for this purpose?

- Comparison of RADARSAT-1's Standard Beam Mode and Fine Beam Mode products for lineament detection. Is the improved spatial resolution of a Fine Beam Mode product superior over the Standard Beam Mode product? Again, this requires a different study location other than Boaco where Fine Beam Mode images are available.

- Investigate the study area with wide-spread geophysical surveys to either confirm or disprove the lineament analysis. Ideally this would be performed with an airborne geophysical survey, either magnetic or gravity, due to difficulties of performing ground-based geophysics in this type of terrain, climate, and anthropogenic barriers.

- Test many more wells to allow for statistical analysis of pump test data vs. lineament location, density, and intersection. Results from this study may

provide a better assessment of the fracture buffer width used to create the coincidence raster. Unfortunately in the Boaco study area, this requires many new wells to be drilled as there are not enough feasible wells for testing at this time. A solution to this is to expand the study area beyond the current boundaries to make use of existing wells outside the study area.

- Repeat this entire study for another location of similar climate and geology to test if RADARSAT-1 Despeckle Levels 2 and 3 image products are again ranked the highest, advancing RADARSAT-1 image products as the key to successful lineament interpretations. Furthermore, it would be interesting to repeat the study a completely different study area with contrasting geology (i.e., karst setting) and/or climate to determine which image product is most successful elsewhere.

It is strongly recommended that geophysics accompany any satellite based remote sensing results prior to implementation of a drilling program. Geophysical surveys provide subsurface information about fracture dip, width, and vertical extent which are not revealed during lineament interpretations from satellite imagery. This additional information is necessary to further confirm lineament interpretations and pin-point an appropriate well site.

7.0 References Cited

Abouma-Simba, S., Deroin, J. P. and Regnoult, J. M. 2003. Combination of SAR, Spot, and Geophysical Data for Geological Mapping: the Nyanga Basin (SW Gabon) Example." *IEEE*, pp. 3314-3316.

Akman, A. Ü. and Tüfekçi, K. 2004. Determination and characterisation of fault systems and geomorphological features by RS and GIS techniques in the WSW part of the Turkey. Proceedings of XX ISPRS Congress: Geo-Imagery Bridging Continents, Vol. XXXV, Istanbul, pp. 899–904.

Alaska Satellite Facility Distributed Active Archive Center Program and NASA (2007), RADARSAT-1 scene R159031031G1S002, Standard Beam Mode 3, ASF, Fairbanks, Alaska, February 24, 2007.

Alaska Satellite Facility Distributed Active Archive Center Program and NASA (2006), RADARSAT-1 scene R156630031G1S002, Standard Beam Mode 3, ASF, Fairbanks, Alaska, September 9, 2006.

Alaska Satellite Facility Distributed Active Archive Center Program and NASA (1997), RADARSAT-1 scene R110503419G1S001, Standard Beam Mode 3, ASF, Fairbanks, Alaska, November 8, 1997.

Arellano-Baeza, A. A., Zverev, A. T. and Malinnikov, V. A. 2006. Study of changes in the lineament structure, caused by earthquakes in South America by applying the lineament analysis to the Aster (Terra) satellite data. Advances in Space Research, Vol. 37, No. 4, pp. 690-697.

ASF MapReady© version 1.0.2, 2007. Alaska Satellite Facility, Geophysical Institute, University of Alaska Fairbanks, Fairbanks, AK.

Boeckh, E. 1992. An exploration strategy for higher-yield boreholes in the West African crystalline basement, *in* Hydrogeology of Crystalline Basement Aquifers in Africa. Geological Society Special Publication, No. 66, pp. 87-100. Wright, E. P. and Burgess W. G. (eds).

Breilin, O., Tikkanen, J., Kesola, R., Leveinen, J. and Mursu, J. 2003. Groundwater from crystalline bedrock in municipal of Leppävirta in southeast Finland. Groundwater in Fractured Rocks, Krásný-Hrkal-Bruthans (eds).

Bundschuh, J., Alvarado, G. E. (eds.). 2007. Central America; Geology, Resources, and Hazards, Volumes 1 & 2. Taylor and Francis, March 27, 2006, pp. 1436.

Burns, K. L. and Brown, G. H. 1978. The Human Perception of Geological Lineaments and Other Discrete Features in Remote Sensing Imagery: Signal Strengths, Noise Levels and Quality. Remote Sensing and the Environment 7, p163-177.

Carroll, E. A. 2006. A water quality assessment of the upper Rio Fonseca drainage basin, Boaco, Nicaragua. M. S. Thesis, University of New Mexico.

Cross, A. and Wadge, G. 1998. Geological Lineament Detection Using the Hough Transform. Proceeding of IGARSS, pp. 1779-1782, August.

DigitalGlobe (2006), QuickBird scene 005547368010_01_P001, Level Standard 2A, DigitalGlobe, Longmont, Colorado, 6/1/2006.

Drury, S. A. and Andrews Deller, M. E. 2002. Remote sensing and locating new water sources. Online only: http://www.unoosa.org/pdf/sap/2002/ethiopia/presentations/12speaker01_1.pdf. Cited 22 May 2008.

Edet, A. E., Okereke, C. S., Teme, S. C. and Esu, E.O. 1998. Application of remote-sensing data to groundwater exploration: a case study of the Cross River State, southeastern Nigeria. Hydrogeology Journal, Vol. 6, pp. 394–404.

Elaborado por el Instituto Nicaragüense de Estudios Territoriales (INETER). 1987. 1:50,000 Topographic Map, Region V, Department of Boaco.

ESRI© ArcMap™ 9.2, 2006.

Glenn, N. F. and Carr, J. R. 2004. The effects of soil moisture on synthetic aperture radar delineation of geomorphic surfaces in the Great Basin, Nevada, USA. Journal of Arid Environments, Vol. 56, No. 4, pp. 643-657.

Office of Cadasters and Natural Resources Inventory, 1971. Geological Map. Impreso por el Instituto Geográphico Nacional 1:50,000 Geological Map of Boaco, area 3053 II, series E751, Managua, Nicaragua.

Gross, E. L. 2008. A Manual Pumping Test Method for Characterizing the Productivity of Drilled Wells Equipped with Rope Pumps. M.S. Thesis, Department of Geological and Mining Engineering and Sciences, Michigan Technological University.

Gross, E. L. 2008. Interview, April 15, 2008, Houghton, Michigan, USA.

Gutierrez, L. M. 2008. Interview, March 19, 2008, Boaco, Nicaragua.

Gupta, R. P. 2003. Remote Sensing Geology, 2nd Edition. Springer, Berlin, p655.

Henderson, D. B., Ferrill, D. A. and Clarke, K. C. 1996. Mapping Geological Faults Using Image Processing Techniques Applied to Hill-Shaded Digital Elevation Models. *IEEE*, pp 240-245.

Hung, L. Q., Batelaan, O., and De Smedt, F. 2005. Lineament extraction and analysis, comparison of LANDSAT ETM and ASTER imagery. Case study:

Suoimuoi tropical karst catchment, Vietnam. Proceedings of SPIE, Vol. 5983.

Hung, L. Q., Batelaan, O., San, D. N. and De Smedt, F. 2004. Lineament analysis for the groundwater in karst fractured rocks in the suoimuoi karst catchment. Proceedings of the International Transdisciplinary Conference on Development and Conservation of Karst Regions, Hanoi, Vietnam. 13-18 September. Batelann, O., Dusar, M., Masschelein, J., Tam, V. T., Van, T. T. and Khien, N. X. (eds).

HydroSOLVE, Inc. 2007. AQTESOLV®. Developed by Duffield, G. M.

Jensen, J. R. 2005. Introductory Digital Image Processing: A Remote Sensing Perspective, 3rd Edition. Pearson Prentice Hall, Upper Saddle River, New Jersey.

Jha, M. K., Chowdhury, A. and Chowdary, V. M. 2007. Groundwater management and development by integrated remote sensing and geographic information systems: prospects and constraints. Water Resource Management, Vol. 21, pp. 427-467.

Inzana, J., Kusky, T., Higos, G., and Tucker, R. 2003. Supervised classifications of Landsat TM band ratio images and Landsat TM band ratio image with radar for geological interpretations of central Madagascar. Journal of African Earth Sciences, Vol. 37, No. 1-2, pp. 59-72, July-August.

Kageyama, Y., Nishida, M. and Oi, T. 2000. Analysis of the segments extracted by automated lineament detection. IEEE, Vol. 1, pp. 289-291.

Khan, S. D. and Glenn, N. F. 2006. New strike-slip faults and litho-units mapped in Chitral (n. Pakistan) using field and ASTER data yield regionally significant results. International Journal of Remote Sensing, Vol. 27, Nos. 18-20, pp. 4495-4512.

Kresic, N. 1995. Remote Sensing of Tectonic Fabric Controlling Goundwater Flow in Dinaric Karst. Remote Sensing of Environment, Vol. 53, No. 2, pp. 85-90, August.

Krishnamurthy, J., Manavalan, P. and Saivasan, V. 1992. Application of digital enhancement techniques for groundwater exploration in hard-rock terrains. International Journal of Remote Sensing, Vol. 13, No. 15, pp. 2925-2942.

Lecia Geosystems Geospatial Imaging, LLC. 2006. ERDAS IMAGINE 9.1.

Lee, T. H. and Moon, W. M. 2002. Lineament Extraction from Landsat TM, JERS-1 SAR, and DEM for Geological Applications. IEEE, pp. 3276-3278.

Loizzo, R., Sylos Labini, G., Pappalepore, M., Pieri, P., Blonda, P., Pasquariello, G. and Antoninette, M. 1994. Multitemporal Analysis of ERS-1 and Landsat TM data for Geological Studies. IEEE, pp. 1478-1780.

Loveless, J. P., Hoke, G. D., Allmendinger, R. W., González, G., Isacks, B. L., Carrizo, D. A. 2005. Pervasive cracking of the northern Chilean Coastal Cordillera: New evidence for forearc extension. Geology, Vol. 33, No. 12, pp. 973-976.

Mabee, S. D. 1999. Factors Influencing Well Productivity in Glaciated Metamorphic Rocks. Ground Water, Vol. 37, No. 1, pp. 88-97.

Mabee, S. B., Hardcastle, K. C. and Wise, D. U. 1994. A Method of Collecting and Analyzing Lineaments for Regional-Scale Fractured –Bedrock Aquifer Studies. Ground Water, Vol. 32, No. 6, pp. 884-894.

Mahmood, A. 1996. Lineaments as groundwater exploration guides in hard-rock terranes of arid regions. Canadian Journal of Remote Sensing, Vol. 22, No. 1., pp.108-116.

Magowe, M. and Carr, J. R. 1999. Relationship Between Lineaments and Ground Water Occurrence in Western Botswana. Ground Water, Vol. 37, No. 2, pp. 282-286.

Meijerink, A. M. J., Bannert, D., Batelaan, O., Lubczynski, M. W. and Pointet, T. 2007. Remote Sensing Applications to Groundwater. IHP-VI, Series on Groundwater No. 16, United Nations Educational, Scientific and Cultural Organization, Paris, France, pp. 304.

Murphy, M. A. and Burgess, W. P. 2006. Geometry, kinematics, and landscape characteristics of an active transtension zone, Karakoram fault system, Southwest, Tibet. Journal of Structural Geology, Vol. 28, No. 2, pp. 268-283.

NASA Landsat Program (2004), Landsat ETM+ scene L7CPF20011001_20011231_05, L1G, USGS, Sioux Falls, November 13, 2001.

Paganelli, F., Grunsky, E. C., Richards, J. P. and Pryde, R. 2003. Use of RADARSAT-1 principal component imagery for structural mapping: a case study in the Buffalo Head Hills area, northern central Alberta, Canada. Canadian Journal of Remote Sensing, Vol. 29, No. 1, pp. 111-140.

Paillou, P. and Rosenqvist, A. 2003. A JERS-1 radar mosaic for subsurface geology mapping in East Sahara. IEEE, Vol. 3, pp. 1870-1872, July.

Paradella, W. R., dos Santos, A. R., Dall' Agnol, R., Pietsch, R. W. and Sant' Anna, M. V. 1998. A Geological Investigation Based on Airborne (SAREX) and Spaceborne (RADARSAT-1) SAR Integrated Products in the

Central Serra Carajá Granite Area, Brazil. Canadian Journal of Remote Sensing, Vol. 24, No. 4, pp. 376-392.

Park, Y., Lee, K. and Kim, J. 2000. Effects of Highly Permeable Geological Discontinuities upon Groundwater Productivity and Well Yield. Mathematical Geology, Vol. 32, No. 5, pp. 605-615.

Radarsat International 1996. Radarsat Geology Handbook. Vancouver, British Columbia, Canada, pp. 56.

Raju, N. J. and Reddy, T. V. K. 1998. Fracture pattern and electrical resistivity studies for groundwater exploration. Environmental Geology, Vol. 34, pp. 175-182.

Ricchetti, E. 2002. Strucural Geological Study of Southern Apennine (Italy) Using Landsat 7 Imagery. IEEE, pp. 211-213.

Ricchetti, E. and Palombella, M. 2005. Application of Landsat 7 ETM+ Imagery for Geological Lineament Analysis of Southern Italy. IEEE, pp. 5200-5203.

Robinson, C., El-Baz, F. and Singhroy, V. H. 1999. Subsurface Imaging by RADARSAT: Comparison with Landsat TM Data and Implications for Ground Water in the Selima Area, Northwest Sudan. Canadian Journal of Remote Sensing, Vol. 25, No. 3, pp. 268-277.

Rogers, R. D. 2003. Jurassic-Recent tectonic and stratigraphic history of the Chortis block of Honduras and Nicaragua (northern Central America). The University of Texas at Austin, Ph. D. dissertation, pp. 289.

Rose, W. and Bluth, G. 2005. National Science Foundation Grant Proposal.

Sander, P. 2007. Lineaments in groundwater exploration: a review of applications and limitiations. Hydrogeology Journal, Vol. 15, pp. 71-74.

Sander, P., Minor, T. B. and Chesley, M. M. 1997. Ground-water exploration based on lineament analysis and reproducibility tests. Ground Water, Vol. 35, No. 5, pp. 888.

Saether, B., Rueslatten, H. and Gronlie, A. 1994. Application of the Hough transform for automated interpretation of linear features in imageries. IEEE, Vol. 2, pp. 847-850.

Sawaragi, T., Katsunobu, H., Katai, O. Sosuke, I. and Tsukada, K. 1992. Integrated Cognitice Architecture for Image Understanding Using Fuzzy Clustering and Structured Neural Network. IEEE, pp. 21-28.

Sawaya, K. E., Olmanson, L. G., Heinert, N. J., Brezonik, P. L. and Bauer, M. E. 2003. Extending satellite remote sensing to local scales: land and water resource monitoring using high-resolution imagery. Remote Sensing of Environment, Vol. 88, pp. 144-156.

Schaber, G. G., McCauley, J. F. and Breed, C.S. 1997, The use of multifrequency and polarimetric SIR-C/X-SAR data in geologic studies of Bir Safsaf, Egypt. Remote Sensing of Environment, Vol. 59, No. 2, pp. 337-363.

Solomon, S. and Friedrich, Q. 2006. Groundwater study using remote sensing and geographic information systems (GIS) in the central highlands of Eritrea. Hydrogeology Journal, Vol. 14, pp. 729-741.

Tam, V. T., De Smedt, F., Batelaan, O. and Dassargues, A. 2004. Study on the relationship between lineaments and borehole specific capacity in a fractured and karstified limestone area in Vietnam. Hydrogeology Journal, Vol. 12, pp. 662-673.

The MathWorks, Inc. 2007. MATLAB®, Version 7.4.0.287 (R2007a).

USGS (2004), Shuttle Radar Topography Mission, 3 Arc Second scene SRTM_fB03_p016r051, Unfilled Unfinished 2.0, Global Land Cover Facility, University of Maryland, College Park, Maryland, 2000.

USGS (2004), Shuttle Radar Topography Mission, 3 Arc Second scene SRTM_fB03_p016r052, Unfilled Unfinished 2.0, Global Land Cover Facility, University of Maryland, College Park, Maryland, 2000.

USGS (2004), Shuttle Radar Topography Mission, 3 Arc Second scene SRTM_fB03_p017r051, Unfilled Unfinished 2.0, Global Land Cover Facility, University of Maryland, College Park, Maryland, 2000.

USGS (2004), Shuttle Radar Topography Mission, 3 Arc Second scene SRTM_fB03_p017r052, Unfilled Unfinished 2.0, Global Land Cover Facility, University of Maryland, College Park, Maryland, 2000.

USGS and Japan ASTER Program (2007), ASTER scene AST_L1B_00311242005161636_20070712094142_26205, Level 1 B, USGS, Sioux Falls, November 11, 2004.

Vassilas, N., Perantonis, S., Eleni, C. Tsenoglou, T., Stefouli, M. and Varoufakis, S. 2002. Delineation of Lineaments from Satellite Data Based on Efficient Neural Network and Pattern Recognition Techniques. 2nd Hellenic Conf. on Al, SETN-2002 Proceedings, pp. 355-366, April.

Wang, J. and Howarth, P. J. 1990. Use of the Hough Transform in Automated Lineament Detection." IEEE, Vol. 28, No. 4, July.

Weyl, R. 1980. Geology of Central America, 2nd Edition. Borntraeger, Berlin, 371 pp.

Yun, S. and Moon, W. M. 2001. Lineament Extraction from DEM using Drainage Network. *IEEE*, pp. 2337-2339.

Appendix 1

General statistics, statistical assessments, and PCA results for all images.

Table A1-1: General statistics for all images. All units are brightness values.

QuickBird						
band	**min**	**max**	**mean**	**median**	**mode**	**std. dev.**
1	55	1106	303.65	269.59	290	53.58
2	38	1611	433.50	423.54	413	85.63
3	1	1217	287.59	279.97	293	72.32
4	1	1690	586.97	574.44	552	122.21

Lansat7 ETM+						
band*	**min**	**max**	**mean**	**median**	**mode**	**std. dev.**
1	47	149	65.58	65.00	64	5.34
2	33	140	54.10	54.00	54	6.38
3	18	186	41.86	40.00	38	9.37
4	21	159	93.34	94.00	93	14.69
5	6	192	86.95	87.00	84	17.44
7	10	139	41.31	40.00	36	10.74

*Band 6 (thermal) not considered in study.

ASTER						
band	**min**	**max**	**mean**	**median**	**mode**	**std. dev.**
1	34	169	46.90	46.56	47	4.87
2	16	176	24.99	24.21	21	4.75
3	45	210	91.00	90.82	88	10.89
4	7	24	11.14	11.10	11	1.12
5	1	7	2.04	2.00	2	0.23
6	1	8	1.87	1.82	2	0.26
7	1	7	1.53	1.50	1	0.21
8	1	5	0.95	0.91	1	0.15
9	0	3	0.62	0.61	1	0.06

RADARSAT-1						
band**	**min**	**max**	**mean**	**median**	**mode**	**std. dev.**
1	2	255	136.71	127.51	254	54.17
2	14.729	255	70.99	66.35	64	23.00
3	15.41	255	74.79	69.69	64	25.00

**Bands 1, 2, and 3 are scenes acquired on 2/24/2007, 11/8/1997, and 9/92006 respectively.

Table A1-2: QuickBird statistical assessment.

Correlation matrix

band	1	2	3	4
1	1.000	0.994	0.967	0.474
2	0.994	1.000	0.969	0.538
3	0.967	0.969	1.000	0.391
4	0.474	0.538	0.391	1.000

Variance-covariance matrix

band	1	2	3	4
1	2871.180	4559.397	3752.208	3104.479
2	4559.397	7331.738	6008.178	5631.331
3	3752.208	6008.178	5240.389	3455.719
4	3104.479	5631.331	3455.719	14935.102

Optimum index factor (OIF)

Band Combination	Optimum Index Factor
1, 2, 3	107.9
1, 2, 4	169.1
1, 3, 4	172.2
2, 3, 4	301.7

Table A1-2: QuickBird statistical assessment – continued.

Principal components analysis (PCA)

	Principal Component			
	1	**2**	**3**	**4**
Eigen values	22330.4	7897.0	140.9	10.1
Difference	14433.4	7756.1	130.8	---
Total Variance	30378.4			

Percentage	73.5	26.0	0.5	0.0
Cumulative	73.5	99.5	100.0	100.0

Eigenvectors (factor scores)

	Principal Component			
	1	**2**	**3**	**4**
band 1	0.307	-0.304	-0.485	0.761
2	0.513	-0.427	-0.397	-0.630
3	0.389	-0.473	0.776	0.148
4	0.701	0.708	0.072	0.045

Factor Loadings

	Principal Component			
	1	**2**	**3**	**4**
band 1	0.856	-0.503	-0.107	0.045
2	0.894	-0.443	-0.055	-0.023
3	0.804	-0.581	0.127	0.007
4	0.857	0.515	0.007	0.001

Table A1-3: Landsat7 ETM+ statistical assessment.

Correlation matrix

band*	1	2	3	4	5	7
1	1.000	0.988	0.988	0.470	0.782	0.921
2	0.988	1.000	0.990	0.541	0.836	0.942
3	0.988	0.990	1.000	0.465	0.834	0.953
4	0.470	0.541	0.465	1.000	0.669	0.527
5	0.782	0.836	0.834	0.669	1.000	0.935
7	0.921	0.942	0.953	0.527	0.935	1.000

*Band 6 (thermal) not considered in study.

Variance-covariance matrix

band*	1	2	3	4	5	7
1	1034.598	993.198	1146.074	320.068	739.747	746.614
2	993.198	976.333	1115.060	357.893	768.715	742.184
3	1146.074	1115.060	1299.988	355.244	884.262	865.951
4	320.068	357.893	355.244	448.761	416.677	281.228
5	739.747	768.715	884.262	416.677	865.330	693.347
7	746.614	742.184	865.951	281.228	693.347	635.412

*Band 6 (thermal) not considered in study.

Table A1-3: Landsat7 ETM+ statistical assessment – continued.

Optimum index factor (OIF)

Band Combination	Optimum Index Factor
1, 2, 3	10.7
1, 2, 4	18.1
1, 2, 5	16.5
1, 2, 7	11.8
1, 3, 4	20.2
1, 3, 5	18.2
1, 3, 7	13.3
1, 4, 5	29.9
1, 4, 7	22.1
1, 5, 7	19.7
2, 3, 4	19.9
2, 3, 5	18.2
2, 3, 7	13.7
2, 4, 5	28.0
2, 4, 7	21.5
2, 5, 7	19.4
3, 4, 5	31.9
3, 4, 7	24.5
3, 5, 7	21.0
4, 5, 7	35.9

*Band 6 (thermal) not considered in study.

Table A1-3: Landsat7 ETM+ statistical assessment – continued.

Principal components analysis (PCA)

	Principal Component					
	1	**2**	**3**	**4**	**5**	**7**
Eigen values	507.3	229.4	42.4	5.56	4.32	3.29
Difference	277.9	187.0	36.8	1.25	1.03	---
Total Variance	792.2					
Percentage	64.0	29.0	5.4	0.7	0.5	0.4
Cumulative	64.0	93.0	98.3	99.0	99.6	100.0

Eigenvectors (factor scores)

	Principal Component					
	1	**2**	**3**	**4**	**5**	**7**
band 1	0.152	-0.167	-0.420	0.235	0.494	-0.688
2	0.237	-0.085	-0.424	-0.191	0.540	0.654
3	0.321	-0.306	-0.525	-0.381	-0.610	-0.103
4	0.219	0.903	-0.323	0.122	-0.132	-0.027
5	0.758	0.063	0.513	-0.329	0.157	-0.160
7	0.442	-0.229	0.032	0.800	-0.222	0.248

Factor Loadings

	Principal Component					
	1	**2**	**3**	**4**	**5**	**7**
band 1	0.107	-0.079	-0.085	0.017	0.032	-0.039
2	0.171	-0.041	-0.088	-0.014	0.036	0.038
3	0.200	-0.128	-0.095	-0.025	-0.035	-0.005
4	0.232	0.645	-0.099	0.014	-0.013	-0.002
5	0.580	0.032	0.114	-0.026	0.011	-0.010
7	0.395	-0.137	0.008	0.075	-0.018	0.018

Table A1-4: ASTER statistical assessment.

Correlation matrix

band	1	2	3	4	5	6	7	8	9
1	1.000	0.940	-0.059	0.570	0.787	0.777	0.793	0.799	0.771
2	0.940	1.000	-0.295	0.501	0.816	0.803	0.820	0.843	0.834
3	-0.059	-0.295	1.000	0.289	-0.117	-0.092	-0.116	-0.179	-0.250
4	0.570	0.501	0.289	1.000	0.812	0.835	0.798	0.735	0.632
5	0.787	0.816	-0.117	0.812	1.000	0.979	0.973	0.967	0.914
6	0.777	0.803	-0.092	0.835	0.979	1.000	0.975	0.967	0.915
7	0.793	0.820	-0.116	0.798	0.973	0.975	1.000	0.970	0.922
8	0.799	0.843	-0.179	0.735	0.967	0.967	0.970	1.000	0.945
9	0.771	0.834	-0.250	0.632	0.914	0.915	0.922	0.945	1.000

Variance-covariance matrix

band	1	2	3	4	5	6	7	8	9
1	40.447	29.388	38.621	7.832	1.696	1.712	1.423	0.938	0.494
2	29.388	25.273	9.194	5.142	1.293	1.346	1.124	0.765	0.382
3	38.621	9.194	177.054	12.963	1.534	1.411	1.107	0.578	0.386
4	7.832	5.142	12.963	2.444	0.422	0.438	0.352	0.221	0.111
5	1.696	1.293	1.534	0.422	0.090	0.092	0.076	0.050	0.025
6	1.712	1.346	1.411	0.438	0.092	0.098	0.080	0.053	0.026
7	1.423	1.124	1.107	0.352	0.076	0.080	0.067	0.044	0.021
8	0.938	0.765	0.578	0.221	0.050	0.053	0.044	0.030	0.014
9	0.494	0.382	0.386	0.111	0.025	0.026	0.021	0.014	0.008

Table A1-4: ASTER statistical assessment – continued.

Optimum index factor (OIF)

Band Combination	Optimum Index Factor	Band Combination	Optimum Index Factor	Band Combination	Optimum Index Factor
1, 2, 3	28.0	2, 3, 4	96.5	3, 5, 8	-46.5
1, 2, 4	8.6	2, 3, 5	35.7	3, 5, 9	-37.3
1, 2, 5	6.8	2, 3, 6	36.7	3, 6, 7	-66.8
1, 2, 6	6.8	2, 3, 7	35.4	3, 6, 8	-50.9
1, 2, 7	6.7	2, 3, 8	33.8	3, 6, 9	-40.1
1, 2, 8	6.6	2, 3, 9	34.2	3, 7, 8	-46.6
1, 2, 9	6.7	2, 4, 5	5.2	3, 7, 9	-37.4
1, 3, 4	41.6	2, 4, 6	5.3	3, 8, 9	-31.7
1, 3, 5	27.4	2, 4, 7	5.2	4, 5, 6	1.3
1, 3, 6	27.8	2, 4, 8	5.0	4, 5, 7	1.3
1, 3, 7	27.2	2, 4, 9	5.0	4, 5, 8	1.3
1, 3, 8	26.8	2, 5, 6	3.5	4, 5, 9	1.4
1, 3, 9	27.8	2, 5, 7	3.4	4, 6, 7	1.3
1, 4, 5	6.1	2, 5, 8	3.3	4, 6, 8	1.3
1, 4, 6	6.1	2, 5, 9	3.3	4, 6, 9	1.3
1, 4, 7	6.0	2, 6, 7	3.5	4, 7, 8	1.3
1, 4, 8	5.9	2, 6, 8	3.3	4, 7, 9	1.3
1, 4, 9	6.0	2, 6, 9	3.3	4, 8, 9	1.3
1, 5, 6	4.5	2, 7, 8	3.3	5, 6, 7	0.4
1, 5, 7	4.4	2, 7, 9	3.2	5, 6, 8	0.4
1, 5, 8	4.3	2, 8, 9	3.2	5, 6, 9	0.4
1, 5, 9	4.3	3, 4, 5	88.5	5, 7, 8	0.4
1, 6, 7	4.4	3, 4, 6	77.2	5, 7, 9	0.3
1, 6, 8	4.3	3, 4, 7	87.5	5, 8, 9	0.3
1, 6, 9	4.4	3, 4, 8	137.0	6, 7, 8	0.4
1, 7, 8	4.3	3, 4, 9	381.9	6, 7, 9	0.3
1, 7, 9	4.3	3, 5, 6	-66.5	6, 8, 9	0.3
1, 8, 9	4.2	3, 5, 7	-59.4	7, 8, 9	0.3

Table A1-4: ASTER statistical assessment – continued.

Principal components analysis (PCA)

	Principal Component								
	1	**2**	**3**	**4**	**5**	**6**	**7**	8	9
Eigen values	100.6	36.4	0.781	0.549	0.015	0.001	0.001	0.001	0.000
Difference	64.2	35.6	0.232	0.534	0.014	0.000	0.001	0.000	---
Total Variance	138.4								

Percentage	72.70	26.32	0.56	0.40	0.01	0.00	0.00	0.00	0.00
Cumulative	72.70	99.03	99.59	99.99	100.00	100.00	100.00	100.00	100.00

Eigenvectors (factor scores)

	Principal Component								
	1	**2**	**3**	**4**	**5**	**6**	**7**	8	9
band 1	0.069	-0.715	-0.425	0.551	0.010	-0.002	-0.003	0.000	0.000
2	0.171	-0.667	0.288	-0.664	-0.053	0.002	0.002	0.000	-0.001
3	-0.983	-0.164	0.001	-0.089	0.006	0.000	0.000	0.000	0.000
4	-0.025	-0.120	0.829	0.492	-0.234	0.017	0.011	0.034	0.012
5	0.004	-0.030	0.118	0.043	0.482	-0.670	0.534	-0.125	0.023
6	0.004	-0.034	0.142	0.051	0.531	-0.127	-0.751	-0.331	-0.071
7	0.004	-0.028	0.105	0.039	0.494	0.726	0.374	-0.273	-0.029
8	0.004	-0.019	0.065	0.018	0.386	0.068	-0.067	0.852	-0.333
9	0.002	-0.008	0.024	0.003	0.184	0.053	-0.083	0.271	0.939

Table A1-4: ASTER statistical assessment – continued.

Principal components analysis (PCA) - continued

Factor Loadings

	Principal Component								
	1	**2**	**3**	**4**	**5**	**6**	**7**	8	9
band 1	0.157	-0.980	-0.085	0.093	0.000	0.000	0.000	0.000	0.000
2	0.389	-0.913	0.058	-0.112	-0.001	0.000	0.000	0.000	0.000
3	-0.995	-0.100	0.000	-0.007	0.000	0.000	0.000	0.000	0.000
4	-0.228	-0.645	0.653	0.325	-0.026	0.001	0.000	0.001	0.000
5	0.197	-0.799	0.464	0.143	0.264	-0.106	0.082	-0.014	0.002
6	0.171	-0.794	0.491	0.149	0.255	-0.018	-0.101	-0.032	-0.005
7	0.196	-0.804	0.441	0.136	0.288	0.122	0.061	-0.032	-0.002
8	0.259	-0.800	0.394	0.091	0.326	0.016	-0.016	0.145	-0.041
9	0.327	-0.759	0.327	0.037	0.354	0.030	-0.045	0.105	0.263

Table A1-5: RADARSAT-1 statistical assessment.

Correlation matrix

band**	1	2	3
1	1.000	-0.159	0.596
2	-0.159	1.000	-0.199
3	0.596	-0.199	1.000

**Bands 1, 2, and 3 are scenes acquired on 2/24/2007, 11/8/1997, and 9/92006 respectively.

Variance-covariance matrix

band**	1	2	3
1	2934.845	-197.747	807.022
2	-197.747	528.746	-114.423
3	807.022	-114.423	624.991

**Bands 1, 2, and 3 are scenes acquired on 2/24/2007, 11/8/1997, and 9/92006 respectively.

Principal components analysis

	Principal Components		
	1	**2**	**3**
Eigen values	3207.5	526.0	355.1
Difference	2681.4	171.0	---
Total Variance	4088.6		

Percentage	78.45	12.87	8.69
Cumulative	78.45	91.31	100.00

Eigenvectors (factor scores)

	Principal Components		
	1	**2**	**3**
band 1	0.950	-0.083	0.301
2	-0.167	-0.949	0.267
3	-0.263	0.304	0.916

Factor Loadings

	Principal Components		
	1	**2**	**3**
band 1	0.993	-0.035	0.105
2	-0.412	-0.947	0.219
3	-0.596	0.279	0.690

Appendix 2

Examples of image ability to exhibit the two primary fault directions (ranked as good, moderate, or poor).

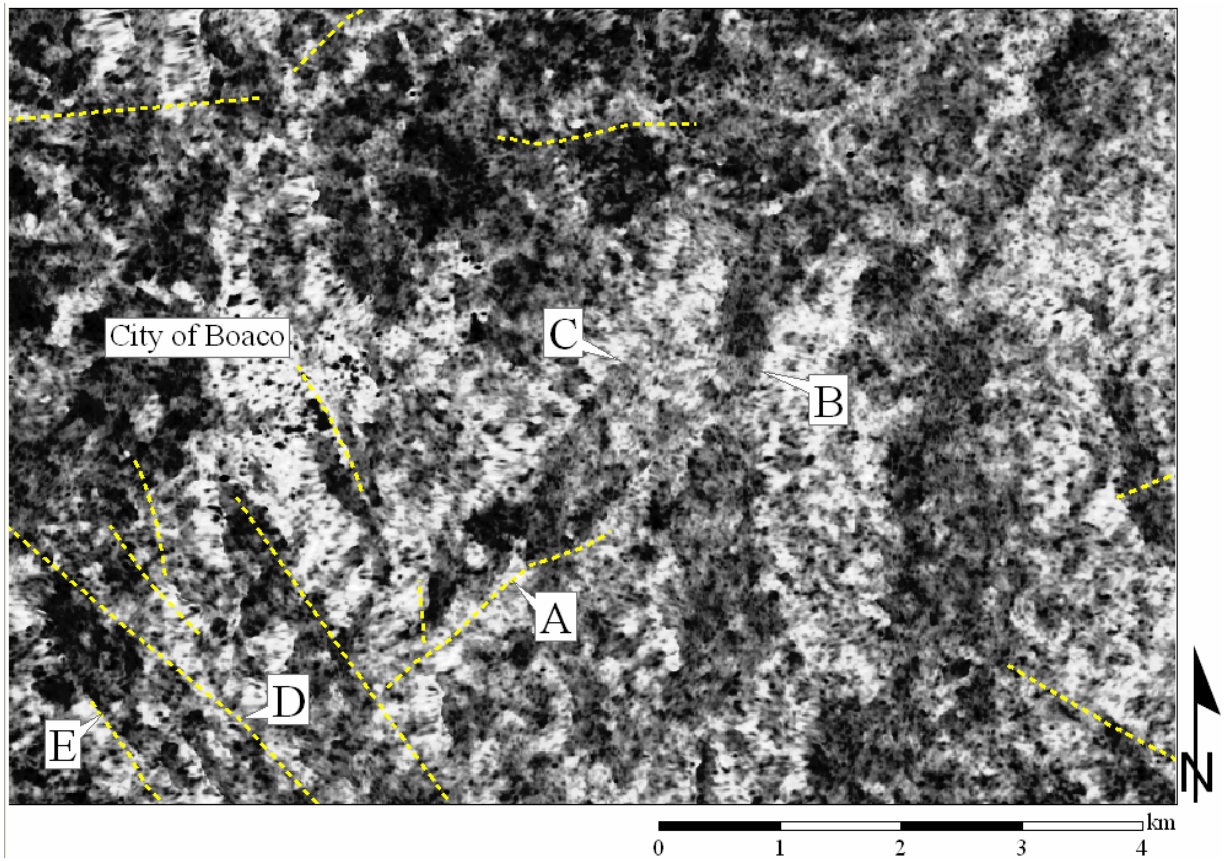

Figure A2-1: Example of "good" exhibition of faulting in both primary directions in RADARSAT-1 Change Detection Product. Image derived from RADARSAT-1 scenes courtesy of Alaska Satellite Facility Distributed Active Archive Center Program, NASA (2007, 2006, and 1997). Previously mapped faults are shown as dotted yellow lines. Fault A strikes NE/SW is clearly visible and likely continues beyond the mapped extent along feature B. Feature C strikes in the same direction as fault A and feature B, suggesting that this feature is also a fault. Faults striking NW/SE are also apparent, such as those labeled E and D.

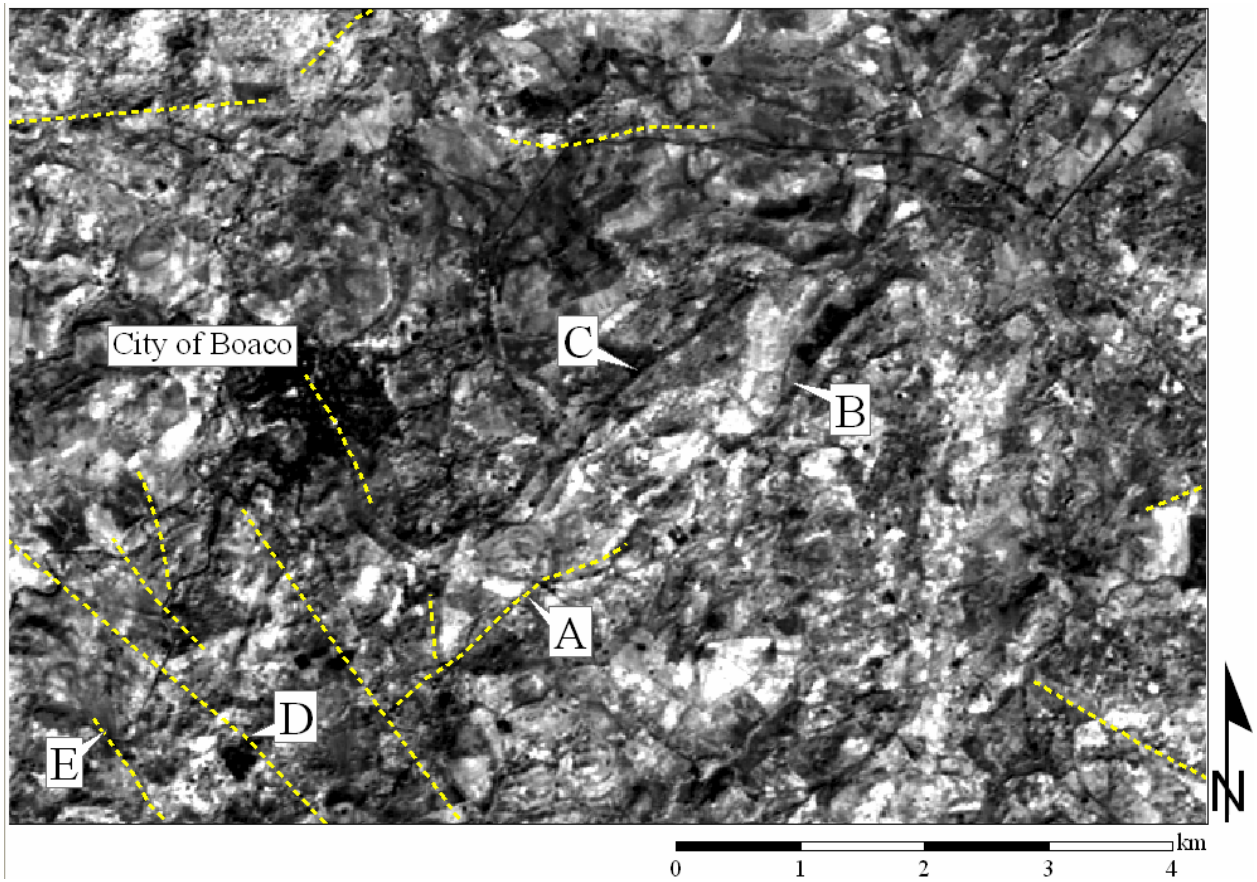

Figure A2-2: Example of "moderate" exhibition of NE/SW faulting and "poor" exhibition of NW/SE faulting in ASTER Band-3. Image derived from ASTER scene courtesy of USGS and Japan ASTER Program (2007). Previously mapped faults are shown as dotted yellow lines. Similar to Figure A2-1, fault A strikes NE/SW and is again likely to continue beyond the mapped extent along feature B. Feature C is also visible in this image and strikes in the same direction as fault A and feature B. Faults striking NW/SE are subtle, such as those labeled E and D.

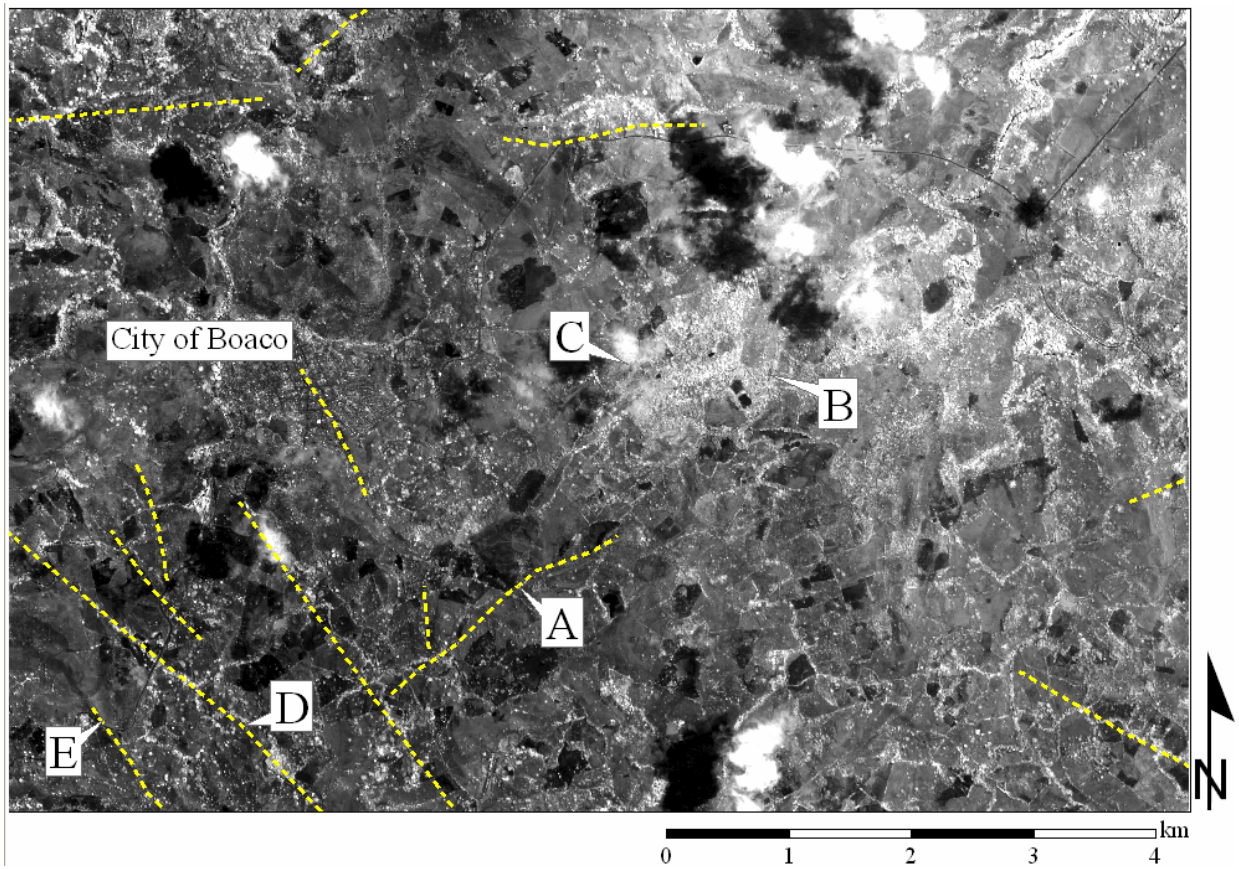

Figure A2-3: Example of "poor" exhibition of NE/SW faulting and "moderate" exhibition of NW/SE faulting in QuickBird Band-4. Imagery derived from QuickBird scene courtesy of Digital Globe (2006). Previously mapped faults are shown as dotted yellow lines. Fault A and features B and C are not evident in this image. Faulting in the NW/SE direction is fairly detectable. Fault D is apparent due to alignments in vegetation which are highly reflective (bright) in QuickBird Band-4. Fault E is observable due to topographic shadows caused by sun elevation and angle.

Appendix 3

Zipped Archive

Final image products and photographs of lineaments seen in the field.

Table A3-1: List of image file names of data products used for lineament mapping included in zipped archive. The following image files can be found in the supplimental file within the "RS Imagery" folder.

Sensor/Source	Product	File Name (.jpeg)
RADARSAT-1	Original	radar_original
	Despeckle 2	despeckle2
	Despeckle 3	despeckle3
	Despeckle 2 PCA	despeckle2_PCA
	Despeckle 3 PCA	despeckle3_PCA
	Change Detection	change_detection
ASTER	Original VNIR	vnir
	VNIR PCA	vnir_PCA
QuickBird	Oringinal (bands 1, 3, 4)	quickbird
Topographic Map	DEM	dem
RADARSAT-1	Composite 1	composite_1
RADARSAT-1 and ASTER	Composite 2	composite_2

Table A3-2: List of image file names of data products used for lineament mapping included in zipped archive. The following photos can be found in the supplemental file within the "Lineament Pictures" folder. All photos by author.

Lineament ID	Photo Name (.jpeg)	Easting (m)	Northing (m)
1	line1a	644267	1376299
	line1b		
2 a	line2a	644633	1376938
	line2Aa		
	line2Ab		
2 b	line2b	644139	1377333
	line2Ba		
	line2Bb		
3	line3	644252	1377005
4	line4a	observed from a distance	
	line4b		
5	line5a	647850	1381321
	line5b		
6	line6a	651948	1376346
	line6b		
	line6c		
7	line7a	651933	1376948
	line7b		
8	line8a	652117	1377346
	line8b		
9	line9a	observed from a distance	
	line9b		
10	line10a	653055	1378090
	line10b		
	line10c(distance)	observed from a distance	
11	line11a	652886	1378105
	line11b		
14	line14	observed from a distance	
15	line15	observed from a distance	
16	line16A	646133	1377343
	line16B		
	line16C		
17	line17	646459	1377057
18	line18A	646599	1376771
	line18B		
21	line21	644875	1380498
22	Line22A	644775	1380632
	Line22B		
23	line23A	643956	1381409
	line23B		

Table A3-2: List of image file names of data products used for lineament mapping included in zipped archive – continued.

Lineament ID	Photo Name (.jpeg)	Easting (m)	Northing (m)
24	line24a	644001	1381804
	line24b		
	line 24c		
25	line25A	644151	1381410
	line25B		
	line25C		
26	line26A	644319	1381093
	line26B		
27	line27A	644445	1381036
	line27B		
28	line28A	645305	1380508
	line28B		
29	line29A	645933	1380922
	line29B		
30	line30A	646074	1380979
	line20B		
31	line31A	646463	1380147
	line31B		
32	line32A	646019	1379471
	line32B		
	line32C		
	line32D		
	line32E		
	line32F		
	line32G		
34	line34A	646542	1379366
	line34B		
35	line35	646667	1379474
36	line36	646895	1379082
37	line37A	646595	1378955
	line37B		
38	line38a	646239	1378683
	line38b		
40	line40a	645233	1378288
	line40b		
41	line41a	644968	1377700
	line41b		
42	line42a	644699	1377091
	line42b		
44	line44a	643991	1376444
	line44b		
46	line46	643440	1376053

Appendix 4

Blank well survey form, completed well surveys and photographs of tested wells from field campaign. The blank well survey form has been slightly altered from the original form used during the field campaign.

WELL SURVEY

GPS Well ID #: _____

Date/Time: _____

Boaco ID: _____

Name of well manager and phone number: _____

Location

GPS coordinates (UTM): Sketch location:

_____E _____N

Picture number: _____

Description of site and terrain:

_____

_____

Details

Well type: ☐ Drilled ☐ Hand-dug

Well status: ☐ Open ☐ Sealed/cemented

Well owner: ☐ Public ☐ Private ☐ Industry: _____

Intended use: ☐ Household ☐ Irrigation ☐ Industrial ☐ Not in use

Type of pump: _____

Pumping periods: _____

Water appearance: ☐ Turbid ☐ Clear

Additional notes:

_____

_____

_____

Pump test feasibility: poor --- 1 --- 2 --- 3 --- good

Red gate: A

Well Survey

GPS Well ID #: Well 7 Boaco ID: E. San Nicolas

Date/Time: 3:30pm 3/12/08

Name of investigator: Jie

Location

Name of farm or town: E. of San Nicolas

GPS coordinates (UTM): Sketch location:

0641856 E 1381579 N

Picture number: 11

Description of site and terrain: very flat, (Qal ?), yellow house

---

Details

Well type: ☒ Drilled ☐ Hand-dug

Well status: ☐ Open ☒ Sealed/cemented

Well owner: ☒ Public ☐ Private ☐ Industry: _____

Intended use: ☒ Household ☐ Irrigation ☐ Industrial ☐ Not in use

Type of pump: Rope

Pumping periods: _____

Water appearance: ☐ Turbid ☒ Clear

Measurements:

Description of reference point and elevation above ground surface (m)	top of casing
Depth to water level ~~(m)~~ ft	22.41 ft
Diameter at surface ~~(m)~~ ft	0.35 ft
Temperature ~~(F)~~ °C	27.5 °C
Conductivity µS	815 µS

Pump test feasibility: poor --- 1 --- 2 --- 3 --- good

Additional notes: need to return to ask more questions ✓ to set up test

☆ 7:30 am 3/16/08 pump test

Figure A4-1: Photograph of E. San Nicolas well (survey well 7). Photo by author.

Well Survey

GPS Well ID #: Well 8 Boaco ID: Juan Jose Amador urbina

Date/Time: 3:50pm 3/12/08

Name of investigator: Jill

Location

Name of farm or town: N. San Nicolas

GPS coordinates (UTM): Sketch location:

0646753 E 1381740 N

Picture number: 12 pumping pics #63-65

Description of site and terrain: mostly flat (Qal?)

Details

Well type: ☒ Drilled ☐ Hand-dug

Well status: ☐ Open ☒ Sealed/cemented

Well owner: ☒ Public ☐ Private ☐ Industry: _____

Intended use: ☒ Household ☐ Irrigation ☐ Industrial ☐ Not in use

Type of pump: Rope

Pumping periods: 33 households use it

Water appearance: ☐ Turbid ☒ Clear

Measurements:

Description of reference point and elevation above ground surface (m)	top of casing
Depth to water level ~~(m)~~ ft	39.80
Diameter at surface ~~(m)~~ ft	0.5
Temperature ~~(F)~~ °C	29.2°C
Conductivity ms	862.0

ORP = 264.4

Pump test feasibility: poor --- 1 --- 2 --- 3 -- good

Additional notes: Saturday - when everyone is available to take water

talked to Juan across street - black house
- call him before pumping

3pm Saturday

Figure A4-2: Photograph of N. San Nicolas well (survey well 8). Photo by author.

Well Survey

GPS Well ID #: N/A well (11) Boaco ID: Axcelon

Date/Time: 11:00am 3/13/08

Name of investigator: Jill

Location

Name of farm or town: Santa Blanca

GPS coordinates (UTM): N/A Sketch location:

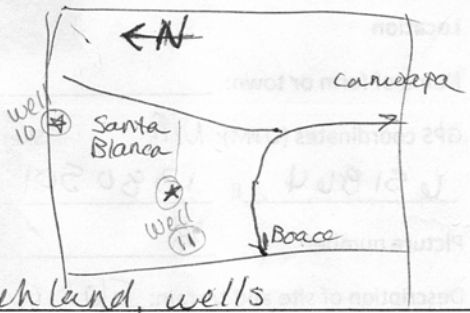

0652145 E 1381375 N

Picture number: 19 y 20

Description of site and terrain: very flat, ranch land, wells drilled for rice trg. - never used.

Details

Well type: ☒ Drilled ☐ Hand-dug

Well status: ☐ Open ☒ Sealed/cemented

Well owner: ☐ Public ☒ Private ☐ Industry: _____

Intended use: ☐ Household ☒ Irrigation ☐ Industrial ☐ Not in use

Type of pump: none

Pumping periods: _____

Water appearance: ☐ Turbid ☐ Clear ?

Measurements: X → pumping showed clear water

Description of reference point and elevation above ground surface (m)	top of casing
Depth to water level ~~(m)~~ (ft)	21.82
Diameter at surface (m)	0.55
Temperature ~~(F)~~ °C	N/A
Conductivity mS	672.0

ORP: 244.1

Pump test feasibility: poor --- 1 --- 2 --- (3) --- good

Additional notes: top is sealed metal - need to puncture away from road

Figure A4-3: Photograph of Santa Blanca well (survey well 11). Photo by author.

Well Survey

GPS Well ID #: Well 12 Boaco ID: S. Boaco (on main highway to Boaco)

Date/Time: 11:10 am 3/15/08

Name of investigator: Jill

Location

Name of farm or town: Green Ranch House

GPS coordinates (UTM): 0643542 E 1376043 N Sketch location:

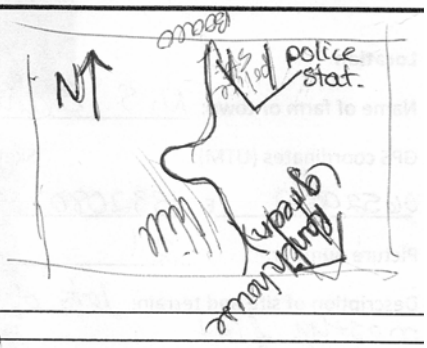

Picture number: 58

Description of site and terrain: hill to E, somewhat flat to west, sm. dry stream to S.

Details

Well type: ☒ Drilled ☐ Hand-dug

Well status: ☐ Open ☒ Sealed/cemented

Well owner: ☐ Public ☒ Private ☐ Industry: _____

Intended use: ☒ Household ☐ Irrigation ☐ Industrial ☐ Not in use

Type of pump: Rope

Pumping periods: _____

Water appearance: ☐ Turbid ☒ Clear

Measurements:

Description of reference point and elevation above ground surface (m)	top of casing
Depth to water level ~~(m)~~ (ft)	17.73
Diameter at surface (m) (ft)	0.33
Temperature ~~(F)~~ (°C)	29
Conductivity (µS)	805

Pump test feasibility: poor --- 1 --- 2 --- 3 --- good

Additional notes: ~~depth = 60 x 33'~~ well is 1 mo. old (owner lives in Boaco dir. in purple notebook)

60m depth
not in basalt (white sand) [What is this? Ash? Pyroclastics?]
water table 16m
rope pump goes to 48'
driller: milder Gutierrez 20 gal/min.

10ft away, a well was hand-dug - did not produce very much, collapsed, test: 5 gal/min, lower water depth

Figure A4-4: Photograph of S. Boaco well (survey well 12). Photo by author.

Leornel Antonio Sosa Lira

Well Survey

GPS Well ID #: Well 13 Boaco ID: S. Boaco Police Sta.

Date/Time: 11:30 am 3/15/08

Name of investigator: Jill

Location

Name of farm or town: Munic. St. House well

GPS coordinates (UTM): ~~X~~ Sketch location:

0644846 E 1376678 N

Picture number: 59 & 60

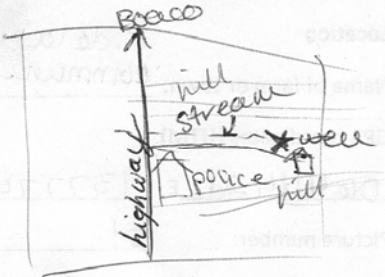

Description of site and terrain: in a dry stream valley stream runs roughly E/W ~~to~~ can see fracturing in bedrock in stream bottom

Details

Well type: ☒ Drilled ☐ Hand-dug

Well status: ☐ Open ☒ Sealed/cemented

Well owner: ☐ Public ~~☒ Private~~ ☒ Industry: municipal slaughter horse

Intended use: ☐ Household ☐ Irrigation ☒ Industrial ☐ Not in use

Type of pump: electric

Pumping periods: ~5hrs everyday to everyotherday

Water appearance: ☐ Turbid ☒ Clear

Measurements:

Description of reference point and elevation above ground surface (m)	top of casing
Depth to water level ~~(m)~~ (ft)	4.61
Diameter at surface (m) (ft)	0.5
Temperature (F)	N/A
Conductivity	N/A

Pump test feasibility: poor --- 1 --- 2 --- 3 --- ~~good~~

Additional notes: 50m deep, 8" diameter pump fills tank, pumps ~5hrs. every day, every other day.

↳ how to measure this flow rate?

~~* GPS pt.~~

Figure A4-5: Photograph of Municipal Slaughter House well (survey well 13). Photo by author.

Well Survey

GPS Well ID #: Well 14 Boaco ID: South Paso de Laja (S)

Date/Time: 12:10 pm 3/15/08

Name of investigator: Jill

Location

Name of farm or town: P. de Laja community well

GPS coordinates (UTM): Sketch location:

0644421 E 1377446 N

Picture number: 61

Description of site and terrain: ~~Flat~~ small valley w/ dry stream coming down to ~~Rio Tuan~~. stream

Details

Well type: ☒ Drilled ☐ Hand-dug

Well status: ☐ Open ☒ Sealed/cemented

Well owner: ☒ Public ☐ Private ☐ Industry: _____

Intended use: ☒ Household ☐ Irrigation ☐ Industrial ☐ Not in use

Type of pump: rope, single handed, smaller

Pumping periods: _____

Water appearance: ☐ Turbid ☒ Clear

Measurements:

Description of reference point and elevation above ground surface (m)	TOP of CASING
Depth to water level ~~(m)~~ (ft)	27.00? Estimate!
Diameter at surface (m) (ft)	0.5
Temperature ~~(F)~~ (°C)	28.7
Conductivity (mS)	768

Pump test feasibility: poor --- 1 --- 2 --- 3 --- **good**

Additional notes: well diameter looks somewhat large pump @ least 1 gal/min.

Figure A4-6: Photograph of S. Paso de Laja well (survey well 14). Photo by author.

Comm. Leader: Fermin Mendosa

Well Survey

GPS Well ID #: Well 15 Boaco ID: Paso de Laja (N)

Date/Time: 12:30pm 3/15/08

Name of investigator: Jue

Location

Name of farm or town: Paso de Laja

GPS coordinates (UTM): Sketch location:

0644813 E 1378256 N

Picture number: 62

Description of site and terrain: Near (~200m) from Rio Fransesca, somewhat flat, minor hills around, Rio F. makes a small Ravine

Details

Well type: ☒ Drilled ☐ Hand-dug

Well status: ☐ Open ☒ Sealed/cemented

Well owner: ☒ Public ☐ Private ☐ Industry: _____

Intended use: ☒ Household ☐ Irrigation ☐ Industrial ☐ Not in use

Type of pump: Rope

Pumping periods: Serves 21 houses

Water appearance: ☐ Turbid ☐ Clear

Measurements:

Description of reference point and elevation above ground surface (m)	TOP of casing
Depth to water level ~~(m)~~ ft	33.00 ? ESTIMATE
Diameter at surface (m)	0.33
Temperature ~~(F)~~ °C	30
Conductivity µS	681

Pump test feasibility: poor --- 1 --- 2 --- 3 --- good

Additional notes: detected by divining - Novem. 2007 UNICEF

SUNDAY anytime

Figure A4-7: Photograph of Paso de Laja well (survey well 15). Photo by author.

Well Survey

GPS Well ID #: Well 16 Boaco ID: South S. Nic.

Date/Time: 4:40pm 3/15/08

Name of investigator: Jill

Location

Name of farm or town: community well S. Nic.

GPS coordinates (UTM): Sketch location: See well 17

0646666 E 1381020 N

Picture number: 166

Description of site and terrain: flat → wal? S. of San Nicolas Comm., near another well - this one is used more

Details

Well type: ☒ Drilled ☐ Hand-dug

Well status: ☐ Open ☒ Sealed/cemented

Well owner: ☒ Public ☐ Private ☐ Industry: _____

Intended use: ☒ Household ☐ Irrigation ☐ Industrial ☐ Not in use

Type of pump: Rope

Pumping periods: mostly morn. & evening

Water appearance: ☐ Turbid ☒ Clear

Measurements:

Description of reference point ~~and elevation above ground surface (m)~~	top of well bore casing
Depth to water level ~~(m)~~	21.4 ft
Diameter at surface ~~(m)~~	0.35 ft
Temperature ~~(°C)~~	29.7°C
Conductivity	ℓe 50

ORP: ~~252.7~~ 250.2

Pump test feasibility: poor --- 1 -- (2) -- 3 -- (good) ?

Additional notes: ~~bad bolts~~

Figure A4-8: Photograph of S. San Nicolas (A) well (survey well 16). Photo by author.

Well Survey

GPS Well ID #: Well 17 Boaco ID: South S. Nic

Date/Time: 4:45pm 3/15/08

Name of investigator: Jill

Location

Name of farm or town: community well S. Nic

GPS coordinates (UTM): Sketch location:

0641671 4 E 1381048 N

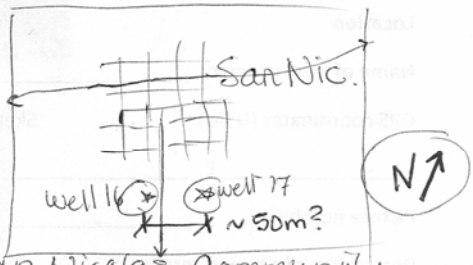

Picture number: 65-68

Description of site and terrain: flat, ~~rural~~? S. of San Nicolas Community

Details

Well type: ☑ Drilled ☐ Hand-dug

Well status: ☐ Open ☒ Sealed/cemented

Well owner: ☒ Public ☐ Private ☐ Industry: _____

Intended use: ☑ Household ☐ Irrigation ☐ Industrial ☐ Not in use

Type of pump: Rope

Pumping periods: mostly morning & evening, less used than well 16 because pump is more difficult to crank and rope often slips.

Water appearance: ☐ Turbid ☒ Clear

Measurements:

Description of reference point ~~and elevation above ground surface (m)~~	top of wellbore casing
Depth to water level ~~(m)~~	22.41 ft
Diameter at surface ~~(m)~~	0.33 ft
Temperature ~~(°C)~~	28.3 °C
Conductivity	775.1

ORP: ~~775.1~~ 257.5

Pump test feasibility: poor --- 1 ~~2~~ --- 3 --- good ?

Additional notes: ~~bad bolts~~ can only pump @ 2 gal/min?

It would be interesting to compare pump test results to well 16 — same aquifer?

Figure A4-9: Photograph of S. San Nicolas (B) well (survey well 17). Photo by author.

Appendix 5

Temperature and specific conductivity measurements of tested wells.

Table A5-1: Temperature and specific conductivity values for pump tested wells, measured with flow-through cell.

Community Name	Temperature (°C)	Conductivity (µS/cm)	Easting Coordinate (m)*	Northing Coordinate (m)*	Ground Elevation of Well (m)
E San Nicolas	27.5	815	646,856	1,381,579	404
N San Nicolas	29.2	862	646,753	1,381,740	407
Santa Blanca	N/A	672	652,145	1,381,375	369
S Boaco	29	805	643,542	1,376,043	310
Municiple Slaughter House, S Boaco	N/A	N/A	644,846	1,376,678	345
S Paso de Laja	28.7	768	644,421	1,377,746	311
Paso de Laja	30	681	644,813	1,378,256	300
S San Nicolas (A)	29.7	650	646,666	1,381,020	400
S San Nicolas (B)	28.3	775	646,714	1,381,048	400

*Datum: WGS 84, UTM Zone 16N

Appendix 6

Geographical information system (GIS) method for filtering lineament interpretations and ranking image performance.

Geographical Information System (GIS) Method for Filtering Lineament Interpretations and Ranking Image Performance.

1. Compute acceptable lineament interpretation buffer width – this represents the *fracture zone.* Measurements of the acceptable buffer width are most likely larger than the fracture zones they represent due to extensive weathering in the study area.

   In ArcGIS, digitized faults from the geological map were displayed on top of the QuickBird image. Attributes exhibited by the QuickBird image nearby faults, such as vegetation concentrations and tonal variations in the soil, were observed. Distances across (perpendicular to) the faults where the QuickBird image exhibited fault-like characteristics were measured. Twenty-four measurements, distributed over the study area, were taken, averaging 172m width.

   The QuickBird image was chosen over the other image types for judging the acceptable buffer width because it has the highest spatial resolution and results in the most accurate measurements.

2. Check all lineament interpretations:

   Each lineament interpretation (16 total) was examined to ensure that all lineaments drawn were actually observable (i.e., does each lineament exist in the image?) and to ensure all possible lineaments were found. This step is important to guarantee the interpretations are of high quality.

3. GIS analysis to filter lineament interpretations:

   A. Buffer each lineament interpretation polyline shapefile by the fracture zone width (86m buffer = 172m fracture zone), Figure A6-1.

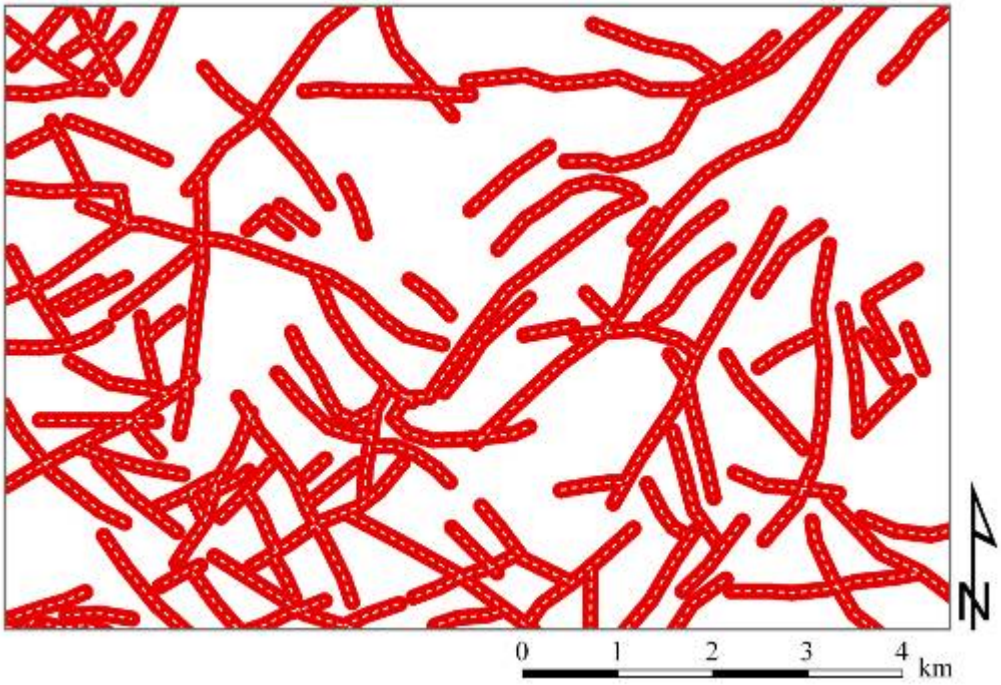

Figure A6-1: Original lineament interpretation and buffer, step 3A. The original lineament interpretation is displayed as white dashed lines and was observed from ASTER VNIR product. 172m wide buffers are displayed in red and are calculated for each lineament.

B. Calculate buffer areas for each interpretation shapefile. These values will be used later to assess image performance (step 4).

C. Change each buffer shapefile created in (step 3A) into a raster file. Select an appropriate pixel size (i.e., 1 meter).

D. Reclassify each raster created in (step 3A) so that buffer pixels = 1 and no data pixels = 0 to create a binary raster, Figure A6-2.

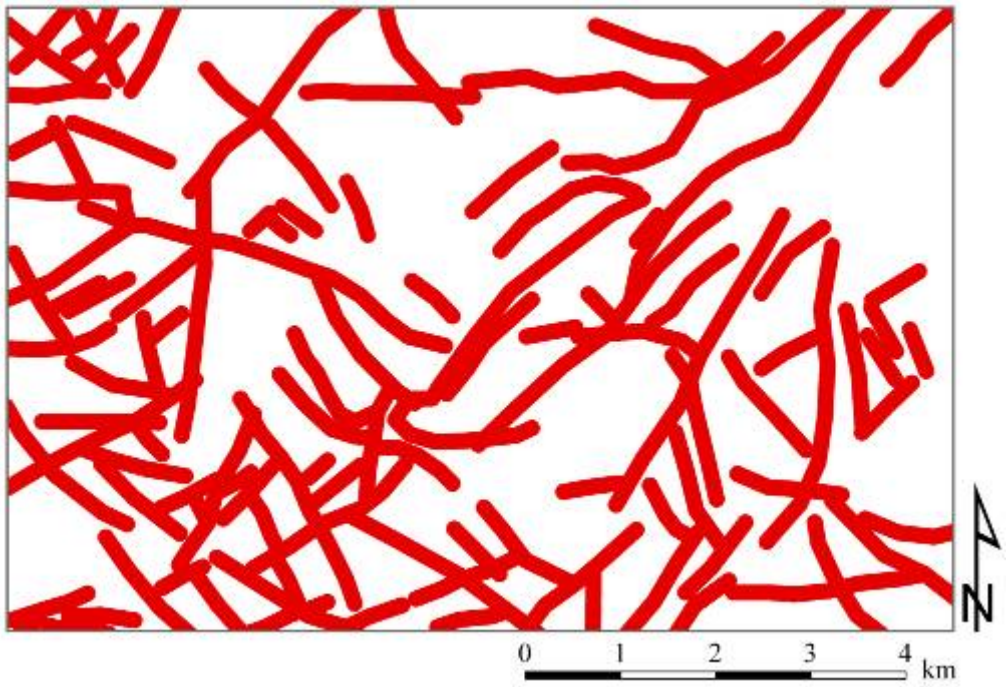

Figure A6-2: Reclassified buffer raster, step 3D. This raster is created from the buffer shapefile and reclassified into a binary raster so that buffer areas have a value of 1, shown in red, and areas without a raster have a value of 0, shown as white. Notice that the reclassified raster has the same coverage as the buffer shown in Figure A6-1.

E. Add all the reclassified rasters from (step 3C). The output, called the coincidence raster, shows the level of agreement between all lineament interpretations. For example, if 16 interpretations were used in the analysis, then the maximum level of agreement in the coincidence raster would have a value of 16. Areas of no agreement would have a value of 0. It is most helpful to view the coincidence raster with a gradational color theme and displaying the values of 0 and 1 in black (no agreement areas), Figure A6-3.

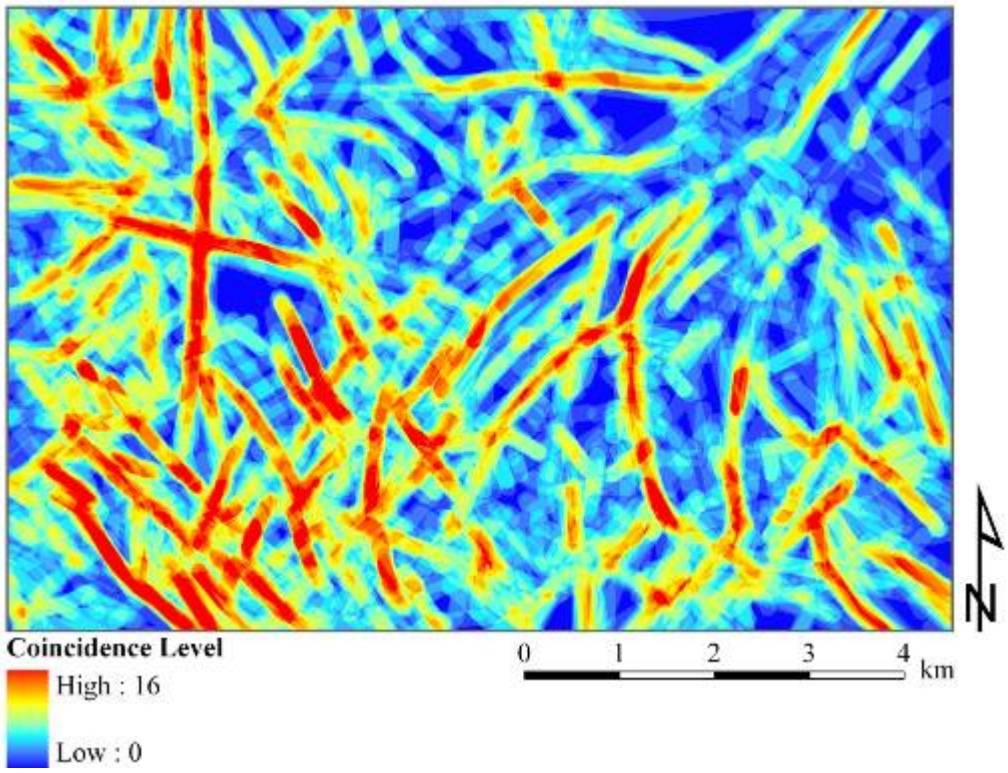

Figure A6-3: Coincidence raster created using all interpretations, step E. Sixteen lineament interpretations were used to create this coincidence raster. Warmer colors indicate greater agreement between lineament interpretations. Not much of the study area is free of lineament interpretations (coincidence level = 0).

The coincidence raster created in this study from the 16 lineament interpretations was overwhelmed by the level of detail present in QuickBird image interpretations. A second coincidence raster was created by adding all the reclassified rasters from (step 3C) except the QuickBird interpretations, reducing the number of input rasters from 16 to 11. This results in a coincidence raster that is much more visually acceptable, Figure A6-4.

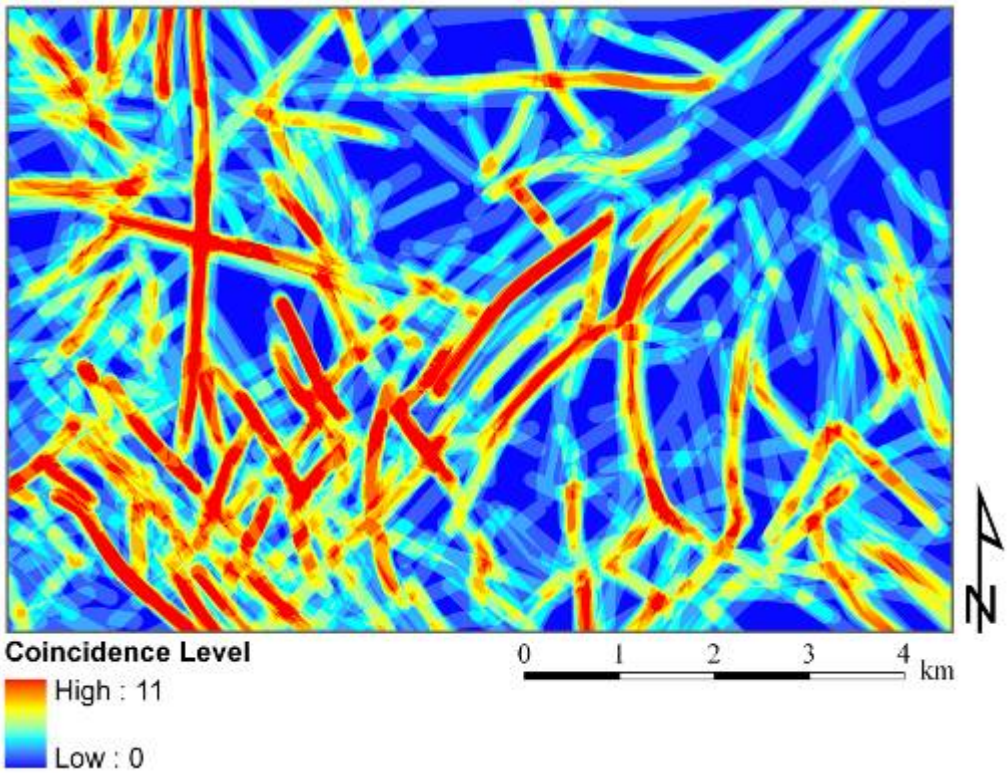

Figure A6-4: Coincidence raster created using all but QuickBird derived lineament interpretations, step E. Eleven lineament interpretations, including those from ASTER, RADARSAT-1, and composite products, were used to create this coincidence raster. Warmer colors indicate greater agreement between lineament interpretations. Notice that more of the study area is free of lineament interpretations (coincidence level = 0) than is shown in Figure A6-3.

F. Reclassify the coincidence raster (step 3D) so that areas of no agreement (coincidence raster values 0 and 1) = 0 and areas of coincident lineaments (coincidence raster values >2) = 1, Figure A6-5.

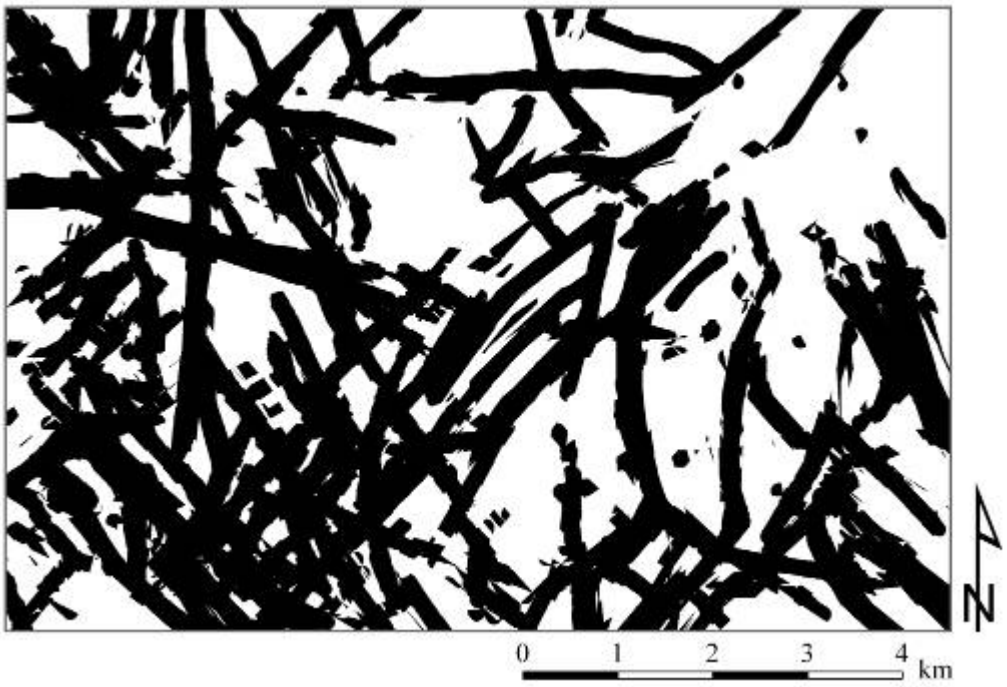

Figure A6-5: Reclassified coincidence raster with coincidence number = 2, step 3F. Areas in black show where coincidence number is greater than or equal to 2, meaning that in these locations, lineaments have been observed two or more times. Areas in white are either where no lineaments were observed or only observed once.

Depending on the image types used, these parameters for reclassifying may be biased. In this study several of the lineament interpretations were made from similar image products. For example, three individual interpretations produced from RADARSAT-1 products are very similar, including interpretations from the stack of all original RADARSAT-1 scenes and the despeckled (levels 2 and 3) products. Agreement in the coincidence raster is almost definite. To remove bias inherent to this coincidence raster, coincidence raster values of 0, 1, 2, and 3 are set = 0, and areas in agreement >4 times are set = 1, Figure A6-6.

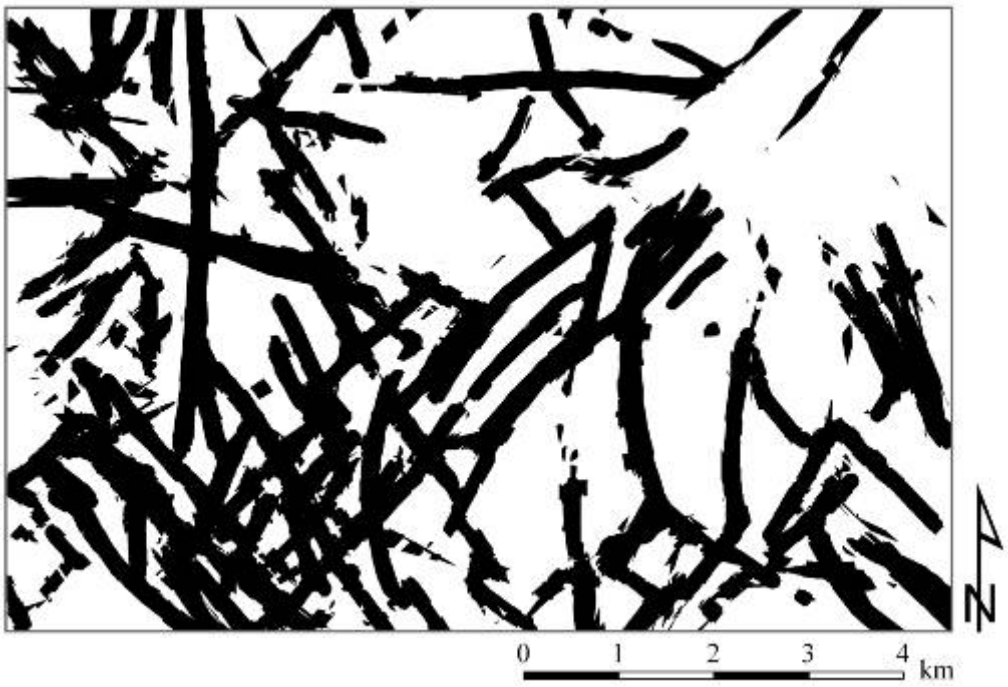

Figure A6-6: Reclassified coincidence raster with coincidence number = 4, step 3F. Areas in black show where coincidence number is greater than or equal to 4, meaning that in these locations, lineaments have been observed four or more times. Areas in white are either where no lineaments were observed or less than four times. Notice how much less area is consider *coincident* than in Figure A6-5.

G. Transform the reclassified coincidence raster (step 3E) into a coincident lineament shapefile. The result will be polygons for only areas of coincident lineaments.

   The shapefile created in this step will have many "sliver" polygons of significantly small area. These can be removed by selecting and deleting areas below a specified threshold. In this study, polygons <60,000m^2 were removed to clean up the coincident lineament shapefile, Figure A6-7.

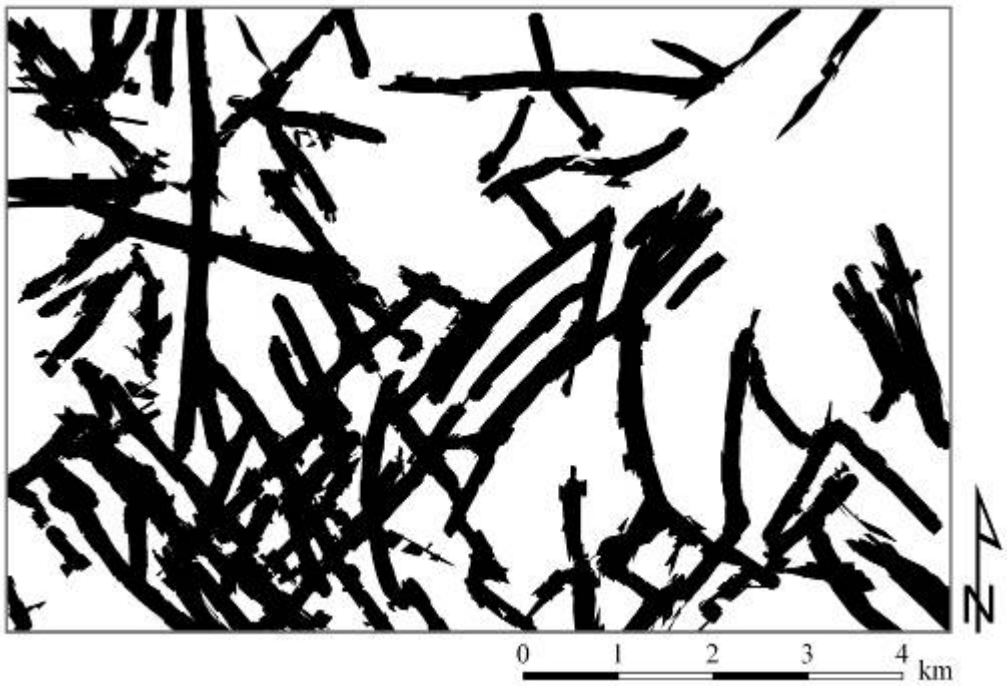

Figure A6-7: Coincidence lineament polygon shapefile with sliver polygons removed. This polygon shapefile was created from the coincidence raster shown in Figure A6-6. Areas less than 60,000 m2, called sliver polygons were removed so that the resulting polygons are all linear in shape, unlike in Figure A6-6.

H. Clip all original lineament interpretation buffer polygon shapefiles (step 3A) by the coincident lineament shapefile (step 3G) and calculate areas of the resulting clipped lineament buffers, Figure A6-7. These values will be used later to assess image performance (step 4).

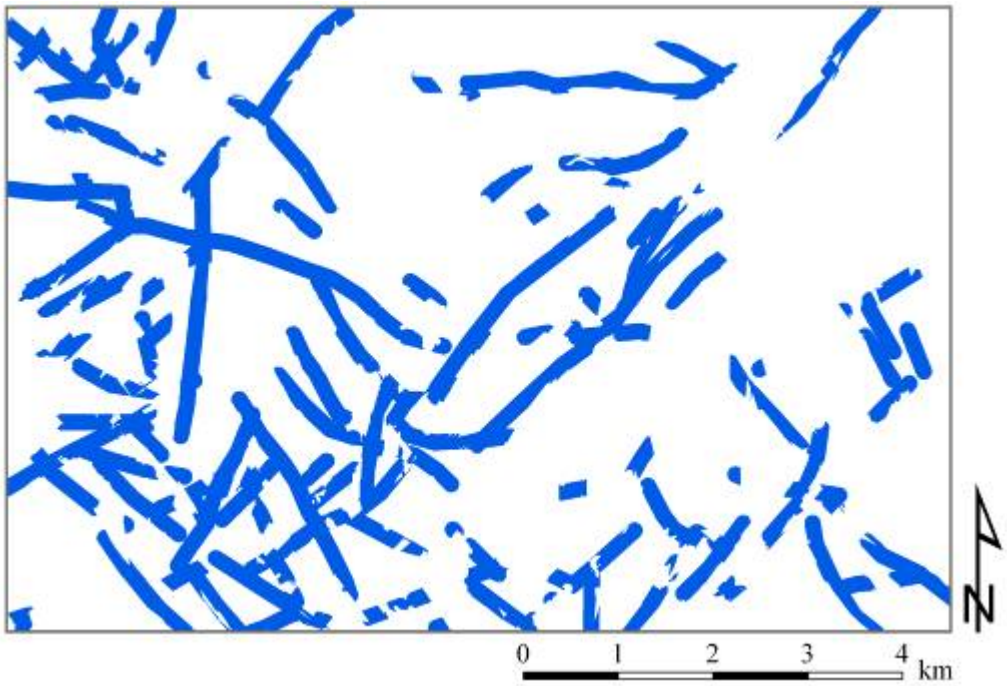

Figure A6-8: Filtered lineament buffer. The blue areas shown are buffer areas that survived the filtering process. These areas represent where the original buffer areas overlap with the coincidence lineament shapefile shown in Figure A6-7.

4. Assess image performance for lineament interpretations – two methods:

   A. (1) Determine how much of the original lineament interpretation is explained in the coincidence raster filter – an overlap comparison of the original interpretation and filter. This is calculated as a percent by dividing the area of the filter lineament buffer by the coincidence buffer.

   B. (2) Examine the degree to which an original interpretation survived the filtering process – a before and after comparison of the lineament interpretation alone. This is calculated as a percent by dividing the area of the filter lineament buffer by the original lineament buffer.